

Design Rules for Solid State Fluorescence
Exploiting Excited State Intramolecular
Proton Transfer

Michael Dommett

School of Biological and Chemical Sciences
Queen Mary University of London

Submitted in partial fulfillment of the requirements
of the Degree of Doctor of Philosophy

January 2019

Abstract

Aggregation-induced emission (AIE) offers a route for the development of solid state organic luminescent technologies, overcoming the common and undesirable phenomenon of aggregation caused quenching. Excited-state intramolecular proton transfer (ESIPT) is an attractive feature to incorporate into the an AIE-active material, which results in red-shifted fluorescence and reduced self-absorption. ESIPT coupled to AIE can produce materials with emission across the visible spectrum, with applications in imaging, detection, optoelectronics, and solid state organic lasers. However, maximising fluorescence is a formidable challenge in attaining first-principles materials design, due to the interplay between the electronic structure of the chromophore and the crystalline environment.

In this work, computational methods are used to investigate how the molecular properties and the environment mediate fluorescence for ESIPT systems. We concentrate on a family of systems, 2'-hydroxychalcones (**H**Cs), with substituent- and morphology-dependent fluorescence. The aim of this thesis is to uncover the mechanism behind why some of these compounds undergo AIE, whilst some remain dark in both solution and the solid state.

By initially isolating molecular properties, we find the systems are non-fluorescent in vacuum due to nonradiative decay *via* conical intersections. Using cluster models, we then probe the potential energy surfaces in the solid state, assessing how intra- and intermolecular processes dictate fluorescence. Based on our calculations, we establish guiding principles which mediate fluorescence in these materials.

The scope is then extended to a related set of molecules, 2-hydroxyphenylpropenones, whose AIE behaviour is even more pronounced. We account for their remarkable photochemical properties through the design rules established for the 2'-hydroxychalcones. We systematically investigate competing excited state decay channels in a total of eleven systems to evaluate the factors needed for efficient ESIPT fluorophores, accounting for the crystal morphology, exciton coupling, and exciton hopping rates. This study of structure-property relationships for luminophores based on the ESIPT mechanism bridges the understanding of molecular photochemistry with crystal structure, aiding the development of highly efficient solid state emitters.

Statement of Originality

I, Michael Dommett, confirm that the research included within this thesis is my own work or that where it has been carried out in collaboration with, or supported by others, that this is duly acknowledged below and my contribution indicated. Previously published material is also acknowledged below.

I attest that I have exercised reasonable care to ensure that the work is original, and does not to the best of my knowledge break any UK law, infringe any third party's copyright or other Intellectual Property Right, or contain any confidential material.

I accept that the College has the right to use plagiarism detection software to check the electronic version of the thesis.

I confirm that this thesis has not been previously submitted for the award of a degree by this or any other university.

The copyright of this thesis rests with the author and no quotation from it or information derived from it may be published without the prior written consent of the author.

Signature: Michael Dommett

Date: 10/01/2019

Details of collaboration and publications:

1. **M.Dommett** and R. Crespo-Otero, *Phys. Chem. Chem. Phys.*, 2017, **19**, 2409-2416
2. **M. Dommett**, M. Rivera and R. Crespo-Otero, *J. Phys. Chem. Lett.*, 2017, 6148-6153
3. L. del Olmo[†], **M. Dommett**[†], I. H. Oevreeide, A. Walsh, D. Di Tommaso and R. Crespo-

[†]Equal Contribution

Otero, *J. Mater. Chem. A*, 2018, **6**, 24965-24970

4. M. Rivera, **M. Dommett** and R. Crespo-Otero, *J. Chem. Theo. Comput.*, 2019, **15**, 2504-2516
5. **M.Dommett**, M. Rivera, M. T. Hollis-Smith, R. Crespo-Otero, Connecting Crystal Structure and Chromophore Design, *In Preparation*
6. M. Cirulli, E. Salvadori, Z.-H. Zhang, **M. Dommett**, F. Tuna, H. Bamberger, R. Crespo-Otero, J. van Slageren. S. Goldup and M. Roessler, Tuning the Magnetic Anisotropy of Cobalt(II) Complexes through Peripheral Ligand Modifications: Rotaxane-based Single-Ion Magnets, *In Preparation*

Acknowledgements

I first want to thank my supervisor Dr. Rachel Crespo-Otero. From when I first interviewed for the position on Skype from a hostel in Colombia, I knew that I wanted to work with her, and I haven't once regretted my decision. She has been the best supervisor I could have asked for, and working with her has been a pleasure. I have learned much from her outstanding scientific abilities and it has been a privilege to be her first PhD student. I appreciate the space that she has given me to explore my own ideas and interests, whilst always being available to discuss any topic at all. The last three years have flown by and I am sad that it is all over.

I would like to thank Miguel Rivera, who since joining the group has become a great colleague and friend. The last three years with my computational chemistry colleagues, Etienne, Shaima, Fu, Bob, Matteo, Ljiljana, have been a great experience. I thank my PhD Panel members Prof. Tony Vlcek and Dr. Greg Chass for their interest, discussions and ideas for the project. Thank you to Dr. Devis Di Tommaso for all the help, in particular in molecular dynamics. I would like to thank Prof. Mario Barbatti for his hospitality and scientific expertise when I visited his group in Marseille in June 2018.

The support from my family has been constant during the last three years. My parents have always encouraged me, offering blind optimism that I could solve whatever problem I had, whilst constantly stating they had "absolutely no idea" what I was doing (something to do with excited atoms). In particular I want to thank my sister, who put up with me as a flatmate during my first two years in London. Her support (mostly financial) will never be forgotten, and will (someday) be repaid. Greg, I like your sheets.

Finally, I couldn't have done this without my girlfriend Colombine and it is to you I owe the most. Your love, support, and enthusiasm have made this process so easy, even with us living in different countries. Thank you for always being there, always believing in me, and making things so simple.

Contents

Statement of Originality	2
Acknowledgements	4
List of Figures	9
List of Tables	12
List of Abbreviations	13
1 Introduction	17
1.1 Background	17
1.2 Thesis Framework	18
2 Theoretical Framework	21
2.1 Quantum Mechanics and Chemistry	21
2.1.1 Overview	21
2.1.2 The Schrödinger Equation	22
2.1.3 The Born-Oppenheimer Approximation	23
2.2 Molecular Photochemistry	25
2.2.1 Fundamental Principles	25
2.2.2 Conical Intersections	27
2.2.3 Dynamics Simulations of Excited State Processes	28
2.3 Photophysics of Molecular Aggregates	32
2.3.1 Molecular Stacking	32
2.3.2 Exciton Theory	34
2.3.3 Exciton Transport Regimes	36
2.3.4 Approaches to Calculate Exciton Couplings	37
2.3.5 Modelling Excited States in Molecular Crystals	39

3	Luminescent Organic Materials	43
3.1	Aggregation Induced Emission	43
3.1.1	Overview	43
3.1.2	Hypothesised Mechanisms	44
3.1.3	Optoelectronic Applications of AIE	46
3.2	Mechanistic Interpretations of AIE	46
3.2.1	Approaches Based on Fermi Golden Rule	46
3.2.2	Huang-Rhys Factors and Reorganisation Energies	49
3.2.3	Restricted Access to Conical Intersection Model	51
3.3	Excited State Intramolecular Proton Transfer	54
3.3.1	Combining AIE with ESIPT	54
3.3.2	The Four-Level Photocycle	54
3.3.3	Exploiting ESIPT and AIE for Applications	56
3.3.4	Harnessing ESIPT for Near-IR Emission	57
3.4	Emitters Based on 2'-hydroxychalcones	59
3.4.1	Crystalline Emission Properties of HCs	59
3.4.2	Further Investigation into HC Photochemistry	60
4	Computational Chemistry Methods	64
4.1	The Hartree-Fock Method	64
4.2	Recovering Electron Correlation	67
4.2.1	Configuration Interaction	67
4.2.2	Møller-Plesset Perturbation Theory	69
4.2.3	Coupled Cluster	70
4.2.4	Multireference Methods	70
4.3	Density Functional Theory	72
4.3.1	Basis Sets	74
4.4	Methods for Excited States	75
4.4.1	Time Dependent Density Functional Theory	75
4.4.2	ADC(2) and CC2	77
4.4.3	Methods to Locate Minimum Energy Conical Intersections	79

5	Nonradiative Decay Mechanisms in 2'-hydroxychalcones	81
5.1	Introduction	81
5.2	Computational Methods	82
5.3	Results	83
5.3.1	Vertical Excitations	83
5.3.2	Excited State Minima	85
5.3.3	Relaxation Channels	87
5.3.4	Nonadiabatic Dynamics	89
5.4	Conclusions	97
6	Inter- and Intramolecular Interactions in the Solid State	100
6.1	Introduction	100
6.2	Computational Methodology	102
6.3	Results	106
6.3.1	Benchmarking of TDDFT	106
6.3.2	Absorption in the Molecular Crystal	107
6.3.3	Radiative vs. Nonradiative Decay	110
6.4	Summary and Conclusions	116
7	Connecting Chromophore Design with Crystal Morphology	119
7.1	Introduction	119
7.2	Computational Details	121
7.3	Results	123
7.3.1	Potential Energy Surfaces of HP Derivatives in Vacuum	123
7.3.2	HP Bias for ESIPT	125
7.3.3	Relaxation Pathways in the Molecular Crystal	127
7.3.4	Radiative Decay Rates	130
7.3.5	Huang-Rhys Factors	131
7.3.6	Analysis of Crystal Packing	134
7.3.7	Intermolecular Interactions in the Molecular Crystal	138
7.3.8	Exciton Hopping	143
7.4	Conclusions	145

8	Conclusions and Outlook	147
8.1	Mechanistic Overview and Design Rules	147
8.2	Detailed Summary of Results	148
9	Bibliography	152
	Appendices	167

List of Figures

2.1	Relaxation pathways post electronic excitation.	26
2.2	Schematic of the double-cone topology of degenerate electronic states	29
2.3	Fluorescence spectrum of pyrene	32
2.4	Stacking arrangements of benzene	33
2.5	Exciton energy level diagram for H- and J-aggregates	35
3.1	Examples of AIE-active chromophores	44
3.2	Schematic of the reorganisation energy in the adiabatic regime	51
3.3	Schematic of the RACI Model	52
3.4	The four-level photocycle of ESIPT	55
3.5	Emission behaviour of crystalline 2'-hydroxychalcone derivatives	59
3.6	Crystal structures of 2'-hydroxychalcone derivatives	60
4.1	Schematic of the mean-field approximation	67
5.1	Electron density difference maps	85
5.2	Simulated absorption spectra of HC1-5	86
5.3	HC energy levels	87
5.4	Potential energy surface along the relaxation mode θ_{tor}	88
5.5	Model of the state decay rates for HC1	91
5.6	Model of the state decay rates for HC5	92
5.7	Global fit for enol and keto states for HC1 in TSH simulations	94
5.8	Global fit for enol and keto states for HC5 in TSH simulations	95
5.9	Typical trajectories for HC1	96
5.10	Energies of important optimised states for 1	98
6.1	Molecular, dimer, and crystal structures of 1 and 5	102
6.2	The M7 and M15 cluster models	104

6.3	The Ewald cluster model	104
6.4	The D7 cluster models	105
6.5	The vacuum PES of 1-5 with TDDFT	108
6.6	Comparison of MECIs obtained with TDDFT and CASSCF	108
6.7	Relaxed geometry scan in the crystal	112
6.8	Decay mechanism in the molecular crystal in D7 model	113
6.9	Linear interpolation of internal coordinates in the solid state	114
6.10	Comparison of vacuum and solid state conical intersections	114
6.11	Radiative decay in HC1	117
6.12	Nonradiative decay in HC5	118
7.1	Molecular structures of eleven HC and HP compounds	120
7.2	The vacuum PES of HP1-4 with TDDFT	124
7.3	Electron density difference maps for the first three excitations of HP1	124
7.4	Relaxed geometry scan of θ_{tor} for HP derivatives	125
7.5	Relaxed geometry scan for ESIPT process.	126
7.6	Relaxed geometry scan of the torsional angle	127
7.7	PES for HP1 in vacuum and the solid state	128
7.8	MECI geometries for HC1 , HC5 & HP1	129
7.9	Emission spectra in molecular crystals	130
7.10	HR factors for HC1	133
7.11	HR factors for HC5	133
7.12	HR factors for HP1	134
7.13	Voronoi indices for HC and HP crystal structures.	135
7.14	Schematic of α , β , and γ angles for classification of dimers.	136
7.15	Example dimers in HC1 , HC5 , and HP1	136
7.16	Probability density maps of β and γ angles.	137
7.17	x -slip densities for dimer configurations of HC and HP systems	138
7.18	Electron density difference maps of the HP1 trimer.	139
7.19	Trimer exciton couplings	140
7.20	Exciton couplings in HC and HP systems	141

7.21	Correlation between the energy splitting and exciton coupling	143
7.22	Exciton hopping rates	145
A1	CASSCF space used in Chapter 5.	168
A2	The vacuum PES of HC1 & HC5	169
A3	Decay mechanism in the molecular crystal in M15 model	170
A4	CASSCF and CASPT2 space used in Chapter 7.	171

List of Tables

3.1	Molecular structures and their quantum efficiency of photoluminescence (Φ_{PL}) in the solid state	58
5.1	Vertical excitation energies of HC1-5	84
5.2	Calculated rates of population transfer between electronic states	91
5.3	Obtained rates for tautomer decay processes for compounds 1 and 5	94
6.1	Excitation energies in the solid state	109
6.2	Exciton coupling in dimers of HC1 & 5	110
6.3	Emission energies in the solid state	111
6.4	Relative energies with and without electrostatic embedding in monomer models .	115
6.5	Comparison of MECI angle parameters	116
7.1	Radiative decay rates in the solid state	131
7.2	Dimer types for HC and HP molecular crystals	142
7.3	Reorganisation energies and larges exciton hopping rates	146

List of Abbreviations

OLED	organic light-emitting diode
AIE	aggregation induced emission
ACQ	aggregation caused quenching
UV	ultraviolet
CT	charge-transfer
η_{QE}	external quantum efficiency
Φ_{PL}	quantum efficiency of photoluminescence
HR	Huang-Rhys
DRE	Duschinsky rotation effect
TICT	twisted intramolecular charge transfer
RIR	restriction of intramolecular rotation
RIV	restriction of intramolecular vibrations
RIM	restriction of intramolecular motions
TPE	tetraphenylethene
FGR-RIM	Fermi Golden Rule Restriction of Intramolecular Motions
RACI	restricted access to a conical intersection
ESIPT	excited state intramolecular proton transfer
GSIPT	ground state intramolecular proton transfer
HBT	2-(2-hydroxyphenyl)benzothiazole

NIR	near-infrared
HC	2'-hydroxychalcone
HP	2-hydroxyphenylpropenone
MM	molecular mechanics
DFT	density functional theory
HF	Hartree-Fock
PES	potential energy surface
MP2	Møller-Plesset perturbation theory to second order
CC	coupled cluster
ADC(2)	algebraic diagrammatic construction to second order
CAS	complete active-space
SCF	self-consistent field
CASSCF	complete active-space self-consistent field
RAS	restricted active-space
DFT	density functional theory
XC	exchange-correlation
LDA	local density approximation
GGA	generalized gradient approximation
RSH	range-separated hybrid
TDDFT	time-dependent density functional theory
MCTDH	multiconfigurational time-dependent Hartree
UFF	universal force field

ISC	inter-system crossing
FC	Franck-Condon
MECI	minimal energy conical intersection
NA-MQC	nonadiabatic mixed quantum-classical
TSH	trajectory surface hopping
LIIC	linear interpolation of internal coordinates
EDG	electron donating group
PCM	polarizable continuum model
RMSD	route-mean-square deviation

*Uncertainty is an uncomfortable position. But certainty is an
absurd one.*

Voltaire

1 Introduction

1.1 Background

Luminescent organic molecules are used in numerous biological and technological applications. In aqueous solution they are employed extensively in biological imaging, probing, and detection. Deposited as thin films and aggregates, they represent the next generation of organic optoelectronics, where availability and low cost of starting materials, straightforward syntheses, and lightweight, flexible devices are attractive features. Perhaps most importantly, the luminescent response of molecular organic systems can be tuned with relative ease compared to their inorganic counterparts.¹

Since the discovery of electroluminescence in the 1960s, intensive efforts in academia and industry have delivered considerable progress in the field of organic electronics, leading to the development of applications such as field-effect transistors, photovoltaic cells, optical memory devices, and single-crystal lasers.² The most prominent success stories are certainly organic light-emitting diodes (OLEDs), which have already reached market adoption for lighting and display purposes. However, in many areas organic systems suffer from low efficiencies, trial-and-error optimisation, and decreased performance in aggregated form versus solution. To advance, there must be control over both the supermolecular structure of the material and the electronic structure of the molecules within. Neither property exists in isolation, and their interplay must also be understood, which somewhat complicates matters. Of these contributing factors, it is the electronic structure and its relationship with the environment which are of interest in this work. The luminescent response of molecules can change drastically from one medium to another, whether in the gas phase, as a solution, aggregated as clusters, or in molecular crystals. This thesis focuses on understanding the interplay between the luminophore and its environment, crucial for designing more efficient materials from first principles.

We approach the problem using computational chemistry methods to investigate organic compounds exhibiting aggregation induced emission (AIE). AIE-active compounds are non-emissive

in dispersed media, but undergo a switch-on of luminescence, typically in the form of fluorescence, upon aggregation.³ Since technological applications require a thin-film or solid-state layer, AIE has attracted considerable interest as a pathway to overcome the common effect of aggregation caused quenching (ACQ), hitherto a major obstacle in the development of organic luminophores. The potency of AIE systems can be further boosted by incorporating excited state intramolecular proton transfer (ESIPT) into the chromophore, where the large Stokes shift separates emission from absorption and increases the quantum yield of fluorescence.⁴

We study two families of related compounds which all undergo ESIPT but with a range of differing luminescent behaviour in the solid state. None of the eleven compounds emit with any potency in dispersed phase. However, when crystalline, inter- and intramolecular interactions result in markedly different fluorescent quantum yields. We wish to understand both of these phenomena; why the systems do not fluoresce as single molecules, why some of the compounds *do* fluoresce when aggregated, and why some fluoresce more efficiently. From a mechanistic view, just as important are the systems which are non-emissive in either phase. We address these phenomena by probing the excitation-decay photocycle of these systems in both vacuum and aggregated phase through their potential energy surfaces (PESs), constructing feasible energy pathways to attest their observed properties. We determine the various competing decay pathways and identify the factors which drive them. This enables us to determine the fundamental mechanisms dictating the observed phenomena, from which we elucidate design rules to aid the development of luminescent organic materials which incorporate the ESIPT effect.

1.2 Thesis Framework

Starting from the experimental discovery of the AIE of a range of 2'-hydroxychalcones (HCs) compounds, we took a three step approach in probing the excitation-decay mechanism of these systems. These steps make up Chapters 5-7 of the thesis. First, we study five compounds and determine why none fluoresce in good solvent, and how electronic substituents influence the excited state decay. Next, we take two of the systems with differing fluorescence properties and model the decay mechanism in the solid state. Our approach isolates both the effect of both inter- and intramolecular interactions, and rationalises the observed behaviour of the compounds. Finally, we take our mechanistic understanding and apply it to a set of related systems, showing that the

mechanism is robust and descriptive. From our results we derive a set of design rules to boost the quantum yield of molecular organic crystals.

In the next Chapter we introduce the theoretical foundations for the thesis. These are rooted in quantum chemistry, and we examine the Schrödinger equation and the Born-Oppenheimer Approximation before turning to the fundamental photophysical and photochemical principles which dictate the luminescent response of molecules and materials. Single molecule excitation and decay concepts are examined first, with particular attention paid to electronic state crossings, known as conical intersections. These concepts are directly important for the mechanistic study of the nonradiative decay mechanisms in vacuum in Chapter 5. When single molecules aggregate in the solid state, their photobehaviour is influenced by intermolecular interactions due to the close proximity of neighbouring molecules. We explore these effects in the context of exciton theory, a highly successful framework in which to view excited state processes of aggregates, employed in Chapters 6 and 7.

In Chapter 3 the AIE and ESIPT phenomena are established through analysis of typical structures and mechanistic interpretations. We then introduce the systems under investigation. 2'-hydroxychalcone (**HC**) compounds have a donor-acceptor structure and undergo ESIPT, where substituent identities and molecular packing determine the AIE response. In contrast, the four molecules of the 2-hydroxyphenylpropanone (**HP**) family combine ESIPT with a remarkable AIE response. At the end of Chapter 3 we survey the experimental studies on these systems.

In Chapter 4, we overview the computational methods which have been used in this work. The excited state methods applied in this thesis are introduced, detailing their strengths, weaknesses and areas of application. In the final sections of Chapter 4, we examine hybrid methods, which enable excited state calculations of molecular crystals to be computational tractable.

In Chapter 5, we present a study of the vacuum photochemistry of five **HC** compounds synthesised by Cheng and coworkers (Figure 3.5). Here the vertical excitations, PESs and nonadiabatic dynamics of the family are studied to determine the nonradiative decay pathways and rationalise the nonemission of these compounds.

In Chapter 6 the focus moves to the crystalline photochemistry for the **HCs**. Using a hierarchy of QM:MM models, we construct the PES and the decay pathway in the excited state for two systems with differing emission behaviour using density functional and multireference methods. The methods employed consider exciton coupling, long and short range electrostatics, and cluster

size, to decouple the different factors responsible for the observed photobehaviour. This gives a comprehensive mechanism of the excited state decay in the main **HP**s systems. With our results, we establish design rules for efficient ESIPT emitters.

In Chapter 7, the scope of our work is expanded to consider the **HP** family, as well as two additional **HC** compounds which undergo AIE. In total we consider eleven compounds to understand the remarkable efficiency of the **HP** family and to test the design rules established in Chapter 6. A quantitative description of the crystal morphologies is developed, based upon the dimer configurations present. The thesis concludes with an overview of the main results, and how these precipitate the design rules for more efficient organic luminescent materials.

2 Theoretical Framework

2.1 Quantum Mechanics and Chemistry

2.1.1 Overview

This chapter introduces the key concepts upon which the work of this thesis relies, starting with the advent of quantum mechanics and quantum chemistry. The development of quantum mechanics in the early 20th century armed scientists with the tools to calculate the microscopic properties of matter. In chemistry, the postulates of quantum mechanics can be applied to calculate relative energies of molecules, molecular geometries, ratios of products of chemical reactions, transition states, spectra, and any other phenomenon of interest. However, whilst in principle any property can be calculated exactly by the Schrödinger equation, the analytical solution is only obtainable for systems with one electron. For systems larger than this, and therefore anything of observable chemical relevance, the computational expense on even modern computer architecture is intractable.

To overcome this, a number of approximations are used in the field of computational chemistry to solve the multielectron problem. In general, as the number of atoms one wants to model increases, qualitative nature of the result also increases. Computational chemistry methods can generally be split into the types of approximations made and the number of atoms the method wishes to treat. In biophysical process and the modelling of proteins on the scale of tens of thousands of atoms, quantum mechanics is ignored completely. Force fields are used to calculate the energy corresponding to a set of atomic coordinates in what are known as the molecular mechanics (MM) class of methods. The interactions between atoms are defined by analytical potentials, such as for bond stretches, bends, and angles, and are parameterised for different types of molecules using more accurate methods. This procedure is time-consuming and makes the force field specific to the systems it was fitted to, but enables computationally facile access to molecular geometries and properties of large systems.⁵

At the other end of the scale, the electronic structure can be tackled through wavefunction

or density functional theory (DFT) methods. For the applications involved in this thesis, involving photoinduced phenomena, the activity of the electrons is paramount, and as such it is these methods which are utilised herein. In the next sections, the importance of the Schrödinger equation shall be established, which along with the Born-Oppenheimer approximation form the backbone of quantum chemistry and quantum chemical methods. Following this the idea of the potential energy surface (PES) is introduced, providing the context and framework for molecular photochemistry principles. We then expand this by considering the photochemistry of aggregates, namely dimers within the exciton model, and how to incorporate their effects into mechanistic models.

2.1.2 The Schrödinger Equation

The wavefunction Ψ contains all the information about the quantum state of the system at a position and time. As Newton's second law ($\mathbf{F} = m\mathbf{a}$) gives a classical particle's position and momentum at each time period, thus describing its classical state, so the time-dependent Schrödinger equation does for wavefunction, and has the general form

$$i\hbar \frac{\partial \Psi(\mathbf{R}, \mathbf{r}, t)}{\partial t} = \hat{H}\Psi(\mathbf{R}, \mathbf{r}, t) \quad (2.1)$$

where $\hbar = \frac{h}{2\pi}$ and \hat{H} is the Hamiltonian operator for electrons at \mathbf{r} and nuclei at \mathbf{R} . Separating the spatial part from the temporal part yields the time-independent version of the Schrödinger equation, which using the bra-ket notation of Dirac is⁶

$$\hat{H}|\Psi\rangle = E|\Psi\rangle. \quad (2.2)$$

This is an eigenvalue equation, where the Hamiltonian operator acts on the wavefunction to give the energy E of the system. For a system of N electrons and M nuclei, the Hamiltonian calculates the kinetic (T) and potential (V) energy contributions of the electrons and nuclei towards the total energy of the system,

$$\hat{H} = \hat{T}_e + \hat{T}_n + \hat{V}_{n-e} + \hat{V}_{e-e} + \hat{V}_{n-n} \quad (2.3)$$

$$\hat{H} = \underbrace{-\sum_{i=1}^N \frac{1}{2} \nabla_i^2 - \sum_{A=1}^M \frac{1}{2M_A} \nabla_A^2}_{\text{kinetic terms}} - \underbrace{\sum_{i=1}^N \sum_{A=1}^M \frac{Z_A}{r_{iA}} + \sum_{i=1}^N \sum_{j>i}^N \frac{1}{r_{ij}} + \sum_{A=1}^M \sum_{B>A}^M \frac{Z_A Z_B}{R_{AB}}}_{\text{electrostatic terms}} \quad (2.4)$$

where i and j are electrons and A and B are nuclei. Atomic units are used, where physical constants such as electronic charge and mass are unity. The first two terms are the operators for the kinetic energy of the electrons and the nuclei, where the Laplacian operator ∇^2 is the second derivative of position. The next three terms are the electrostatic operators, summing the Coulomb interactions in the system; the attractive interaction between electrons and the nuclei (of charge Z); the repulsive interaction between electrons; and the repulsive interaction between nuclei. Atomic units are used throughout, such that the electronic charge and mass are neglected. The R and r terms in the electrostatic parts denote the distance between nuclei and electrons respectively.

In the hydrogen atom, the \hat{V}_{e-e} and \hat{V}_{n-n} are neglected since there is only one proton and one electron, and the exact solution for the energy can be calculated since the wavefunction can be constructed analytically. However, for larger systems with many electrons and nuclei, Equation 2.2 cannot be solved. As such, a number of approximations must be made. The most fundamental of these is Born-Oppenheimer approximation.

2.1.3 The Born-Oppenheimer Approximation

Separation of variables is a key concept in quantum chemistry, where a complex problem is broken down into constituent parts. This method is used to simplify the solving of Equation 2.2 by separating the electronic terms from the nuclear terms, and is known as the Born-Oppenheimer Approximation⁷

$$\Psi_{BO}(\mathbf{R}, \mathbf{r}) = \Theta(\mathbf{R}, \mathbf{r})\Phi(\mathbf{r}) \quad (2.5)$$

where $\Theta(\mathbf{R}, \mathbf{r})$ is the nuclear wavefunction and $\Phi(\mathbf{r})$ is the electronic wavefunction. The separation of terms is rooted in the fact that the nuclei are vastly heavier than electrons, and so it can be approximated that the nuclei are static with respect to the electrons. The Schrödinger Equation is solved then, in two steps. First, the electronic wavefunction Φ is calculated with “clamped” nuclei, resulting in an electronic energy which is a parametric function of the nuclear coordinates.

By concentrating on just the electronic terms, the *electronic* Hamiltonian \hat{H}_e becomes

$$\hat{H}_e = \underbrace{-\sum_{i=1}^N \frac{1}{2} \nabla_i^2}_{\text{kinetic term}} - \underbrace{\sum_{i=1}^N \sum_{A=1}^M \frac{Z_A}{r_{iA}} + \sum_{i=1}^N \sum_{j>i}^N \frac{1}{r_{ij}}}_{\text{electrostatic terms}}. \quad (2.6)$$

and the electronic Schrödinger equation is then

$$\hat{H}_e |\Phi\rangle = E_e |\Phi\rangle. \quad (2.7)$$

In a similar vein, the nuclear part can also be solved where the electronic coordinates are replaced by their averaged values and the nuclear Hamilton \hat{H}_n is⁸

$$\hat{H}_n = -\sum_{A=1}^M \frac{1}{2M_A} \nabla_A^2 + \left\langle -\sum_{i=1}^N \frac{1}{2} \nabla_i^2 - \sum_{i=1}^N \sum_{A=1}^M \frac{Z_A}{r_{iA}} + \sum_{i=1}^N \sum_{j>i}^N \frac{1}{r_{ij}} \right\rangle + \sum_{A=1}^M \sum_{B>A}^M \frac{Z_A Z_B}{R_{AB}} \quad (2.8)$$

In the Born-Oppenheimer approximation, solving the electronic problem provides a potential which governs the motion of the nuclei. This potential is known as the potential energy surface (PES).⁸ The total wavefunction Ψ considering multiple electronic states can be constructed from the combination of the electronic functions for each state I and the corresponding nuclear wavefunction Θ_I in what is known as the Born-Huang expansion⁹

$$\Psi(\mathbf{R}, \mathbf{r}) = \sum_I \Theta_I(\mathbf{R}, \mathbf{r}) \Phi_I(\mathbf{r}). \quad (2.9)$$

This approach is used to reconstruct the wavefunction in nonadiabatic dynamics simulations (Section 2.2.3).¹⁰ When the nuclei are stationary, their kinetic energy is zero and the complete Hamiltonian is just the electronic Hamiltonian. For vibrating molecules, Equation 2.7 is solved at the required nuclear configuration, for electronic state I , and the time-evolution of the nuclear wavefunctions is¹¹

$$i\hbar \frac{\partial \Theta_I}{\partial t} = [T_n + E_I] \Theta_I - \underbrace{\sum_I \hat{\Lambda}_{JI} \Theta_I}_{\text{Nonadiabatic couplings}} \quad (2.10)$$

where the energy of E_I is the expectation value of the electronic Hamiltonian ($\langle \Phi_I | \hat{H}_e | \Phi_I \rangle$). The highlighted *nonadiabatic coupling* operator $\hat{\Lambda}_{JI}$ couples electronic state I with electronic state

J . In the adiabatic Born-Oppenheimer approximation, this coupling is completely neglected and the time-evolution of the nuclei becomes¹²

$$i\hbar\frac{\partial\Theta_I}{\partial t} = [\hat{T}_n + E_I]\Theta_I \quad (2.11)$$

The nuclear motion is thus determined by the electronic energy of uncoupled *adiabatic* states, and the nuclei move on the PES of state I . $\hat{\Lambda}_{JI}$ contains the nonadiabatic couplings, which become important when electronic states converge in energy. This shall be discussed in Section 2.2.2 The Born-Oppenheimer approximation helps divide the problem into electronic and nuclear parts. However, solving the electronic problem exactly for many electron systems is impossible. In Chapter 4 we shall explore the methods which have been developed to approximate the exact formulation of the wavefunction. Next, however, we turn our attention to photo-induced chemical processes, which are at the of this work. We start with single molecule phenomena before expanding to the photophysics of molecular aggregates.

2.2 Molecular Photochemistry

2.2.1 Fundamental Principles

Modelling electronically excited states is a considerably complex task, in terms of both the number of possible reaction paths and the methods needed to describe them. Some of these pathways are illustrated in Figure 2.1. The potential energy surface (PES) is absolutely central in understanding excited-state processes. It is through probing the minima and gradients of the PES that feasible pathways, and thus chemical mechanisms, are elucidated and physical observables are rationalised theoretically.¹¹

Electronic excitation, induced by irradiation from the ultraviolet (UV) or visible range, will normally occur at the thermal equilibrium geometry in the ground state. Absorption of a photon will place the system in an electronically excited state. According to the Franck-Condon (FC) Principle, the nuclei will undergo negligible instantaneous change upon change in electronic state.¹³ This region of the PES is called the FC region, or point, and the electronic excitation is considered to be vertical (directly to the point of the upper PES vertically above the ground state). From here, a multitude of relaxation processes are possible with vastly different timescales.

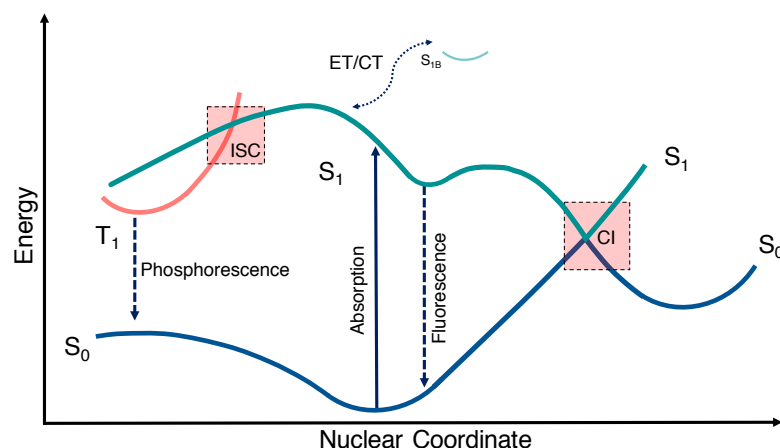


Figure 2.1: Competing relaxation pathways after electronic excitation to the first excited singlet state (S_1). Nonradiative decay channels through conical intersections (CI), energy transfer (ET) and charge transfer (CT) to other molecules, compete with fluorescence. Alternatively, intersystem crossing (ISC) can occur, followed by phosphorescence.

The fastest process is typically relaxation to lowest vibrational state, occurring in femtoseconds. The system will follow the nuclear coordinate with the largest electronic gradient to a minimum on excited surface, followed by fluorescence. At the other end of the scale, if there is significant spin-orbit coupling, crossing to a triplet state through inter-system crossing (ISC) followed by phosphorescence can take milliseconds.

Calculating the relative energies of these relaxation pathways is a challenging task for a number of reasons. Firstly, whilst Figure 2.1 is a one-dimensional cut of a specific nuclear coordinate, the true PES is a $3N-6$ ($3N-5$ for a linear molecule) hypersurface of nuclear degrees of freedom. As such the full surface cannot feasibly be sampled for large molecules. Secondly, ground state methods must be tweaked or expanded upon to incorporate excited states. As such, not all excited state methods are created equal, where a careful choice of method must be made depending on the region of the PES one is interested in. This shall be expanded on in Chapter 4. Thirdly, and perhaps most importantly, in certain regions of the PES the fundamental principle of quantum chemical methods, the Born-Oppenheimer approximation, breaks down altogether. Such regions occur when two electronic states become close in energy, as highlighted in red in Figure 2.1. In this region, the electronic states become directly coupled with the nuclear motion, breaking the Born-Oppenheimer approximation. These “funnel” regions, or conical intersections, are ubiquitous in photophenomena.^{11,14–18}

2.2.2 Conical Intersections

In photochemical processes with well-defined, well-separated electronic states, the adiabatic Born-Oppenheimer approximation is valid. That is, the nuclear wavefunction of an electronic state is independent from the nuclear wavefunction of another state. However, as shown in Figure 2.1, in photochemical processes there are regions on the energy landscape where electronic states become close in energy. In these regions, small changes in nuclear configuration results in large changes in the electronic wavefunction - hence the separation of nuclear and electronic wavefunctions is no longer valid and the Born-Oppenheimer approximation breaks down.¹⁷ In practice, this means that the nonadiabatic coupling terms become important and can no longer be neglected.

The coupling operator $\hat{\Lambda}$ of Equation 2.10 has matrix elements

$$\hat{\Lambda}_{JI} = \delta_{JI}\hat{T} - \langle \Theta_J | \hat{T} | \Theta_I \rangle. \quad (2.12)$$

These couple the nuclear and electronic coordinates, describing the dynamic relationship between these degrees of freedom. By setting

$$\hat{T} = -\frac{1}{2M}\nabla^2 \quad (2.13)$$

the nonadiabtic coupling operator can be written as¹¹

$$\hat{\Lambda}_{IJ} = \frac{1}{2M}(2\mathbf{F}_{JI} \cdot \nabla + G_{JI}) \quad (2.14)$$

where ∇ the first derivative of position and

$$\mathbf{F}_{JI} = \langle \Phi_I | \nabla | \Phi_J \rangle \quad (2.15)$$

is the derivative or nonadiabatic coupling vector with respect to position. G_{JI} is the scalar coupling,

$$G_{JI} = \langle \Phi_I | \nabla^2 | \Phi_J \rangle. \quad (2.16)$$

\mathbf{F}_{JI} is a $3N$ -vector coupling the nuclear motion of electronic state I with state J . The total value is given by the scalar product of \mathbf{F} with the nuclear momentum, and so the size (and thus the

probability of a transition) is defined by the size of the coupling as well as the momentum of the nuclei.¹¹ The derivative coupling F_{JI} can be expressed in terms of the electronic Hamiltonian H_e , such that

$$F_{JI} = \frac{\langle \Phi_I | \nabla \hat{H}_e | \Phi_J \rangle}{E_J - E_I}. \quad (2.17)$$

With large electronic energy differences, the mass difference between electrons and nuclei make F_{JI} inconsequentially small. However, as states converge the coupling increases. Only two coordinates can lift complete degeneracy, resulting in the PES forming a double-cone structure. Conical intersections thus act as funnels, where the wavepacket can transfer nonradiatively between electronic states in an ultrafast timeframe. The two degrees of freedom define the branching space vectors. The first is the gradient difference vector \mathbf{g} , defining the difference between the gradients of the upper and lower PESs,

$$\mathbf{g}_{JI} = \langle \Phi_I | \nabla \hat{H}_e | \Phi_I \rangle - \langle \Phi_J | \nabla \hat{H}_e | \Phi_J \rangle. \quad (2.18)$$

The second is the nonadiabatic coupling vector \mathbf{h} , defining the direction of strongest coupling between states, which is the numerator of Equation 2.17,

$$\mathbf{h}_{JI} = \langle \Phi_I | \nabla \hat{H}_e | \Phi_J \rangle. \quad (2.19)$$

The vectors \mathbf{g} and \mathbf{h} are orthogonal, defining the plane of the conical intersection. The vector \mathbf{g} points in the direction of removing the energetic splitting, whilst \mathbf{h} points towards maximising the nonadiabatic coupling.¹⁹ This is depicted in Figure 2.2. Important to note is that for polyatomic molecules the conical intersection is not an isolated point but multidimensional. Displacement through any of remaining $3N-8$ coordinates will retain the degeneracy, with the system moving on a degeneracy seam between the two surfaces.

2.2.3 Dynamics Simulations of Excited State Processes

Simulation of the temporal evolution of photoinduced processes is a powerful method for probing excited state PESs. Treating both nuclear and electronic motion fully quantum mechanically, with the required nonadiabatic couplings, is unfeasibly expensive for all but the smallest molecular systems. As with all quantum chemical approaches, approximations are made. To retain the

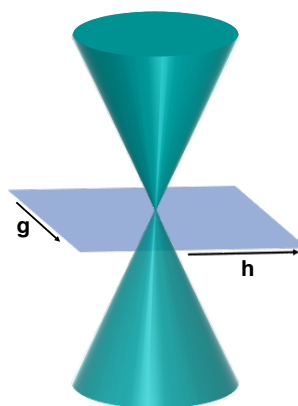


Figure 2.2: Schematic of the double-cone topology of degenerate electronic states. The gradient difference vector \mathbf{g} and the nonadiabatic coupling vector \mathbf{h} define the branching space lifting the degeneracy.

quantum description of the nuclei, specific nuclear modes can be sampled to reduce the dimensionality of the configuration space and the associated computational cost, which is often done in the multiconfigurational time-dependent Hartree (MCTDH) method, which can reproduce the exact quantum mechanical molecular wavefunction through the Born-Huang expansion (Equation 2.9).¹¹ Alternatively, the nuclear motion can be treated classically and allowed to explore the configuration space determined by the electronic PESs.

The second approach, nonadiabatic mixed quantum-classical (NA-MQC), shall be used in elements of this thesis with the trajectory surface hopping (TSH) method. The most prominent NA-MQC methods are TSH, mean-field Ehrenfest, and multiple spawning.¹⁰ In Ehrenfest dynamics, a nuclear trajectory is calculated using a weighted-average of a predefined number of electronic states. In multiple spawning, a series of Gaussian functions describe the nuclear wavepacket propagating on electronic surfaces. In the vicinity of state crossings, more Gaussian functions are spawned to follow each electronic state. With TSH, a set of independent trajectories approximate the wavepacket propagation, with electronic transitions determined stochastically, most commonly using Tully's fewest-switches algorithm.²⁰ TSH is perhaps the mostly used algorithm for simulating NA-MQC dynamics, where the Newtonian propagation of the nuclei, on-the-fly quantum chemical calculations, and straightforward parallelisation have encouraged wide adoption.²¹

In TSH, the nuclei propagate classically on a single, adiabatic electronic surface, governed by

$$\frac{d^2 \mathbf{R}}{dt^2} = \frac{\mathbf{F}}{M} \quad (2.20)$$

where the force \mathbf{F} is proportional to the electronic gradient of the current state I

$$\mathbf{F} = -\nabla \langle \Phi_I | \hat{H}_e | \Phi_I \rangle. \quad (2.21)$$

The nuclear motion is integrated typically using the velocity Verlet algorithm.²² At each nuclear timestep, the electronic evolution is governed by the time-dependent Schrödinger equation, where the wavefunction is approximated as a linear combination of K electronic states ψ

$$\Phi = \sum_K c_K \psi_K, \quad (2.22)$$

allowing the Schrödinger equation to propagate through the coefficients c

$$\frac{dc_I}{dt} = \sum_K -c_K \left(\frac{i}{\hbar} H_{IK} + \Lambda_{IK} \right) \quad (2.23)$$

where H collects the energies and Λ the nonadiabatic couplings. The time-derivatives of the nonadiabatic couplings can be computed through wavefunction overlaps from previous time steps, for example using a finite differences procedure.^{23,24} Alternatively the couplings can be directly calculated.¹⁰

The initial state (at $t = 0$) can be chosen based upon the oscillator strengths for the nuclear configuration in question. During propagation, the current state can change, or 'hop', from I to J based upon a probability P defined by

$$P_{I \rightarrow J} = \max \left[0, \frac{-2\Delta t}{|c_I|^2} \text{Re}(\Lambda_{IJ} c_J c_I^*) \right] \quad (2.24)$$

which gives a hopping probability number P . For the hop $I \rightarrow J$ to occur, a randomly sampled number $r_t([0, 1])$ is used to evaluate

$$\sum_{K=1}^{J-1} P_{I \rightarrow K} < r_t \leq \sum_{K=1}^J P_{I \rightarrow K} \quad (2.25)$$

A further condition that the energy does not increase after a hopping is also enforced. The nuclear equations are typically integrated in steps of 0.5 fs, while the electronic structure calculations are performed at these timesteps with interpolation between them to account for the faster oscillations, to reduce the computational expense. Generally, the algorithm for TSH involves the following steps:

1. Calculate electronic energies, gradients and nonadiabatic coupling terms for a specific nuclear configuration
2. Integrate Equation 2.23
3. Evaluate the hopping probability from Equation 2.24 and determine the current state from Equation 2.25
4. Propagate the nuclei to a new configuration by integrating Equation 2.20

These steps are repeated until the maximum time for the simulation is reached, which is normally a pre-determined maximum timeframe. An ensemble of trajectories is computed, where the above algorithm is carried out for many starting nuclear configurations to obtain the average wavepacket propagation. The most computationally demanding step is the first, where the electronic properties are calculated at each time step.

The number of trajectories in the ensemble is important for proper evaluation of the configuration space. However, even with an infinite ensemble, the quantum features of the nuclear motion are generally missed in TSH. This is due to the decoherence problem, where off-diagonal terms of the density matrix do not vanish during the dynamics. This is a direct result of the propagation along a single surface, which artificially prevents the amplitudes following other gradients and quickly vanishing.¹⁰ By applying a decoherence correction to the energy in Step 2., the TSH average population of the independent trajectories should mimic the quantum behaviour if enough trajectories are sampled.²⁵ Further corrections in TSH must be made in order to preserve kinetic energies in case of frustrated hopping events, where Equation 2.24 is fulfilled but the energy condition is not.

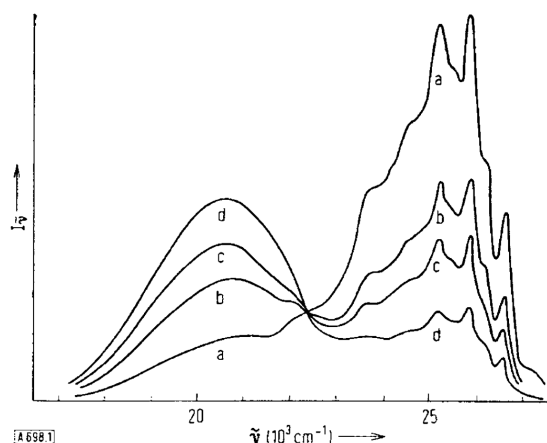


Figure 2.3: Fluorescence spectrum of pyrene (in n-heptane, 20°C) at different concentrations: a) 5.0×10^{-5} , b) 1.8×10^{-4} , c) 3.1×10^{-4} , d) 7.0×10^{-4} molL⁻¹. Reprinted from ref. 27 with permission of Wiley-VCH.

2.3 Photophysics of Molecular Aggregates

2.3.1 Molecular Stacking

Photoinduced luminescence occurs after chromophores with π -conjugation, typically in the form of aromatic moieties, absorb light in the UV or visible region of the electromagnetic spectrum. Fluorescence will usually follow, although the presence of metals or second row elements can allow phosphorescence *via* intersystem crossing. Upon aggregation with increased concentration, or crystallisation, the fluorescence is often reduced or quenched completely.

In 1954, photochemistry pioneer Theodor Förster elegantly showed that the fluorescence of pyrene is shifted and weakened with increasing concentration (Figure 2.3).^{26,27} Aromatic rings in conventional luminophores lead to intermolecular π - π interactions and the formation of dimers. In the case of pyrene, as the concentration increases a new fluorescent species is formed and the original emission band loses intensity. Since the absorption spectrum is unchanged in the concentration range, the arising band can be “attributed to an associate that exists only in the excited electronic state, i.e. to an excimer.”²⁷ The formation of excimers can be detrimental to the fluorescence of organic systems.

The supermolecular alignment of aromatic groups is commonly termed π -stacking or π - π interactions in the chemical literature. However, this labelling can be slightly misleading and

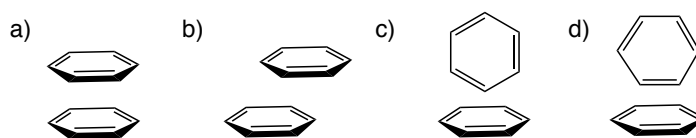


Figure 2.4: Packing arrangements of benzene molecules: a) face-centred, b) displaced, c) Perpendicular T-shaped, d) Perpendicular Y-shaped. Adapted from ref. 29.

even inaccurate.^{28,29} It is argued by Grimme that a specific π - π interaction arises only in large, polyaromatic groups as a result of increased dispersion in specific orientations.²⁸ Meanwhile, a thorough review of experimental and theoretical literature by Martinez and Iverson found a lack of the face-centred stacking of aromatic groups which would maximise overlap of aromatic π clouds.²⁹ They argue that the terms π -stacking and π - π interactions are misnomers since they incorrectly imply the ubiquity of face-face stacking configurations. Typical stacking arrangements are shown in Figure 2.4, where parallel displacement tempers the unfavourable electrostatic interaction and reduces the Pauli exchange repulsion, with the dominating factor being the favourable dispersion interaction. Inclusion of substituents introduces a permanent dipole, with substituents preferentially aligning antiparallel.²⁹

This intermolecular interaction is detrimental to solid-state fluorescence, and yet is a direct consequence of the design requirements of the chromophore. Researchers have developed numerous strategies to overcome this effect. In biosensing applications, work is often carried out in dilute solutions with reduced sensitivity because of ACQ.^{30,31} In the solid state, for instance in thin films for optoelectronics, the ACQ effect means that solution screening for viable candidates is rendered meaningless by the differing luminescent properties of the final material compared to the molecule. Strategies to circumvent ACQ have seen varying success, for example through the inclusion of bulky substituents, polar groups, and promotion of hydrogen bonding.^{1,3,32,33} However, synthetic modification can in turn affect the chromophore's electronic structure and its excited state properties, thus commencing a tedious trial-and-error optimisation process. Attempts to physically block aggregation by encapsulating in surfactants or polymer matrices require extensive engineering and can reduce charge transport.^{32,34,35}

The deleterious effects of ACQ cannot be underestimated and pose a significant problem for organic luminescent applications. In the next section, we shall look in more detail of the photo-physics of molecular aggregates, within the context of Kasha's exciton theory.

2.3.2 Exciton Theory

Intermolecular interactions become photophysically important in the solid state due to the dense packing of molecular units. This effect is typically framed in Kasha's two state exciton theory.^{36–40} The exciton is typically defined as a delocalised excited state, where the excited electron and hole remain in close proximity. The Coulomb interaction between the transition dipoles of the monomers in a dimer results in an energy shift in the absorption spectrum, and has underpinned exciton theory since its inception in the 1960s.⁴¹ When two monomers stack "side-by-side" with parallel transition dipole moments, the Coulombic excitonic coupling is positive, a blue-shifted absorption spectrum is witnessed (relative to the isolated monomer) and radiative decay is reduced. This stacking arrangement is denoted an H-aggregate. Conversely, in J-aggregates, dimers align "head-to-tail", and a red-shifted absorption is witnessed with an increased radiative decay. These two extreme cases are depicted in Figure 2.5, and have helped interpret the supermolecular photophenomena in molecular aggregates.

When the intermolecular distance is large enough to minimise orbital overlap, the exciton can be considered as the interaction of the wavefunction of one monomer ($|1\rangle$) with the wavefunction of the second monomer ($|2\rangle$). In the excited state, the wavefunctions interact to form an exciton, the Hamiltonian \hat{H} of which is given by

$$\hat{H} = \hbar\omega + \hbar D + J_{12} |1\rangle \langle 2|. \quad (2.26)$$

The first term is the energy gap between S_0 and S_1 , $\hbar D$ is the shift of the S_1 state in going from the vacuum to the crystal, and J_{12} is the Coulombic coupling between molecules 1 and 2.⁴² The ket $|1\rangle$ represents the state where molecule 1 is excited to S_1 and molecule 2 remains in the ground state. For a many-chromophore system (more than two molecules), the exciton can be described using periodic boundary conditions to produce a wavelike function k . For the two site system, $|k\rangle$ is⁴³

$$|k\rangle = \frac{1}{\sqrt{2}} [e^{ik} |1\rangle + e^{i2k} |2\rangle] \quad k = 0, \pm\pi. \quad (2.27)$$

For the allowed values of k , the transition energy E_k for state k is an eigenvalue of \hat{H} , and has the form

$$E_k = \hbar\omega + \hbar D + J_{12} \cos k. \quad (2.28)$$

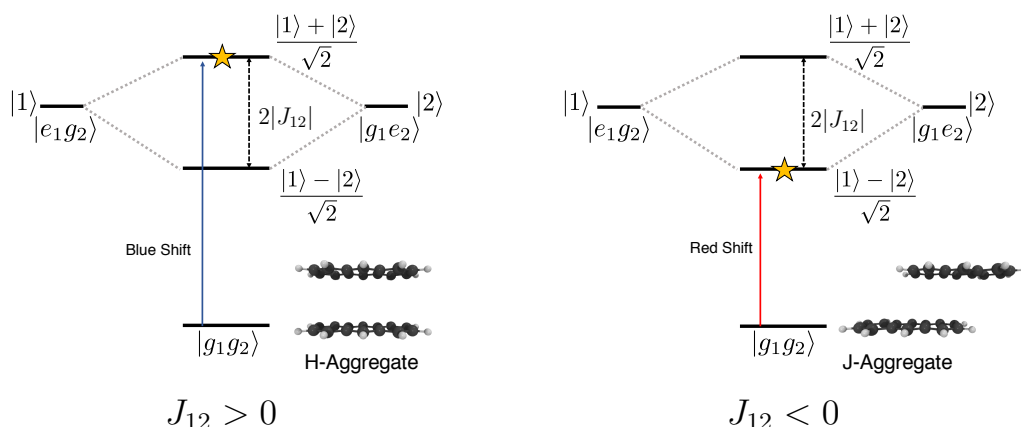


Figure 2.5: Energy level diagram for a H-aggregate (left) and J-aggregate (right) of naphthalene. For the H-aggregated, the Coulombic coupling J is positive, raising the energy of the symmetric state resulting in blue-shifted absorption with respect to the monomer state. Emission from the lower state is forbidden, and thus quenched. In the J-aggregate, the negative Coulombic coupling results in red-shifted absorption and allowed emission. The bright excitonic state, the symmetric superposition of the monomer wavefunctions, is indicated with a star.

For the two site system, this results in two exciton states in the Frenkel Hamiltonian, as depicted in Figure 2.5. The Coulomb coupling J represents the interaction energy due to exchange of excitation energy between $|1\rangle$ and $|2\rangle$, the sign of which dictates whether the symmetric superposition is the upper or lower state. When the coupling is positive, the symmetric state is the upper state, as in the H-aggregate, and the transition dipoles are reinforced resulting in blue-shifted absorption compared to the gas-phase monomer. Since Kasha's rule dictates that emission will usually take place from the lower state, the state is nonradiative and fluorescence is quenched.⁴⁴ When the coupling is negative, the symmetric state is lowered and emission is symmetry allowed.³⁹ H- and J-aggregates represent the two extreme stacking cases.

Understanding the complex photophenomena of molecular aggregates is important in the development of materials requiring control over the exciton. The existence of excitons and the dynamics in the solid state opens nonradiative decay channels and often a quenching of fluorescence for typical aromatic systems due to the prominence of H-aggregates. This has hindered the development of solid-state organic luminescence.

2.3.3 Exciton Transport Regimes

The understanding and control of the exciton dynamics has great fundamental and technological importance in organic crystals and materials. In organic semiconductors, light-emitting diodes, and solar cells, having fast exciton diffusion through the material is highly desirable. The transport of an exciton through a material is mainly governed by the exciton coupling J between sites. Disorder in the material causes exciton localisation. Dynamic disorder causes exciton localisation due to low frequency modes in these molecular systems, where the vibrations cause a fluctuation in the exciton coupling. Static disorder, on the other hand, is more common when there is an inherent difference in the site energies of molecular units.⁴⁵

In general, exciton transport is viewed between two extreme regimes in organic crystals. These two regimes involve the competition between two parameters; the exciton coupling J and what is known as the electron-phonon coupling. The electron-phonon coupling, or reorganisation energy (see Section 3.2.2) is the relaxation energies when one molecule relaxes on its PES as it changes electronic state (either from ground to excited, or vice versa) and its neighbour undergoes the opposite process.

In the coherent transport regime, the exciton coupling is far greater than the magnitude of the exciton-phonon coupling. When this is the case, the exciton is delocalised over the whole aggregate.² In contrast, in the incoherent regime, the exciton-phonon coupling outweighs the exciton coupling to localise the excited state on one unit. In this regime, the exciton will stochastically “hop” between neighbouring units.⁴⁶ Thermal motions can modify the strength of the exciton coupling, in particular the short-range contribution which is highly distant dependent.⁴⁷

Modelling these processes is extremely complex in molecular crystals, in particular when we move away from the extreme cases of coherent or incoherent transport. Band theory poorly describes the coherent regime by underestimating the diffusion length, while incoherent regime models overestimate the hopping rate.⁴⁸ The work of Troisi *et. al.* has explored how these processes in organic crystals, where thermal fluctuations can influence the magnitude of the exciton coupling and how this influences the diffusion.^{46,49–51} In Chapter 7, we examine how the competition between the exciton coupling and reorganisation energy in the ES IPT systems affects the photorelaxation mechanism.

2.3.4 Approaches to Calculate Exciton Couplings

Quantum chemical methods allow for the calculation of the coupling parameter J for two monomers, in general labelled i and j , in a molecular dimer. In Kasha's exciton theory, the coupling J_{ij} arises from the interaction of the transition dipole moments, which at its most crude can be treated as the interaction between two point dipoles,

$$J_{ij} = \frac{\mu^2(1 - 3 \cos^2 \theta)}{4\pi\epsilon R^3} \quad (2.29)$$

where R is the intermolecular distance (between the centroids of the monomers), θ is the angle between μ (transition dipole vector) and R , and ϵ is the optical dielectric constant of the medium. Thus for H-aggregates, when $\theta=90^\circ$, the coupling is positive, and is negative in J-aggregates when θ is close to zero. H-aggregates become J-aggregates at the so-called "magic angle" of 54.7° .⁴³

The crude point-dipole, Coulomb interpretation of the coupling is only a valid approximation for homodimers with large intermolecular separation.⁵² When monomers stack in close proximity ($R \leq 4\text{\AA}$), wavefunction overlap invokes the possibility of charge-transfer (CT) states, where the electron resides on one site and the hole on another.⁵³ This creates a short-range coupling factor as well as the long-range Coulomb coupling. The total coupling is the combined short-range CT coupling and the Coulomb coupling, leading to complex behaviour which is dependent on the sign of the short- and long-range contributions. For example, the CT coupling is highly sensitive to the molecular geometry, where small distortions can change the total coupling value and result in multiple H- to J-aggregate conversions.⁴⁹ Yamagata *et. al* devised a wavefunction overlap scheme to calculate the effect of charge transfer in addition to the Coulomb interpretation.⁵⁴

Perhaps the simplest method to attain J_{ij} is to refer to the original definition of the coupling shown in Figure 2.5 and use the splitting of the first two adiabatic excited states of the supermolecular system,

$$J_{ij} = \frac{E(S_2) - E(S_1)}{2} \quad (2.30)$$

It is a method which has proven popular for its conceptual simplicity and ease of calculation, since only one calculation on the dimer is required.^{38,40,55}

An alternative method based on the Coulomb interpretation is to project the full transition density matrix as atomic transition charges q^t , where each atom in the monomer is assigned a

transition charge. This is cheaper than the full supermolecular calculation since only a monomer need be calculated, although the polarising effect of the second monomer is therefore neglected. In such a scheme, J is calculated through intermolecular pairwise contributions

$$\sum_u^{N_i} \sum_v^{N_j} \frac{q_u^t q_v^t}{|\mathbf{R}_u^i - \mathbf{R}_v^j|} \quad (2.31)$$

between atom u monomer i and atom v on monomer j . This method is capable of reproducing the supermolecular couplings at lower computational costs for well-separated dimers.⁵² Alternatively, the transition densities can be projected onto a three-dimensional real-space grid and integrated to give a molecular transition density, the product of which gives the coupling, in what is known as the transition density cube method.⁵⁶

An attractive method to calculate J_{ij} , incorporating both the Coulomb and short-range interactions, is the diabaticization method devised by Arag3 and Troisi. Here, the adiabatic energies of the supermolecule in the diagonal adiabatic Hamiltonian are transformed to the diabatic, monomer basis, such that the off-diagonal elements of the diabatic Hamiltonian \mathbf{H}^D contain the couplings, computed *via*

$$\mathbf{H}^D = \mathbf{C}\mathbf{H}^A\mathbf{C}^\dagger \quad (2.32)$$

$$\mathbf{H}^D = \begin{bmatrix} E_i^D & J_{ij} \\ J_{ij} & E_j^D \end{bmatrix} = \begin{bmatrix} C_{11} & C_{12} \\ C_{21} & C_{22} \end{bmatrix} \begin{bmatrix} E_i^A & 0 \\ 0 & E_j^A \end{bmatrix} \begin{bmatrix} C_{11} & C_{21} \\ C_{12} & C_{22} \end{bmatrix} \quad (2.33)$$

where \mathbf{H}^A is the diagonal Hamiltonian of the S_1 and S_2 excitation energies and \mathbf{C} is the adiabatic-diabatic transformation matrix. There exists no unique way to transform the bases, and various properties can be used, such as atomic transition charges or transition dipoles. In our work, \mathbf{C} is defined as the matrix which minimised the difference between the transition dipole moments of the first two excited states of the dimer ($\boldsymbol{\mu}^A$) and the transition dipole moments of the first excited state of the two isolated monomers ($\boldsymbol{\mu}^{ISO}$), which are collected by matrix \mathbf{M} . The singular value decomposition method of \mathbf{M} into $U\Sigma V^\dagger$ yields matrix \mathbf{C} ,

$$\begin{aligned} \mathbf{M} &= (\boldsymbol{\mu}^A)^\dagger \boldsymbol{\mu}^{ISO} \\ &= U\Sigma V^\dagger \end{aligned} \quad (2.34)$$

$$\mathbf{C}^\dagger = UV^\dagger \quad (2.35)$$

This method encapsulates both the Coulomb interaction and the short-range effects such as exchange, overlap, and charge-transfer.^{46,49,50} In this thesis, we implement the method of Troisi and evaluate exciton couplings in Chapter 6. In Chapter 7, we explicitly compare the results to the couplings obtained using the supermolecular approach, and extend the method to a trimer basis, where the effect of a third monomer on the coupling is considered.

2.3.5 Modelling Excited States in Molecular Crystals

The localised nature of excited states in molecular crystals lends to a molecular orbital description of their photophenomena, since the excited state resides on typically one or two molecular units.⁵⁷ The low population of excited molecules in the crystal has led to the current practice of modelling clusters of molecules extracted from the crystal structure. In this methodology, the cluster is partitioned into regions which are treated at different levels of theory in “multilayer” models. At the centre of a cluster sits a chromophore molecule (or molecules), to be treated at an appropriate level using quantum mechanical methods. To reduce the computational expense, the contribution of the surrounding environmental molecules to the total energy is calculated a lower level of theory, either through a molecular mechanics (MM) description (denoted QM:MM) or an efficient quantum mechanical method such as Hartree-Fock (HF) (QM:QM’). QM:QM’ approaches combining multireference methods with DFT are a promising extension, although they have not yet been widely used in describing excited state phenomena.^{58–60} It is typical to freeze the positions of the environmental atoms to retain the crystal packing arrangement, such that only the QM atoms are allowed to relax during an optimisation. It is therefore desirable to first optimise the unit cell using plane-wave methods.⁶¹

A popular route to obtaining the total energy of the cluster is the ONIOM method.^{62–64} In the field of AIE, the multilayer ONIOM QM:MM protocol has been applied in many studies to understand the fluorescent behaviour of solid state organic compounds.^{39,65–77} In the ONIOM method, the whole cluster is called the “real” system and the region to be treated at the highest level of theory is labelled as the “model”. The total energy (E_{ONIOM}) for the cluster is calculated through a subtractive scheme,

$$E_{ONIOM} = E_{QM,Model} + E_{MM,real} - E_{MM,model} \quad (2.36)$$

where the total energy is the sum of the QM energy of the model system with the MM energy of the real system. Subtracting the energy of the model system at the MM level ensures that its contribution is not double counted.⁶⁴ The QM level energy is calculated through the chosen method, typically (TD)DFT or CASSCF/CASPT2. In our work, we mainly use the AMBER force field to describe the MM-level atoms, which evaluates the MM energy through⁷⁸

$$E_{MM} = \sum_{bonds} K_r(r - r_{eq})^2 + \sum_{angles} K_\theta(\theta - \theta_{eq})^2 + \sum_{dihedrals} \frac{V_n}{2}[1 + \cos(n\phi - \gamma)] + \sum_{i < j} \left[s_{ij}^{vdW} \left(\frac{A_{ij}}{r_{ij}^{12}} - \frac{B_{ij}}{r_{ij}^6} \right) + s_{ij}^q \frac{q_i q_j}{\epsilon r_{ij}} \right]. \quad (2.37)$$

The first three terms evaluate the bonded interactions through chemical bonds, angles and dihedrals. The final non-bonded interaction term describes the van der Waals and Coulomb interaction between each atom in the system, which are scaled by s^{vdW} and s^q . Also popular is the universal force field (UFF) to obtain the MM energy, which is parameterised without partial charges.⁷⁹ In mechanical embedding, the cross-region electrostatic interactions are treated at the MM level, and as such the electronic Hamiltonian is not polarised (or influenced) by the environmental molecules. In electrostatic embedding, atom-centred point charges from the MM region are incorporated into the QM Hamiltonian $\hat{H}_V^{model,QM}$ by modifying the original Hamiltonian $\hat{H}^{model,QM}$

$$\hat{H}_V^{model,QM} = \hat{H}^{model,QM} - \sum_i \sum_N \frac{s_N q_N}{r_{iN}} + \sum_J \sum_N \frac{Z_J s_N q_N}{r_{JN}} \quad (2.38)$$

where N, J , and i refer to the MM atoms, QM atoms, and electrons respectively.⁸⁰ The scaling factor s_N prevents overpolarisation of the wavefunction from atoms close to the QM region. The final term is also included in the MM evaluation of the model system, to ensure direct cancellation. The electrostatic embedding scheme provides a direct perturbation of the electronic structure by the environment.

Fundamental in the current work is locating conical intersections in the solid state. Studies by Bearpark and co-workers has shown that this is possible in the ONIOM regime.⁸¹ Using previtamin D (precalciferol) as an exemplar, they partition the molecule into real and model systems, where the real system contains the region where the distortion occurs at the conical intersection. They probe the ground and excited state PESs using multireference methods to show that

faithful conical intersection geometries can be optimised within the ONIOM framework compared to the full calculation.

The work of Morrison *et. al.* has also probed how conical intersections can be located using the ONIOM approach, uncovering the photochemical mechanisms in systems undergoing E-SIPT.^{82,83} In a subtractive ONIOM scheme (Equation 2.36, using static and dynamics calculations in a hybrid QM/QM regime, they find that ES IPT is ultrafast (80 fs) in 7-(2-Pyridyl)-indole in the solid state, followed by reaching a conical intersection through intramolecular rotation.⁸² In N-salicylidene-2-chloroaniline, they find competition between the enol and keto relaxation channels, with an equal population of each, where intramolecular rotation again leads to S_1/S_0 crossings.⁸³ This relaxation mechanism is encountered in our work for the **HC** systems.

A potential deficiency arising from a standard ONIOM calculation for a cluster model is the neglect of the periodic nature of the molecular crystal. The truncation of the crystal into a cluster naturally removes the electrostatic long-range potential. To overcome this, other fields have research have applied the Ewald summation technique, which calculates the exact nature of the crystalline electrostatic potential.^{84,85} The Ewald method as implemented by Derenzo and coworkers does this through a five step algorithm:^{86,87}

1. The point charges from a unit cell are assigned to the atoms of a supercell centered around a defect of interest called the quantum cluster.
2. A chosen number of sample sites are randomly sampled in the quantum cluster region.
3. A spherical region is then defined so that the quantum cluster and a number of additional points are included within a chosen radius. The points within that region will maintain their original charge values whereas the remaining points will be allowed to vary.
4. An Ewald potential is calculated at each fixed value point (including points in the quantum cluster) and at the random sites from step 2.
5. A system of linear equations is solved with respect to the variable charge values to match the direct sum of all charges in the system to the Ewald potentials calculated in step 4, whilst driving the overall charge and dipole moment to zero.

The Ewald method was applied to excited states in molecular crystals in 2016 by Wilbraham *et al.*⁶⁹ As the authors point out, the Ewald scheme is superior to traditional point charge embedding

which inevitably involves some kind of charge truncation and the subsequent loss of periodicity. The Ewald method in contrast aims to reproduce the exact potential on the chromophore. For their case, an ESIPT/AIE system was chosen as a test molecule, such is the importance of the environment on the electronic structure. A second shortcoming of the ONIOM approach alone for excited states is the lack of polarisation of the MM region from the QM region. In the electrostatic embedding scheme, the QM region is polarised by the MM environment, but there is no mutual polarisation from the QM region *back* to the MM atoms. Wilbraham and co-workers have attempted to remedy this through a self-consistent polarisation scheme, where the MM point charges and QM charges are altered until convergence.⁶⁹ This has been shown to be more effective than embedding alone for modelling absorption and emission in molecular crystals.^{73,88} However, by treating the environment point charges and the chromophore charges at the same level of theory, the former necessarily correspond to a fully excited molecular crystal, which is perhaps nonphysical. This has been addressed by Miguel Rivera in our group, who has worked on the development of self-consistent embedding schemes to extend the method of Wilbraham. These are implemented in the `fromage` package, to which I have also contributed modules.^{89,90} Due to the implementation timeline, self-consistent embedding schemes were not included in the work of this thesis.

In this chapter we have introduced the theoretical framework for the thesis. With this established, in Chapter 3 we demonstrate how the discovery of aggregation induced emission (AIE) has revolutionised the development of solids state emitters. Of central importance is excited state intramolecular proton transfer (ESIPT), and we cover the fundamental principles and uses before the eleven exemplar systems covered in the research of Chapters 5-7 are presented.

3 Luminescent Organic Materials

3.1 Aggregation Induced Emission

3.1.1 Overview

In 2001, the Tang group at the Hong Kong University of Science and Technology were interested in silole-based polymers for highly emissive thin-films. As was common at the time, fabrication of such materials was challenging due to ACQ. Through serendipity during a purification process, they found that a wet spot of 1-methyl-1,2,3,4,5-pentaphenylsilole was almost non-emissive, but brightly fluorescent after solvent evaporation.⁹¹ The law of aggregation quenching emission had been turned on its head, and the Tang group had observed the exact opposite behaviour, of molecular aggregation inducing light emission.

The Tang group used the AIE phenomenon to develop a range of chemical sensors to detect volatile organic compounds, explosives, and pH.^{92–94} Such was the magnitude of the AIE breakthrough and the mechanistic interpretations provided by the Tang group, many other groups began to explore this exciting new phenomenon for a wide range of applications. In the field of biological probing, AIE-active systems can detect important small molecules such as glucose, thiols, and lactic acid.^{95–97} Probes have been developed to detect protein fibrillation, which has been linked to Alzheimer's, Parkinson's and type II diabetes.⁹⁸ AIE systems have been also used in medical imaging, where fluorescence is an attractive technique due its high resolution, wide applicability, and low cost.³ The Tang group have tracked the progress of the field with periodic, in-depth reviews of the vast number of innovations, of which they contribute a significant share.^{3,32,33,99–101} The most prominent avenue for the application of AIE is in optoelectronic and lasing devices, particularly OLEDs, which we will overview in Section 3.1.3. Prior to that, in the next section, we examine the proposed mechanisms which precipitated from the experimental studies led by Tang *et. al.*

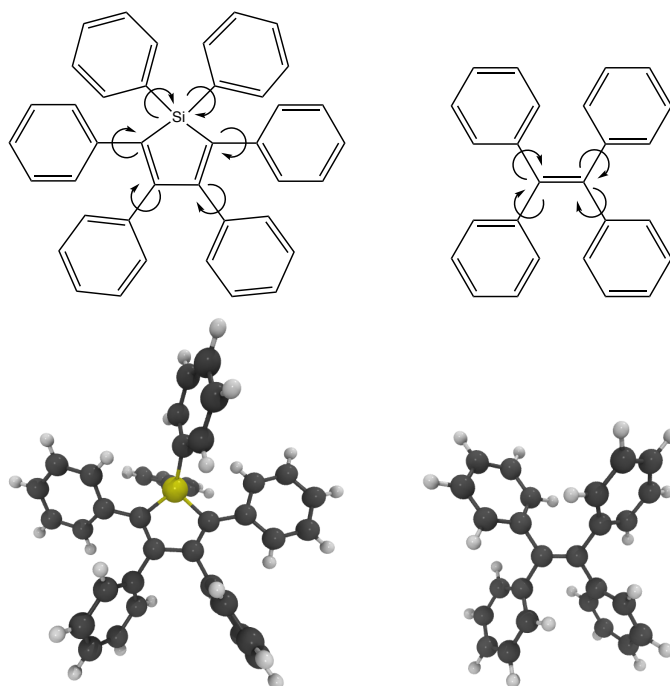


Figure 3.1: Two dimensional (top) and three dimensional (bottom) structures of two of the ubiquitous AIE-active systems, hexaphenylsilole (HPS, left) and tetraphenylethene (TPE, right). AIE occurs through restriction of the rotational motions depicted with arrows.

3.1.2 Hypothesised Mechanisms

Systems exhibiting AIE are typically based on a propeller architecture, where a central stator is connected to a number of aromatic rotors *via* single bonds, as shown in Figure 3.1. In the initial analysis of 1-methyl-1,2,3,4,5-pentaphenylsilole, the absorption spectra showed that after the water fraction in an ethanol-water solvent mixture rose above 60%, the absorption band increased in intensity and moved to longer wavelengths.⁹¹ On this basis, the AIE activity was attributed to the formation of aggregates which forced the molecules into a more planar conformation, thus increasing the conjugation and the absorption. Enough rotation about the sigma bonds was still possible to prevent complete planarity and therefore limiting the stacking and subsequent fluorescence quenching.

A few months later, the group showed the AIE effect for four more silole systems, followed by an extensive study of ten phenylsiloles.^{102,103} Crucially, in this later work the crystal structure of the siloles showed that the conformation remains twisted in the solid state.¹⁰³ Large torsional

angles exist between the phenyl groups and the central silole moiety, on account of the steric repulsion between the six phenyl groups. The lack of space between the phenyl blades, and their angular orientations, prevents intermolecular stacking which give rise to aggregation caused quenching. Therefore the planarisation hypothesis was wrong.

The group investigated other quenching mechanisms, such as twisted intramolecular charge transfer (TICT), where a non-emissive twisted conformer is formed *via* charge separation in the chromophore. The TICT state can be stabilised, and thus favoured, in polar solvents. However, no emission was recorded across a wide range of solvent polarities, ruling out TICT as the cause for AIE in the siloles. Also, the lack of electron donor and acceptor groups make it highly unlikely that TICT could take place in the siloles. In an elegant experiment it was found that the emission increased almost linearly with increasing solvent viscosity, even though no aggregates were formed. In a similar vein, the photoluminescence intensity increased with decreasing temperature, with NMR studies confirming that the intramolecular rotations of the exterior phenyl groups were reduced at lower temperatures. It was concluded that in good solvents, at ambient temperature, the energy consumed by the rotation of the phenyl groups about the single bonds results in the nonradiative decay of the excited state. Upon aggregation, the propeller-like shape limits the intermolecular stacking while C-H $\cdots\pi$ interactions rigidify the structure, hindering the intramolecular rotation and the excited state decays *via* fluorescence.¹⁰³

The restriction of intramolecular rotation (RIR) mechanism allowed the library of AIE-active systems to be expanded to other molecules with propeller-shaped structures. Along with the phenylsiloles, TPE derivatives (Figure 3.1) have driven understanding and technological progress in the field.^{3,32,33,99–101} By switching a phenyl group of TPE with a traditional ACQ molecules, such as triphenylamine or carbazole, the electroluminescence properties of the system are enhanced due to the hole-transport properties of the ACQ group.¹⁰⁴ Conversely, ACQ cores can be made to undergo AIE by the attachment of TPE.¹⁰⁵

Dissipation of the excited state can occur through means other than rotation. A bent, π -surface system of benzenes fused with cyclooctatetraenes undergoes AIE but without any rotatable units.¹⁰⁶ In solution, ring inversions dissipate the excited state and there is almost no emission. Single crystals show emission in the blue region, since the bent structure prevents facial stacking and the inversion modes are restricted. Thus AIE is achieved through restriction of intramolecular vibrations (RIV). In a similar manner, the RIV mechanism can be applied to TPE by locking pairs

of phenyl groups with ethylene linkers. In 2014, Tang unified the RIR and RIV interpretations under the restriction of intramolecular motions (RIM) umbrella.¹⁰⁷

3.1.3 Optoelectronic Applications of AIE

Upon discovery of AIE, the potential for the improvement of optoelectronic devices was immediately apparent. In the original publication, the group built a highly emissive blue-emitting electroluminescent device, and optimised the device to 8% external quantum efficiency (η_{QE}) in the cyan region, a vast improvement on the previous high of just 1.5% for an OLED.^{91,108} η_{QE} is the product of the electroluminescence efficiency of the emitter (the organic layer in this case) and the external coupling factor, which is a measure of the fraction of light able to escape the OLED. Due to electroluminescence efficiency being limited to 25% for singlet emitters, and the external coupling being limited to around 22%, it was previously thought that the theoretical maximum η_{QE} is 5.5%. Indeed, such was the remarkable η_{QE} measure in this OLED that these previously accepted limitations had to be reconsidered.

In follow-up work, a light-blue emitting OLED with hexaphenylsilole (Figure 3.1) as the emitting layer was fabricated with η_{QE} of 7%.¹⁰³ While the unfavourable spin statistics inhibit efficiency for singlet-emitting OLEDs across the visible spectrum, deep blue emitters are harder still since the large band gap makes charge injection difficult, hindering the development of full colour displays. Non-doped deep blue OLEDs with η_{QE} of around 4% were reached in 2014, with emitters based on triphenylamine and tetraphenylethene (Figure 3.1).^{109,110} This has recently been increased to 6.5% using a carbazole-based organic layer, and in 2018 reached 9.4%.^{111,112} Inclusion of phosphorescent or thermally-activated delayed fluorescent dopants can further increase the quantum efficiency by harvesting triplet states for luminescence.¹¹³

3.2 Mechanistic Interpretations of AIE

3.2.1 Approaches Based on Fermi Golden Rule

In 2005, the first theoretical study to determine the root of AIE in the phenylsiloles was presented.¹¹⁴ To probe the origins of the AIE phenomenon, Shuai *et al.* constructed a model for the

observed Φ_{PL} ,

$$\Phi_{\text{PL}} = \frac{k_r}{k_r + k_{nr}} \quad (3.1)$$

where the overall observed Φ_{PL} is determined by the rates of radiative (k_r) and nonradiative (k_{nr}) decay. k_{nr} will typically consist of internal conversion, intersystem crossing, and intermolecular processes such as charge transfer. The idea is to calculate the radiative and nonradiative rates in solution and aggregate form to elucidate the reason for the increased fluorescence in the solid state. This strategy underpins most of the theoretical investigation into AIE, of which the Shuai group have been at the forefront over the last 10 years.

To evaluate k_r , the Einstein spontaneous emission formula can be applied,¹¹⁴

$$k_r = \frac{f E_{if}^2}{1.499} \quad (3.2)$$

where f_{if} is the oscillator strength and E_{if} is the energy difference between the initial (S_1) and final electronic state (S_0). This considers that there is no displacement between the ground and excited state PESs. An alternative method to evaluate k_r is to simulate the fluorescence spectrum using a Wigner ensemble and integrate the spontaneous emission for the rate,

$$k_r = \frac{1}{\hbar} \int \Gamma_r(E) dE \quad (3.3)$$

where Γ_r is the rate of spontaneous emission per molecule per unit of angular frequency between E/\hbar and $(E + dE)/\hbar$.^{115,116} We compare both strategies in Chapter 7.

The Fermi Golden rule and Condon approximation can be used within the Born-Oppenheimer approximation to determine k_{nr} according to,¹¹⁷

$$k_{nr}(T) = \frac{2\pi}{\hbar} \sum_{\nu_i \nu_f} P_{i\nu_i}(T) \left| \sum_k \langle \Phi_f | \hat{P}_k | \Phi_i \rangle \langle \Theta_{f\nu_f} | \hat{P}_k | \Theta_{i\nu_i} \rangle \right|^2 \delta(E_{i\nu_i} - E_{f\nu_f}) \quad (3.4)$$

where $P_{i\nu_i}$ is the Boltzmann distribution of vibrational states (ν) in the initial electronic state (Φ_i), \hat{P} is the momentum operator to give the coupling between electronic states and nuclear (Θ) wavefunctions. The first sum runs over each of the vibrational states in the initial (ν_i) and final (ν_f) states, and Boltzmann probability for the excited state (ν_i) is multiplied by the product of the electronic (or nonadiabatic) coupling and the vibrational coupling. The coupling terms mea-

sure the change of the nuclear and electronic wavefunctions due to nuclear displacements for each nuclei k . For systems with small spin-orbit coupling, the contributions of intersystem crossing are normally neglected. As such, the framework for evaluating k_{nr} focuses on internal conversion processes, although intermolecular decay through exciton formation or charge transfer are of growing interest.¹¹⁸ Equation 3.4 lies at the heart of Shuai's theoretical framework for interpreting AIE through intramolecular motions, which we denote the Fermi Golden Rule Restriction of Intramolecular Motions (FGR-RIM) approach.

Solving Equation 3.4 is computationally demanding and thus approximations must be made. Initially Shuai *et al.* used a displaced harmonic approximation, where it is assumed that the excited state PES is just a rigid displacement of the ground state.¹¹⁴ The internal conversion rate can then be recast as

$$k_{nr} = \sum_l \frac{1}{\hbar} \left[\frac{\omega_l}{2\hbar} |R_{fi}^l|^2 \right] N_{FC} \quad (3.5)$$

where R_{fi}^l are the nonadiabatic couplings, ω_l is the frequency of mode l and N_{FC} is the density-weighted Franck-Condon factor, given by

$$N_{FC} = \sqrt{\frac{2\pi}{\sum_j S_j \omega_j^2 (2\bar{n}_j + 1)}} \exp \left[-\frac{(\omega_{fi} + \omega_l + \sum_j S_j \omega_j)^2}{2 \sum_j S_j \omega_j^2 (2\bar{n}_j + 1)} \right]. \quad (3.6)$$

k_{nr} the weighted Franck-Condon factors are functions of the Huang-Rhys (HR) factors S for each mode j , which determine the difference in vibrational wavefunctions in different electronic states.

Within the displaced harmonic oscillator model (Equation 3.5), some key approximations are made. Firstly, by assuming the ground and excited state PESs mirror each other means that the model is only valid for systems where the excited state geometry does not deviate far from the ground state equilibrium position. Secondly, in the implementation a "promoting-mode" l is chosen which is used to calculate the nonadiabatic coupling but does not contribute to N_{FC} (Equation 3.6).

To overcome these limitations, Shuai *et al.* further developed the FGR-RIM theory to incorporate the Duschinsky rotation effect (DRE), such that all vibrations are considered rather than just one promoting mode.^{114,115,119} The DRE correlates the excited state coordinates Q^e with those of the ground state Q^g

$$Q_i^e = \sum_j R_{ij} Q_j^g + D_i \quad (3.7)$$

where R_{ij} are the elements of the Duschinsky rotation matrix and D_i is the displacement of the two PES. Fourier transform of the delta function yields the thermal vibrational correlation function which can be solved analytically *via* the implementation of Peng and Shuai.¹²⁰ Incorporating DRE to model the effect of temperature shows that increases k_{nr} by 700 times when the temperature increases from 70K to 300K.¹²¹ Low-frequency modes are strongly coupled for tetraphenylbutadiene compounds, while high-frequency modes are less sensitive to temperature effects and less affected by DRE.

Shuai *et al.* have also considered the effect of including exciton couplings in the nonradiative decay rate.¹¹⁸ The authors developed an analytical expression for k_{nr} incorporating the exciton coupling and evaluated the rates for four aromatic molecules and four typical AIE chromophores. It was found that the exciton coupling increases k_{nr} , but only slightly. However, the values of exciton couplings for the tested systems was less than 30meV, which is relatively small.

The FGR-RIM framework offers major progress in rationalising AIE through the restriction of intramolecular motions interpretation. Shuai's group have implemented the methods in a closed-source, commercial code MOMAP.¹²² However, the formalism contains some key approximations which should be highlighted. For the electronic nonadiabatic coupling, perturbation theory is used where the magnitude of the coupling is only calculated at the equilibrium geometries in S_0 and S_1 . This may be a source of error in systems which deviate from the equilibrium structures, as nonadiabatic couplings can vary significantly in the regions of surface crossings. Further, low-frequency modes driving the photochemistry can be highly anharmonic and nonadiabatic couplings in the equilibrium region do not necessarily correlate with the deactivation modes driving the photochemistry. In general, the use of the harmonic potentials potentially limits the applications to molecules which excited state dynamics is restricted to regions of the PES around equilibrium. These approximations can break down in systems with more highly anharmonic excited state PESs.

3.2.2 Huang-Rhys Factors and Reorganisation Energies

Using the Duschinsky rotation matrix, normal modes can be correlated between different electronic states, yielding the Huang-Rhys factors S between the electronic states for each frequency

ω

$$S_j = \frac{\omega_j D_j^2}{2\hbar} \quad (3.8)$$

where D_j is the displacement of mode j between the equilibrium geometry in the considered electronic states. Summation of each Huang-Rhys factor yields the normal mode reorganisation energy for the system,

$$\lambda_{NM} = \sum_{j=1}^{3N-6} \hbar\omega_j S_j \quad (3.9)$$

which is associated with the energetic cost of geometry relaxation in the electronic transition. Analysis of the Huang-Rhys factors, the reorganisation energies, and the nonadiabatic couplings give insight into the main vibrational modes involved in the internal conversion. In particular, analysis of the HR factors and reorganisation energies are popular for the semi-quantitative interpretation of AIE.^{65,72,77,117,120,121,123-130} Since k_{nr} is a product of the electronic couplings and the Franck-Condon factors, both of these must be small in order to increase Φ_{PL} (Equation 3.1). For the phenylsilole compounds, calculation of k_r and k_{nr} in vacuum revealed that the most significant contributions to k_{nr} come from low-frequency rotational modes, which have large HR factors and large reorganisation energies. The authors hypothesise that in the solid state, the dampening of rotational modes due to steric hindrance reduces the HR factor, and thus the N_{FC} contribution to k_{nr} .^{114,117} k_{nr} decreases with respect to k_r , resulting in fluorescence.

The reorganisation energy can also be calculated in the adiabatic regime,¹³¹

$$\begin{aligned} \lambda_A &= \lambda_{ex} + \lambda_g \\ &= (E_{ex}^* - E_{ex}) + (E_g^* - E_g) \end{aligned} \quad (3.10)$$

where E_g and E_{ex} are ground state energies at the S_0 and S_1 minima, and E_g^* and E_{ex}^* are the corresponding excited state energies at respective minima.¹³² This is visualised in Figure 3.2. λ_A can be easily calculated using quantum chemical methods, where geometry optimisation in S_0 and S_1 , and a single point calculation of S_1 at the S_0 minimum, yields four quantities required to evaluate Equation 3.10. This does not require the normal modes to be calculated, which can be computationally expensive in the excited state for large molecules.

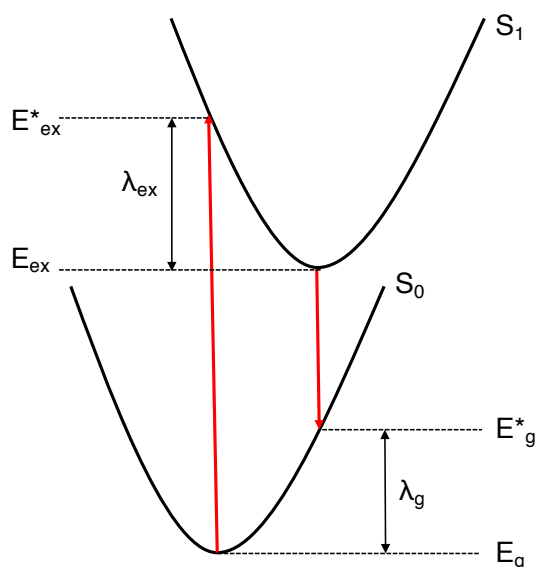


Figure 3.2: Schematic of how the reorganisation energy λ is calculated in the adiabatic regime, based on the ground and excited state PESs of a monomer and the four quantities of Equation 3.10. Red arrows indicate vertical transitions between electronic states. Adapted from reference 133.

3.2.3 Restricted Access to Conical Intersection Model

A different approach to computational modelling of AIE is to consider the topology of the whole PES across the photochemical reaction coordinate. While the framework adopted by Shuai considers the vibronic coupling around the equilibrium geometries, insight into the AIE mechanism can be found by considering the role of conical intersections. Conical intersections are points of degeneracy between electronic states, and allow for nonadiabatic radiationless decay between an upper and lower surface. A more detailed overview on conical intersections is given in Section 2.2. In the restricted access to a conical intersection (RACI) model of Blancafort *et al.*, an energetically accessible conical intersection is responsible for the nonemission in solution. Upon aggregation, steric constraints result in the conical intersection being too high in energy to be populated, leading to fluorescence.⁷¹ The RACI is advantageous in that it does not impose restrictions or assumptions of the topology of the PES.

Blancafort and co-workers first identified the role of a conical intersection for systems based on diphenyldibenzofulvene using multiconfigurational methods.⁶⁶ In solution, torsional rotation takes the system to an extended crossing seam, with the minimal energy conical intersection

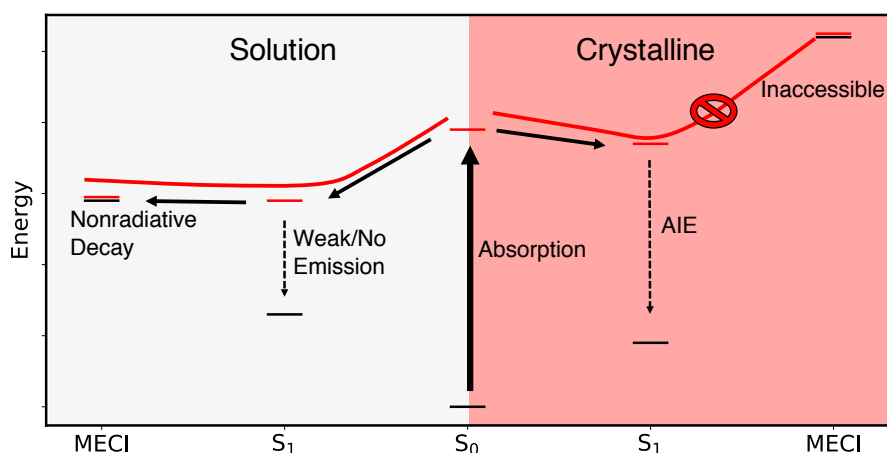


Figure 3.3: Schematic of the RACI model, where in solution there is no emission due to the energetically accessible conical intersection. In crystalline or aggregated state, the minimal energy conical intersection (MECI) is high in energy and inaccessible, which results in AIE.

(MECI) lying 0.7 eV below the excitation energy. In the crystal, rotation is hindered and the MECI lies above the excitation energy. In the RIM model, the phenyl substituents dissipate the excited state energy. In the RACI interpretation, the role of the phenyl substituents is to restrict the torsion in the solid state. Wang *et al.* found a similar mechanism for 4-diethylamino-2-benzylidene malonic acid dimethyl ester.⁷⁰ By combining TDDFT, CASSCF, and CASPT2 methods, the authors compared the PESs in solution and in the solid state. In solution, relaxation along a torsional mode takes the system to a conical intersection which is inaccessible in the crystal. A schematic of the general RACI mechanism is depicted in Figure 3.3.

The RACI model has also been applied to explain the different emissive responses of dicyano-distyrylbenzene derivatives with differing CN substitution patterns.⁴⁰ For some derivatives, there is emission in both solution and the solid state, whereas others display AIE, due to the energetic accessibility of a CI in solution. In this case, it is the vertical excitation energy which is altered most between the compounds, with a red-shift making the conical intersection inaccessible. Again, the CI is reached through intramolecular rotation.

Studies have shown that modes other than rotation can be followed to access conical intersections. For TPE, dynamics calculations at TDDFT level show that cyclisation through bond formation can lead to nonradiative decay through a CI.¹³⁴ The formation of photocyclisation products was later confirmed by transient absorption spectroscopy, while the methylated deriva-

tive of TPE shows similar behaviour.^{135,136} In Duan's study, it was proposed that nonradiative decay of a TPE derivative in solution could be on account of both the intermolecular motions and the conical intersection.¹²⁹

Blancafort has shown that the RACI model can account for AIE in Tang's original compounds, the phenylsiloles.⁷¹ By combining TDDFT and CASSCF/CASPT2 calculations, it is found that a combination of ring puckering and a flapping mode result in a conical intersection in solution, which is inaccessible in the crystal. Conical intersections accessed through ring puckering have been found for other systems exhibiting AIE.¹³⁷ Notable is the octatrene derivative, where the AIE character has been attributed to the RIV mechanism, as discussed in Section 3.1.2.¹⁰⁶ The ring puckering MECI uncovered by Yuan *et al.* means it falls under both the RIM interpretation and the RACI model.¹³⁸

The RACI model and the FGR-RIM interpretation of AIE are different in their underlying assumptions but are not necessarily conflicting interpretations of the AIE phenomenon. The FGR-RIM approach determines the nonradiative decay rate from the coupling of electronic and nuclear wavefunctions through nuclear vibrations. The nuclear modes are treated within the harmonic approximation while the electronic coupling is calculated at the equilibrium geometries. This can be troublesome for systems which undergo large nuclear deformation in the excited state, where the modes can become highly anharmonic and the electronic coupling can vary in the vicinity of a conical intersection. In these cases, more accurate lifetimes would be predicted using nonadiabatic dynamics simulations and the RACI model can be used to interpret the intersection seam. However, the RACI model does require a reliable way to treat all parts of the PES, which is not trivial. In particular, accurate excitation energies and conical intersections are required in order to determine the feasible relaxation pathways. For FGR-RIM, in the solid state the close packing of molecules reduces the conformational phase space and thus the harmonic approximation is more applicable. The RACI model can identify the decay path in solution and the solid state, whilst FGR-RIM can provide a quantitative prediction of lifetimes and Φ_{PL} .

The discovery, development, and rationalisation of the AIE phenomenon has transformed the field of luminescent organic materials. While much of the innovation has been based on the propeller systems, a class of systems based on ESIPT have attracted interest in recent years for their favourable photochemical properties. ESIPT systems form the basis of the research in this thesis and in the next section the ESIPT mechanism shall be introduced, along with the key

applications which incorporate ESIPT.

3.3 Excited State Intramolecular Proton Transfer

3.3.1 Combining AIE with ESIPT

Tautomerism is a type of isomerism resulting in the transfer of a chemical group between two sites on a molecule, and the simultaneous switching of a single and double bond. Photo-induced tautomerism, where the transferring group is a proton, is called excited state intramolecular proton transfer (ESIPT). Research into the mechanism and potential applications of ESIPT has been active for more than half a century, since ESIPT was first observed in the 1950s in salicylic acid.¹³⁹ Photochromic materials harnessing ESIPT have garnered much attention due to the wide range of applications and remarkable properties. In particular, it is the unusually large Stokes-shifted emission which makes ESIPT so attractive. The separation between the absorption and emission bands can typically exceed 200 nm, reducing self-absorption (absorption by other parts of the crystal) and increasing the output signal for the desired application. The emission colour can be tuned by the addition of electron donating or withdrawing groups, as well as solvent polarity and viscosity.^{140,141} Dual emission from the pre- and post-ESIPT forms is also possible. These characteristics, in tandem with AIE, have resulted in ESIPT chromophores being used for chemical sensing, biological imaging and probing, as well the optoelectronic applications such as optical memory, lasers, and OLEDs.^{4,142-146} However, while there is a huge potential range of applications for ESIPT emitters, there are notable shortcomings, such as low Φ_{PL} and short fluorescent lifetimes.⁴

3.3.2 The Four-Level Photocycle

Inherent in all ESIPT processes is a fully reversible four-level photocycle, the prerequisite for which is the presence of an intramolecular hydrogen bond. The proton donor can be an amino or hydroxyl group, while the proton acceptor is usually an imine or carbonyl. The four-level photocycle for salicylic acid is depicted in Figure 3.4, along with the frontier molecular orbitals. The chromophore in the ground state (S_0) is in the enol form (E), mediating hydrogen bond formation between the carbonyl oxygen and the hydroxyl proton. Upon electronic excitation to S_1 (E^*), the

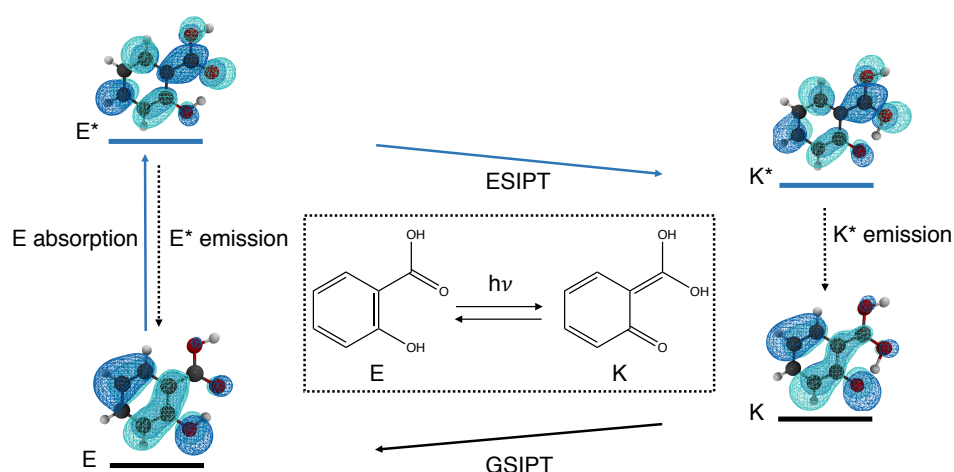


Figure 3.4: The four-level photocycle of ESIPT for salicylic acid. The HOMO and LUMO orbitals are also shown.

electronic redistribution acidifies the hydroxyl and increases the basicity of the carbonyl group, as a result of the population of the π^* orbital on the carbonyl oxygen. In the excited state, the keto form (K^*) is more stable due to the redistributed electron density, and the proton migrates from the hydroxyl oxygen to the carbonyl oxygen. Depending on the system, fluorescence can occur from both the excited enol form (E^*) and the excited keto form (K^*), although due to the ultrafast nature of the proton transfer the major emitting species is the keto tautomer.¹⁴⁴

For most ESIPT processes containing strong hydrogen bonds, proton transfer is near barrierless and occurs on a femtosecond time scale.⁴ The rate of the proton transfer and emission wavelength are highly sensitive to the surrounding medium and the presence of electron donor/acceptor moieties.^{145,147,148} After fluorescence, the ground state keto form (K) is populated and the four level photocycle ($E \rightarrow E^* \rightarrow K^* \rightarrow K$) is completed. The initial geometry is restored through ground state intramolecular proton transfer (GSIPT), although other photoproducts can be formed, for instance through cis-trans isomerisation or intersystem crossing.¹⁴⁹

AIE in ESIPT chromophores can be more complex than in non-polar propeller systems. The presence of hydrogen bonding sites enables the formation of intermolecular hydrogen bonds with solvent molecules, weakening the intramolecular bond and hindering ESIPT.¹⁵⁰ Kasha showed that the ratio of fluorescence intensity between E^* and K^* dramatically changes based upon the solvent polarity.¹⁵¹ In 3-hydroxyflavanone, the K^* fluorescence band is suppressed and the E^* band increases in intensity with polar solvents. In strongly basic solvents, intermolecular proton trans-

fer can occur between the chromophore and solvent, blocking access to the K^* state¹⁵². As touched upon earlier, the presence of donor acceptor groups opens the possibility of deactivation through twisted intramolecular charge transfer (TICT). In solvent, the TICT state is populated after proton transfer and leads to nonradiative decay. In a similar vein to RIR, aggregation frustrates the torsional mode, preventing the TICT state from forming, and opens the radiative decay channel.^{153,154}

The four-level photocycle in ESIPT results in large deviations in the excited state electronic structure, accompanied by large nuclear distortions in solution. As such the application of the FGR-RIM interpretation can be potentially problematic. The RACI model can be applied to alleviate these difficulties, and many ESIPT systems are known to decay through an accessible MECI in solution.^{146,153,155–163} In this work, AIE in the ESIPT systems is interpreted mainly through RACI model, with due consideration of the FGR-RIM approach in Chapter 7.

3.3.3 Exploiting ESIPT and AIE for Applications

The most investigated class of ESIPT molecules are based on benzothiazole dyes, particularly 2-(2-hydroxyphenyl)benzothiazole (HBT).^{4,143} The groups of Li and Liu investigated the effect of solvent for a range of HBT derivatives, finding that increasing polarity impedes the proton transfer reaction and diminishes fluorescence. This is compounded by highly polar, protic solvents, where the hydroxyl proton can dissociate to form the phenolic anion. The proton transfer is highly sensitive to the solvent polarity, which is highly useful for sensing and probing applications.^{150,164} A HBT analogue has been developed for ratiometric probing for hydrogen peroxide in living cells, where the ESIPT-active fluorophore is produced by oxidative hydrolysis.¹⁶⁵ HBT-based systems are also applicable for pH sensing, ion detection, biophotol probing, and intracellular imaging.^{166,166,167}

Substitution of electron donor and acceptor groups onto ESIPT cores can alter the proton transfer rate and stability of the enol and keto conformers on the excited state potential energy surface. In an extensive theoretical study, Jacquemin and co-workers investigated how different substitution patterns affect the emission from enol and keto states for a range of benzothiazoles.¹⁴⁰ They found that dual emission from both E^* and K^* is only possible in a small energy window for the compounds tested, and that the K^* minimum can be favoured more drastically by dependent on the heteroatom in the core. The strongest substituent effects are seen with electron donor

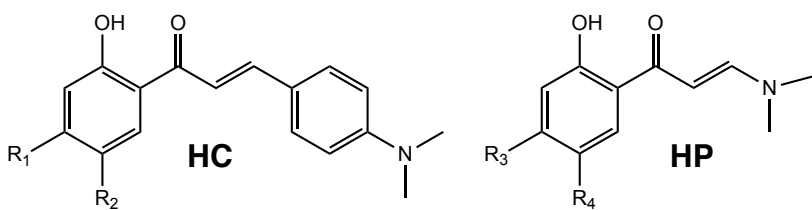
groups, such as methoxy, which stabilise the E* state. The K* state can be favoured by electron withdrawing groups in particular positions. Crucially, the effects of combining substituent groups are complex and depend on the specific ESIPT core and substituent combination. The easily perturbed electronic structure of these systems make design from first principles extremely challenging.

ESIPT cores are excellent candidates for optoelectronic applications on account of minimised self-absorption. However, the environment sensitivity which makes them so suitable for probing can be harmful to device stability.¹⁴³ Through chemical modifications, the Park group have fabricated stable OLED devices with a range of emission frequencies.^{158,168,169} Introduction of carbazole gave access to blue K* emission, while η_{QE} values of 14% have been reached by incorporating triplet harvesting via thermally activated delayed fluorescence with ESIPT.^{168,170} Emission from both E* and K* enables white-light emission in devices, a highly attractive property due to the rarity of single molecule fluorophores with wide emission bands.^{171–174}

The population inversion afforded by the K* form makes ESIPT systems attractive for laser applications.^{175,176} Additionally the large Stokes shift limits reabsorption and increases the optical gain.¹⁴³ In the 1980s, the principle of using ESIPT for lasing applications was established by Kasha and co-workers for 3-hydroxyflavone, where the ultrafast proton transfer and double-well excited state potential energy surface lead to efficient population inversion.^{177,178} Since then, the structural diversity of ESIPT systems have produced lasers with emission in the green, orange, and cyan regions.^{168,179–181} Recently, an imidazole-based system with amplified spontaneous emission properties was developed with deep blue emission.¹⁵³ The restriction of the TICT state in the crystalline form results in Φ_{PL} of 67%, producing an intense and narrow blue band for emission.

3.3.4 Harnessing ESIPT for Near-IR Emission

Developing efficient fluorophore emission at the extremes of the visible spectrum is notoriously difficult. Whilst much attention has been paid to the blue region, the red and near-infrared (NIR) region is also hugely challenging in the solid state. The first system to exhibit solid state lasing properties in the NIR region was reported in 2015.¹⁸² The compounds were based on HC skeletons and displayed ESIPT. Interestingly, solid state fluorescence is only witnessed in some analogues, with substituent position and crystal packing modes determining the Φ_{PL} . The question of whether electronic effects or the crystal structure determined the fluorescence activity

Table 3.1: Molecular structures of the **HC** and **HP** systems and their Φ_{PL} in the solid state.^{182–184}


	R ₁	R ₂	Φ_{PL}		R ₃	R ₄	Φ_{PL}
HC1	H	H	0.32	HP1	H	H	0.74
HC2	CH ₃	H	0.25	HP2	F	H	0.84
HC3	OCH ₃	CH ₃	0.26	HP3	H	OCH ₃	0.77
HC4	H	CH ₃	<0.01	HP4	H	F	0.72
HC5	H	OCH ₃	<0.01				
HC6	F	H	0.41				
HC7	H	F	0.10				

was not fully resolved. Fluorine-containing derivatives with laser properties were published soon after.¹⁸³ In the same year, the same group published another breakthrough in solid state lasing, with structures based on **HP**.¹⁸⁴ These compounds are similar to the **HCs**, but contain only one aromatic ring. Solid state fluorescence in single-benzene emitters is a rarity due to low melting points, but these systems showed extremely high fluorescence activity, surpassing the parent **HC** systems, as shown in Table 3.1.

For the **HC** and **HP** families, the crystal packing, absorption and emission wavelength, and crucially Φ_{PL} , all depend on the choice of substituent and number of aromatic rings. How these factors interplay is not well resolved. To fully understand the photophysical properties of these systems, intricate knowledge of the electronic, molecular picture must be combined with the intermolecular interactions of the crystal. Theoretical methods can help elucidate this picture and offer insight into the working mechanisms behind AIE for these ESIPT systems, and how to maximise the Φ_{PL} . This is the primary aim of the work in this thesis, with **HC** and **HP** families used as exemplars. In this thesis, Chapters 5 and 6 shall focus on the **HC** derivatives, with particular attention on **1** and **5**. In Chapter 7, a holistic view of all eleven systems shall be taken as we examine how the crystal structure and packing regime influences emission. Since the **HCs** are the main focus of the thesis, the following section shall focus on their luminescent properties and previous investigations.

3.4 Emitters Based on 2'-hydroxychalcones

3.4.1 Crystalline Emission Properties of HCs

In 2015, Cheng *et al.* synthesised a range of crystalline HC systems with different substitution patterns.¹⁸² They found the identity and the position of the substituent to be critical in the Φ_{PL} of the crystals. This is summarised in Figure 3.5. When substituents are *meta* to the hydroxyl group (compounds **1-3**) in the phenol ring, deep red fluorescence is observed, but only when in crystalline form. The solutions are almost non-emissive. Interestingly, under frozen conditions the solutions still only weakly fluoresce, indicating that restriction of intramolecular rotation is not the key factor in the AIE for these molecules. When the same substituents are in *para* position (compounds **4,5**), neither the crystals nor the solutions are emissive.

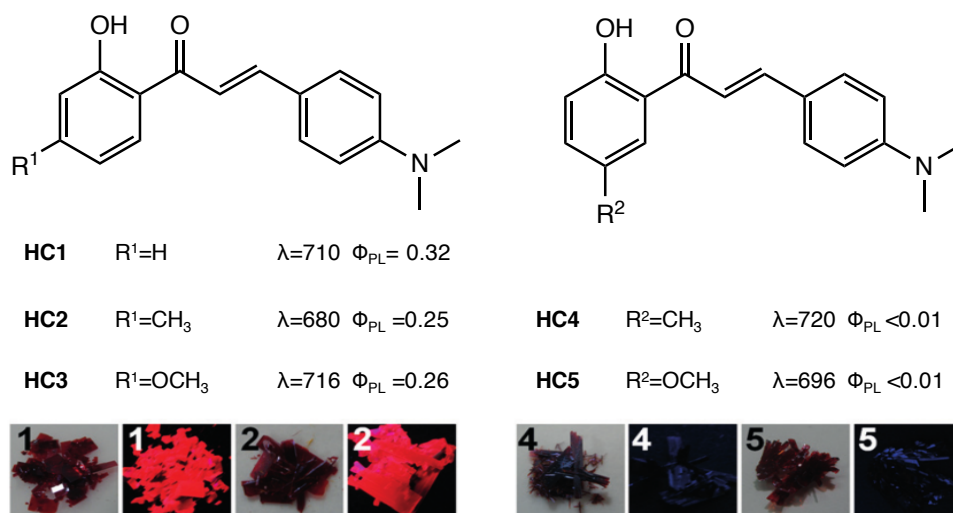


Figure 3.5: Compounds **1-5** synthesised by Cheng and coworkers. **1-** show high Φ_{PL} , but **4&5** are almost non-emissive. Absorbance maxima (λ) and quantum efficiency of photoluminescence (Φ_{PL}) are given, along with pictures of the dark and bright crystals for **1,2,4**, and **5**. Figure adapted from ref. 182 with permission of Wiley-VCH.

These puzzling characteristics are attributed to both the planarity of the individual molecules and the packing in the crystal, as shown in Figure 3.6. Molecules **1-3** are almost completely planar and the strong intramolecular H-bonds, of length 1.753-1.780 Å, increase the rigidity and planarity of the system. In the crystal, the molecules adopt an edge-to-face, herringbone packing mode preventing intermolecular π -interactions between the aromatic rings and enabling fluores-

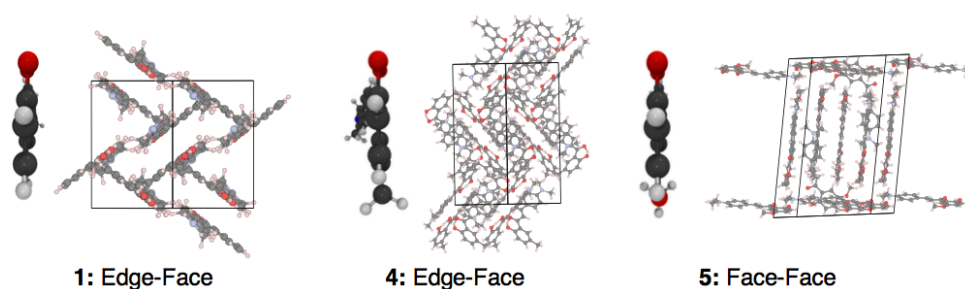


Figure 3.6: The conformation of monomers **1**, **4**, and **5**, along with their crystal structure. Crystal structures obtained from CCDC database codes from ref. 182.

cence from the keto S_1 state. For compound **4**, where a methyl substituent is *para* to the hydroxyl, a similar edge-to-face packing mode is present. However, the molecule has a larger dihedral angle than **1-3**, which the authors attribute as the reason for the weak fluorescence. For **5**, the molecule is planar but the packing is face-to-face with aromatic stacking interactions. In the discussion, it is asserted that **5** is therefore non-emissive in the solid state due to excimer formation and non-radiative decay. The authors also hypothesise that the edge-face packed crystal of compound **4** shows minimal fluorescence because the molecule is not planar, despite other edge-face packed molecules brightly fluorescing, while the planar molecule does not emit because it is packed cofacially. It is with these hypotheses that this thesis begins. The first fundamental question is why do none of the five compounds fluoresce in good solvent? Secondly, in the solid state, why do only compounds **1-3** exhibit AIE? Is this a substituent effect, as a result of the position of the methyl and methoxy groups, or is it due to the molecular packing mode, or is it a combination of both? Quantum chemical methods can identify the nonradiative decay channels in both dispersed and aggregated states, and therefore can elucidate the discrete electronic and intermolecular factors. In answering these questions, we can build understanding of how structure-property relationships operate in the AIE/ESIPT space and provide strategies for further optimising the fluorescence quantum yield of such systems.

3.4.2 Further Investigation into HC Photochemistry

Research into HCs, and chalcones in general, has traditionally focused on their metabolite character, since they are *in vivo* precursors for a variety of flavones, flavonols, isoflavones, anthocyanidins, and other synthetic antioxidants.¹⁸⁵ The ESIPT process in HC was first proven by Chou *et*

al. in 1992.¹⁸⁶ With an absorption band at 354 nm, and emission at 635 nm, the authors concluded that tautomerisation occurs upon absorption and that the keto S_1 state was responsible for emission. Cis-trans isomerism about the central double bond followed by molecular oxygen incorporation produces the flavanoid studied by Kasha, 3-hydroxyflavone. Previous studies had investigated this cyclisation mechanism, where it was initially thought cyclisation occurred through cis-trans isomerisation without proton transfer.^{187,188} It was later found that this isomerism could be hindered by solvent viscosity.¹⁸⁹ Later, Arai and coworkers investigated the photochemistry of **HC** analogues, where they denoted the tautomerisation to be hydrogen atom transfer, rather than proton transfer.¹⁹⁰⁻¹⁹⁶ They mapped the potential energy surfaces using spectroscopic techniques to find that the cis-trans isomerism takes place in the triplet state, and only after hydrogen atom transfer. Most pertinent was their study of the effect of substituent on fluorescence in 2009.¹⁹⁶ Studying systems solvated in benzene, they discovered that the addition of a methoxy substituent *meta* to the hydroxyl group in the phenol ring increased the quantum yield of red fluorescence by at least ten times, which the authors attribute to a combination of electronic and steric effects. The methoxy group stabilises the S_1 state through electron donation to the carbonyl $\pi\pi^*$ orbital whilst its size hinders the intramolecular modes. They supplemented this work by studying a range of **HC** analogues with naphthol, pyrrole and indole substitutions.¹⁹⁷

Since the discovery of the crystalline near-IR fluorescence by Cheng *et. al* in 2015, and over the course of this project, more studies have emerged investigating photochemistry of **HCs**. In early 2017, Li and coworkers synthesised three analogous of **HC1** with differing substitution at the nitrogen and phenol oxygen.¹⁹⁸ The AIE behaviour is attributed to restricting the access to the nonfluorescent TICT state in the aggregate. Two of the systems display excellent quantum yields (0.27, 0.49) and long fluorescence lifetimes in the excited state. Time resolved spectroscopy suggests two decay paths in solid state, but the mechanisms are not identified by the authors. The near-IR technology was used to develop a probe for cysteine, as was done previously by the Tang group using a **HC** system.¹⁹⁹

The AIE/ESIPT principle was applied using **HC** to develop a technique to detect latent fingerprints, for example in crime scenes.²⁰⁰ A fingerprint contains a high level of sebum, and when this is rinsed in a **HC** solution, the **HC** molecules preferentially adhere to the fatty acid residues in the fingerprint, where they aggregate. When light is shone on the fingerprint, ESIPT occurs and red fluorescence is produced, lighting up the fingerprint region against the dark backdrop of

the substrate.

In late 2017, the tunable lasing properties of **HCs** was further attested.²⁰¹ With a fluoro substituted **HC** (**HC6**), colour-tuned organic lasers were developed. It was shown that addition of a second hydroxyl group, β to the carbonyl group on the aliphatic bridge, enables tuning of the photodecay. In solution, both systems undergo ESIPT and have dual emission characteristics in cyclohexane, but no ESIPT is witnessed in isopropanol, due to the formation of intermolecular hydrogen bonds. In the solid state, the compound with additional hydroxyl group does not undergo ESIPT and has blue-shifted fluorescence with respect to the parent **HC6**. The crystal structure shows that the close packing enables intermolecular hydrogen bonds, just like in isopropanol, and ESIPT is inhibited. As such, the additional hydroxyl group produces only E^* emission at 538 nm, and the unmodified system shows solely K^* emission at 647m.

More fundamental spectroscopic studies have also been presented recently. Using time-resolved absorption and emission, Zahid *et. al* study the dynamics of the ESIPT process in **HC1** in both solution and the solid state.²⁰² In methanol, the E^* state is formed and immediately decays, with only trace amounts of the K^* tautomer detected, perhaps on account of solvent molecules forming intermolecular hydrogen bonds and disrupting ESIPT. In the crystal, during the decay of the E^* peak, a new fluorescence peak forms at 600-750 nm which can be ascribed to the K^* state after ESIPT. The E^* form is more transient in the crystal, with its lifetime reduced by a factor of 10 to 3.1 ps, on account of the sterically-enforced planarity enabling efficient ESIPT. Enol emission will also result in self-absorption in **HC1**.

Song and co-workers studied the deactivation of **HC** as a function of solvent polarity using time-resolved absorption spectroscopy.²⁰³ Increasing the solvent polarity stabilises the planar E^* tautomer, due to the intramolecular charge transfer nature of the excitation. The planar E^* state then promotes ESIPT. The authors find no evidence for triplet states in the three solvents. In the nonpolar solvent (cyclohexane), enol decay through intramolecular rotation will compete with ESIPT. For a set of analogues based on **HC3**, but with removal of dimethylamine group, Serdiuk *et. al* found that ESIPT is more efficient than for the parent **HC** compounds, and attribute radiative decay in the solid state to the RACI model.²⁰⁴

The **HCs** and **HPs** systems provide a library of related compounds with differing photobehaviours. In Chapters 5-7, we shall investigate these in detail and establish design rules to optimise the fluorescence response of ESIPT systems. However, next we shall overview the quantum

chemical methods which will be used to explore the properties of these systems.

4 Computational Chemistry Methods

4.1 The Hartree-Fock Method

The Hartree-Fock (HF) method is the foundation of quantum chemistry. In the HF method, a single electron in an N -electron system moves within the field produced by the nuclei and the other $N-1$ electrons.²⁰⁵ The intractable N -electron wavefunction Φ is simplified to be a product of N , one-electron wavefunctions χ ,

$$|\Phi\rangle = |\chi_a\chi_b\dots\chi_i\dots\chi_N\rangle. \quad (4.1)$$

where χ are spin orbitals of each electron in the system. The spin orbitals consist of a spatial functional and a spin function, an infinite number of which could provide an exact solution. However, in practical terms a basis set of atomic functions is supplied, as described in Section 4.3.1.⁸

From the Pauli exclusion principle, no two electrons may share exactly the same four quantum numbers (i.e occupy the same spatial and spin orbital). Since electrons are fermions, the electronic wavefunction is *antisymmetric*, meaning that a change in the orbital must result in the wavefunction changing sign. This is enforced using Slater Determinants.²⁰⁶ This is most easily seen for a two-electron system for electrons at positions \mathbf{x}_1 and \mathbf{x}_2 , where orbital χ_a contains electron at \mathbf{x}_1 and orbital χ_b contains electron at \mathbf{x}_2 , with a normalisation factor of $N^{-\frac{1}{2}}$

$$\begin{aligned} \Phi(\mathbf{x}_1, \mathbf{x}_2) &= \frac{1}{\sqrt{2}} \{ \chi_a(\mathbf{x}_1)\chi_b(\mathbf{x}_2) - \chi_a(\mathbf{x}_2)\chi_b(\mathbf{x}_1) \} \\ &= \frac{1}{\sqrt{2}} \begin{vmatrix} \chi_a(\mathbf{x}_1) & \chi_b(\mathbf{x}_1) \\ \chi_a(\mathbf{x}_2) & \chi_b(\mathbf{x}_2) \end{vmatrix} \end{aligned} \quad (4.2)$$

where by taking the determinant, the antisymmetry is ensured since exchanging the electrons changes the sign of the determinant. In the determinant, the rows consist of the electrons while the columns contain the orbitals. In the HF method, the wavefunction is approximated by a single Slater Determinant, and therefore HF is known as a single-determinant, or single-reference,

method. As well as ensuring antisymmetry, the Slater determinant wavefunction also introduces exact exchange (or HF exchange), a quantum mechanical property for electrons of parallel spin.⁸

The variational principle states that the energy of the true ground state wavefunction will always be less than or equal to the energy a trial wavefunction, meaning that the guessed spin orbitals will never undershoot the true energy.⁸ As such, HF is a purely iterative method where the energy is computed for a set of trial spin orbitals, the spin orbitals are altered, and the energy is calculated again. This is repeated until convergence.

To calculate the “best” set of orbitals, the interactions in the electronic Hamiltonian are split into one-electron and two electron terms. The one electron terms are collected by the core Hamiltonian operator \hat{h}_i , involving the kinetic energy of the electrons and the electron-nuclei interactions,

$$\hat{h}_i = -\frac{1}{2}\nabla_i^2 - \sum_{A=1}^M \frac{Z_A}{r_{iA}}. \quad (4.3)$$

The antisymmetric nature of the Slater determinant results in two operators for the electron-electron interaction, a Coulomb operator \hat{J}_{ij} and an exchange operator K_{ij} , which act on orbital χ_i to determine the effect of the remaining orbitals,⁸

$$\hat{J}_{ij}\chi_i = \chi_i \int \frac{\chi_j^*\chi_j}{r_{ij}} d\mathbf{x}_2 \quad (4.4)$$

$$\hat{K}_{ij}\chi_i = \chi_j \int \frac{\chi_j^*\chi_i}{r_{ij}} d\mathbf{x}_2. \quad (4.5)$$

The Coulomb operator determines the Coulomb potential felt by electron i in orbital χ_i from electron j in orbital χ_j . This is done by *averaging* the interaction over all of the spatial coordinates of electron j . As such, J_{ij} represents the average, or *mean-field*, local potential felt by electron i . For this reason, the HF method is often called a mean-field approach. The exchange operator K_{ij} is a result of the antisymmetric Slater determinant, and is a quantum mechanical artefact of how electrons are by nature indistinguishable, and the exact labelling (i,j) has no physical meaning.⁸

The one-electron and two electron operators are collected by the Fock operator \hat{F} , such that

$$\hat{F} = \hat{h}_i + \sum_{j \neq i}^{\frac{N}{2}} [\hat{J}_{ij} - \hat{K}_{ij}] \quad (4.6)$$

The two electron terms run over only half of the electrons ($\frac{N}{2}$) to ensure interactions are not double counted, while the condition of $j \neq i$ means that an electron cannot interact with itself.

The Fock operator allows Equation 2.2 to be solved in the HF method through,

$$\hat{F}|\Phi\rangle = E|\Phi\rangle \quad (4.7)$$

an eigenvalue equation solved by altering the orbitals until energy convergence is reached. In practice, for a closed shell system, the molecular orbital χ_i consists of a linear combination of K atomic basis functions,

$$\chi_i = \sum_{\mu=1}^K C_{\mu i} \phi_{\mu} \quad i = 1, 2, \dots, K \quad (4.8)$$

The Roothaan-Hall equations are then used to solve Equation 4.7 in matrix form,^{207,208}

$$FC = SC\epsilon \quad (4.9)$$

where F is the Fock matrix containing the elements from the Fock operator, C contains the expansion coefficients from Equation 4.8 and S is the overlap matrix containing the overlaps of atomic orbitals ($\langle\phi_i|\phi_j\rangle$). By diagonalising the Fock matrix, ϵ is a diagonal matrix containing the orbital energies. HF is commonly named the self-consistent field (SCF) approximation, since the Roothaan equations are solved until self-consistency is reached.⁸

The HF method is a powerful approach to solving the electronic part of the Schrödinger equation. However, it has several severe drawbacks which hinder its application and have led to the development of more sophisticated methods to address the shortcomings within. The most serious of these for ground state, closed-shell systems is the correlation problem. While electrons of parallel spin have the required exchange correlation, the Coulomb correlation is completely neglected since each electron sees only an average field of the other electrons. In reality, the motion of one electron is dependent on the motion of each of the other electrons, as depicted in Figure 4.1. This results in the energy of the system in HF being overestimated in respect to the true energy. A number of methods to overcome the lack of correlation have been developed, which use the HF method as a starting point before calculating the electron correlation. Those most relevant to the work in this thesis are discussed in the next section.

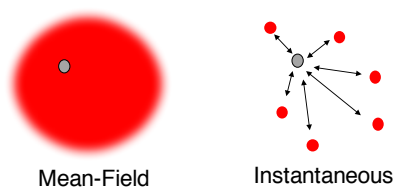


Figure 4.1: Depiction of the mean field electron interaction, where the electron of interest interacts with an average potential, rather than individually with each other electron.

4.2 Recovering Electron Correlation

A number of methods exist to recover the correlation energy absent from the HF method. The correlation energy can be split into two contributions, *dynamic* and *static*. Dynamic correlation is that which is intuitively missing from the HF approximation, where the motion of one electron is correlated with each and every other electron. These are generally termed *post Hartree-Fock* methods, as they use the HF wavefunction as a starting point before subsequently adding the dynamic correlation energy. The lack of static correlation, on the other hand, arises from the single-determinant description of the wavefunction. In some cases, where there are near-degenerate frontier orbitals, two (or more) closed-shell Slater determinants can have very similar energies.⁵ As such, the HF wavefunction can be improved by including these other determinants in the ground state wavefunction. It is these *multiconfigurational*, or *multireference*, methods which recover static correlation. In this section, we shall overview Møller-Plesset perturbation theory to second order (MP2) and coupled cluster (CC) methods, which recover dynamic correlation, and multireference methods, which recovers static correlation. First, however, we shall briefly overview the configuration interaction, which is an important first step in the conceptual understanding of adding dynamic correlation to the HF wavefunction.

4.2.1 Configuration Interaction

The basic idea of the configuration interaction is to describe the wavefunction as a linear combination of Slater determinants. The energy is found by diagonalising the N -electron Hamiltonian (Equation 2.4) in the basis of trial determinant functions, and minimise the energy again using the Variational Principle.⁸ The additional functions consist of “excited” Slater determinants, where a spin orbital (χ_a) in the closed-shell HF determinant is replaced by one of the remaining, unoccu-

pied orbitals χ_r . This excited Slater determinant can be denoted $|\Phi_a^r\rangle$.⁸ Substituting one orbital is a single excitation, whilst replacing two orbitals χ_a and χ_b by χ_r and χ_s is a double excitation, and so on up to N -tuple excited determinants, giving the configuration interaction wavefunction the following form:⁸

$$\begin{aligned}
 |\Phi_{\text{CI}}\rangle = & c_0 |\Phi_{\text{HF}}\rangle + \left(\frac{1}{1!}\right)^2 \sum_{ar} c_a^r |\Phi_a^r\rangle + \left(\frac{1}{2!}\right)^2 \sum_{abrs} c_{ab}^{rs} |\Phi_{ab}^{rs}\rangle \\
 & + \left(\frac{1}{3!}\right)^2 \sum_{abcrst} c_{abc}^{rst} |\Phi_{abc}^{rst}\rangle + \left(\frac{1}{4!}\right)^2 \sum_{abcdrstu} c_{abcd}^{rstu} |\Phi_{abcd}^{rstu}\rangle + \dots
 \end{aligned}
 \tag{4.10}$$

The factorial terms ensure that each excitation is only counted once. In an infinite basis of spin orbitals, the N excited determinants would recover the exact wavefunction of the system. Configuration interaction calculations require huge computational expense due to the vast number of determinants.

To reduce the size and complexity of the wavefunction, some of the terms of the wavefunction in Equation 4.10 can be eliminated, in what are known as *truncated CI* methods. CI calculations are classified according to the degree of excitations allowed in the wave function. If only one electron has been promoted for each determinant, the method is referred as a configuration interaction single-excitation (CIS) calculation. CIS methods approximate the excited state energies of the molecule. CI singles and CI doubles (CISD) calculations can produce a ground state wavefunction incorporating correlation.

The issue with truncated CI methods are their lack of *size-consistency*. The concept of size-consistency relates to how the description of the wavefunction changes with the size of the molecules being described. For methods to be size-consistent, the energy of two identical, infinitely separated, non-interacting molecules should be twice that of the individual molecules. More concretely, the energy of a many-particle system should be proportional to the sum of its non-interacting subsystems. However, in truncated methods like CISD, this is not guaranteed. For example, in the dimer example, a double excitation on each monomer is not possible, since this would result in a quadruple excitation overall. Therefore these excitations are missing in the full system but would be present in the separate monomer calculation.

4.2.2 Møller-Plesset Perturbation Theory

Electron correlation energy can be added to the HF energy by way of an external perturbative correction. In perturbation theory, the total Hamiltonian is divided into the zeroth-order part \hat{H}_0 , which is the HF Hamiltonian, and a perturbation \hat{V} , such that the eigenvalue equation becomes

$$\hat{H} |\Phi_I\rangle = (\hat{H}_0 + \hat{V}) |\Phi_I\rangle = \epsilon_I |\Phi_I\rangle. \quad (4.11)$$

The eigenvalues and eigenfunctions of \hat{H}_0 are varied so that they become closer to the total Hamiltonian \hat{H} , which would then contain electronic correlation. This is done by the ordering factor λ , such that

$$\hat{H} = \hat{H}_0 + \lambda \hat{V} \quad (4.12)$$

For perturbational theory to be justified, the perturbation λ must be small ($\ll 1$). The true eigenvalues and eigenfunctions are expanded in a Taylor series in λ up to n th order,

$$\epsilon_I = E_I^{(0)} + \lambda E_I^{(1)} + \lambda^2 E_I^{(2)} + \lambda^3 E_I^{(3)} + \dots + \lambda^n E_I^{(n)} \quad (4.13)$$

$$|\Phi_I\rangle = |\Phi_I^{(0)}\rangle + \lambda |\Phi_I^{(1)}\rangle + \lambda^2 |\Phi_I^{(2)}\rangle + \lambda^3 |\Phi_I^{(3)}\rangle + \dots + \lambda^n |\Phi_I^{(n)}\rangle \quad (4.14)$$

After inserting Equations 4.13 and 4.14 into Equation 4.11 and collecting terms by order, the general expression for the total energy is

$$E_I = E_I^{(0)} + \sum_{n=1}^n \langle \Phi_I^{(0)} | \hat{V} | \Phi_I^{(n-1)} \rangle \quad (4.15)$$

The perturbation operator \hat{V} introduces the Coulomb repulsion between electrons, which when combined with excited Slater determinants, recovers the dynamic correlation energy. In most chemical applications, the method is contracted at second-order, and was initially employed by C. Møller and M.S. Plesset to obtain the correlation energy, hence the acronym MP2 is often used.²⁰⁹ Since MP is perturbative, the MP-calculated energy can be lower than the true energy, making it a non-variational method. We use MP2 in Chapter 5 to obtain accurate ground state geometries of the **HC** structures, where their small size make MP2 a computationally affordable option.

4.2.3 Coupled Cluster

In an alternative approach to perturbation theory, CC methods were introduced in the 1960s to account for electron correlation.^{210,211} CC theory uses excited determinants by means of a Taylor expansion with an exponential operator

$$|\Phi_{CC}\rangle = e^{\hat{T}} |\Phi_0\rangle \quad (4.16)$$

where $|\Phi_0\rangle$ is the HF wavefunction and \hat{T} is the cluster operator. The cluster operator produces a sum of excitation operators up to the truncation level n

$$\hat{T} = \hat{T}^{(1)} + \hat{T}^{(2)} + \hat{T}^{(3)} + \dots + \hat{T}^{(n)} \quad (4.17)$$

where n is the excitation number. $\hat{T}^{(1)}$ includes all single excitations and $\hat{T}^{(2)}$ includes all double excitations, *etc.* Substituting 4.17 into 4.16, and truncating at $n = 2$, yields the coupled cluster wavefunction

$$|\Phi_{CC}\rangle = e^{\hat{T}} |\Phi_0\rangle = \left[1 + \hat{T}^{(1)} + \left(\hat{T}^{(2)} + \frac{\hat{T}^{2(1)}}{2} \right) \right] \Phi_0 \quad (4.18)$$

As for perturbation theory, CC theory is usually referred to by the truncation level, for example CCSD refers to coupled cluster with single and double excitations. CCSD scales at N^6 , adding considerable expense to the HF method, which scales at N^4 (where N is the number of basis functions).

4.2.4 Multireference Methods

The methods described so far use HF as a starting point and are thus built on a single-reference wavefunction. For a closed-shell system of an even number of electrons, orbitals are all doubly occupied. However, in many chemical processes, the electronic structure will deviate from this description and the wavefunction will not be dominated by one single electronic configuration, for example in bond dissociation, excited state processes, or when the system contains metallic elements. The methods typically employed to model such scenarios are termed multireference or multiconfigurational methods. Such methods recover static correlation through linear combination of configuration state functions m , which themselves are made up of Slater determinants.

Note that this is a subtle difference to the configuration interaction. In the configuration interaction, the expansion coefficients c are varied but the underlying spin orbitals are those used in the HF computation. In multireference methods, both the spin orbitals themselves are varied as well as the expansion coefficients of the state functions. The multireference wavefunction has the form

$$|\Psi_{\text{MCSCF}}\rangle = \sum_m c_m |m\rangle \quad (4.19)$$

where $|m\rangle$ is the configuration state function containing optimised molecular orbitals and c_m is the expansion coefficient for the state. In multireference methods, the molecular orbitals are divided into subspaces, where the active space contains excitations between spin orbitals. Most common is to use an active space containing occupied and virtual orbitals selected for their relevance for the problem in hand, and to only include excitations from within the m active orbitals for n electrons. This is called the complete active-space (CAS) method, which when used in combination with HF for the remaining core orbitals (outwith the active space), is denoted complete active-space self-consistent field (CASSCF).²¹² Due to the factorial scaling with the number of active orbitals, further space decomposition methods have been introduced through restricted active-space (RAS), where only certain excitations are allowed. Furthermore, using a state-averaging procedure can optimise the configuration state-functions for multiple states, to describe regions of strong electronic mixing. With these methods, the key parameter is often the choice of the active space - which orbitals to include, how many of them, and how many corresponding electrons. This is not a black-box procedure and will vary depending on the system of interest, the phenomena being modelled, and the computational resources available.²¹³ Recently, algorithms for automatic active-space selection procedures have been proposed.^{214,215}

Most of the total correlation can be recovered by combining a multireference wavefunction with perturbation theory, thus recovering both static and dynamic correlation. This can produce accurate ground and excited state properties for chemical systems, although with rather large computational expense.^{216,217} A favoured approach is to combine CASSCF with a second-order perturbation calculation (CASPT2), providing an effective protocol to calculate excited states.²¹⁸ When the reference wavefunction is constructed using the state-averaging procedure for the reference wavefunction, and uses multiple electronic states in what is known as the *multistate* CASPT2 (MS-CASPT2) method to give a highly accurate electronic structure.²¹⁹

4.3 Density Functional Theory

The methods introduced thus far access chemical properties through some approximation of the wavefunction. An alternative approach is to disregard the wavefunction altogether and instead use the electron density to calculate microscopic properties of matter. This replaces the $3N$ (+spin) variables of wavefunction methods by just 3 (+spin) spatial variables, allowing significant speed-up in computation. In 1964, Pierre Hohenberg and Walter Kohn proved a unique 1:1 correspondence exists between the ground state energy and the ground state density, proving that all ground state properties of an N -electron system can be calculated from the ground state electron density ρ .²²⁰ The energy is thus a *functional* (function of a function) of the electron density produced by a wavefunction,

$$E[\rho] = \langle \Psi[\rho] | \hat{T} + \hat{V} | \Psi[\rho] \rangle \quad (4.20)$$

which, like HF, obeys the variational principle.

DFT is a mathematically exact formulation. However, the exact form of the functional relating the density to the energy is unknown. In 1965, Kohn and Sham developed a self-consistent approach to attain an approximation of the energy functional in equations that are “analogous to the conventional Hartree and Hartree-Fock equations, and, although they also include correlation effects, they are no more difficult to solve.”²²¹ In the Kohn-Sham system, a non-interacting system mimics the real interacting electron density. As in HF where one-electron wavefunctions construct the N -electron wavefunction, so do single particle orbitals (Kohn-Sham orbitals ψ) construct the electron density ρ ,²²²

$$\rho = \sum_{j=1}^N |\psi_j|^2. \quad (4.21)$$

The Kohn-Sham expression for the energy functional is written in terms of the kinetic and electrostatic interactions,

$$E[\rho] = T_e[\rho] + E_{n-e}[\rho] + E_{e-e}[\rho]. \quad (4.22)$$

The most straightforward term to evaluate is the nuclear-electron interaction, which can be expressed as an electrostatic potential V_n from the nuclei acting on the electronic density,

$$V_{n-e}[\rho] = \int V_n(\mathbf{r})\rho(\mathbf{r})d\mathbf{r}. \quad (4.23)$$

The electron-electron interaction can be separated into a classical, Coulomb-type expression and the quantum mechanical exchange-correlation (XC) part,²²²

$$E_{e-e}[\rho] = \underbrace{\frac{1}{2} \int \frac{1}{r_{e_1 e_2}} \rho(\mathbf{r}_{e_1}) \rho(\mathbf{r}_{e_2}) d\mathbf{r}_{e_1} d\mathbf{r}_{e_2}}_{\text{Classical}} + \underbrace{E_{e-e}^{XC}[\rho]}_{\text{XC}} \quad (4.24)$$

The kinetic energy of the interacting system is replaced by the kinetic energy of the non-interacting system, with the correction incorporated in to the XC functional. It is the XC functional which contains the crux of the problem in DFT, since the exact form is unknown. It must be approximated. Much of DFT development is focused on developing more accurate functionals to better describe specific chemical problems.

The first approximation to the functional is the local density approximation (LDA). The LDA was originally proposed by Kohn and Sham in 1965 and depends only on the density at the coordinate in question.²²¹ LDA approximates the molecular XC energy by the XC energy of a uniform electron gas. The XC energy at a point in the molecule is then compared to a homogeneous electron gas with that density, for which the exchange can be solved analytically and the correlation is approximated through, for example, Monte-Carlo simulation.²²² LDA works surprisingly well in structure prediction, given that the UEG has a uniform density whereas in reality the density varies with position in molecular systems. To incorporate the change of electron density with position, the generalized gradient approximation (GGA) functions include the density gradient, offering improved total energies, energy barriers, and geometries. Of the GGA functionals, the PBE functional has become one of the most used in quantum chemistry.²²³

Hybrid functionals improve upon the GGAs by including a percentage of HF exchange energy. The XC energy is expressed as a combination of the DFT derived XC and the HF exchange energy. The hybrid version of PBE, PBE0, incorporates exact exchange²²⁴

$$E_{XC}^{PBE0} = \alpha E_X^{HF} + (1 - \alpha) E_X^{PBE} + E_C^{PBE}. \quad (4.25)$$

One of the key errors in Kohn-Sham DFT, using the types of functionals introduced thus far, is the self-interaction error. In HF, the electron-electron interaction of the Hamiltonian ensures that an electron will interact with all the other electrons in the system but itself. In DFT, each electron interacts with the entire electron density and thus with itself. If 100% exact exchange is

used this error is exactly cancelled. However, since 100% HF exchange is not present in LDAs or GGAs, the XC-potential does not show the correct asymptotic behaviour, and is only partially remedied by the small percentage of HF exchange in hybrids.²²⁴ At large interelectronic distances, the self-interaction results in incorrect long-range asymptotic behaviour, where the XC potential falls off more rapidly than $1/r$.²²² This causes a huge issue in the description of charge-transfer excitations in time-dependent density functional theory, as shall be discussed in Section 4.4.1

To remedy this, a class of functionals called range-separated hybrids (RSHs) has been developed. The exchange is split into short- and long-range parts, where the short-range exchange will typically be represented by a local or semi-local functional, while the long range exchange is treated by HF exchange.²²⁴ The distance at which the behaviour changes is determined by the range-separation parameter. Therefore, the long-range behaviour can be corrected due to having exact exchange. Whilst hybrid functionals are the most widely used in present day computational chemistry, it is certainly not a “one size fits all” situation, since different functionals are developed to meet certain requirements, often being “property-driven” as much as rooted in theory. In particular, for dealing with excited states, hybrid functionals have known and systematic failings, which the RSH functionals aim to address. This shall be discussed in the next section, where we introduce time-dependent density functional theory (TDDFT).

4.3.1 Basis Sets

Molecular orbitals are constructed from the linear combination of atomic orbitals. These atomic orbitals are represented by mathematical functions called a basis set. A complete set these functions, without any other approximations, would lead to the computation of the exact wavefunction. However, since an infinite basis set is not possible, another source of error in the electronic structure arises from the truncation of the basis set and the number of functions used. Atom-centred basis sets typically consist of Gaussian functions, which hold many numerical advantages over other functional forms for the wavefunction. To adequately describe valence orbitals, more than one basis function is used in what is known as the split valence. Adding polarisation and diffuse functions aid the long range description of the atomic orbital.⁵

For solid state calculations involving periodic systems, it is computationally more efficient to switch from atomic centred orbitals to periodic functions. In the solid state community, plane-wave basis sets are used to sample the unit cell, where the wavefunction is described by one-

electron periodic functions ($e^{i\mathbf{k}\cdot\mathbf{r}}$). The wavefunction is constructed by summing these plane-waves up to an energy cut-off as a function of the frequency. Often the core electrons are approximated by pseudopotentials to lower the computational cost of computing high frequency plane-waves.²²⁵

In the work presented in this thesis, almost all calculations involve atom-centred basis sets. Periodic DFT using plane-waves are used to optimise the unit cells of molecular crystals, from which clusters are extracted and energies calculated as described in Section 2.3.5.

4.4 Methods for Excited States

4.4.1 Time Dependent Density Functional Theory

One of the most popular methods for probing excited states is time-dependent density functional theory (TDDFT). First proposed in 1984 by Runge and Gross, and then extended in 1995 by Casida, TDDFT is a popular approach for modelling the properties of electronically excited states. The fundamental idea within TDDFT is that the dynamics of a system can be completely described by its time-dependent density. Runge and Gross proved that there is a unique, 1:1 correspondence between time-dependent densities and potentials.²²⁶ From the 1:1 correspondence it follows that the time-dependent density is a unique functional of the external potential (and vice versa):

$$V(t) \rightarrow \Phi(\mathbf{r}, t) \rightarrow \rho(\mathbf{r}, t) \quad (4.26)$$

The time-dependent Hamiltonian, and thus the wavefunction, are also functionals of the density, allowing the deduction that all physical observables are functionals of the time-dependent density.

The key quantity in determining the time-dependent density in TDDFT is the time-dependent exchange-correlation (XC) energy. Just as in DFT, TDDFT requires a suitable approximation of the XC-energy. TDDFT uses the XC-energy from DFT and to construct the time-dependent density, in what is known as the adiabatic approximation. The adiabatic approximation assumes that at each moment in time the XC-energy depends only on the instantaneous density.²²²

Solving the time-dependent Schrödinger equation for the wavefunction is not necessary when there is but a small deviation to the ground state, and as such more efficient methods can be used. Excitations are typically calculated in TDDFT using linear response theory, which probes

the response of a system to a weak perturbation. The perturbation causes small time-dependent changes in the density, and the time dependent density can be treated as an expansion of the ground state density plus response densities:

$$\rho(\mathbf{r}, t) = \rho_0(\mathbf{r}) + \rho_1(\mathbf{r}, t) + \rho_2(\mathbf{r}, t) + \dots \quad (4.27)$$

where ρ_1 is the first-order, linear density induced by the first-order perturbation, ρ_2 is the second-order response, *etc.* For absorption processes, this perturbation is an electric field acting on the ground state, and how the system responds contains the information about the system's optical spectrum.²²²

The van-Leeuwen theorem states that a fictitious, non-interacting Kohn-Sham system can replicate the time-dependent density $\rho(\mathbf{r}, t)$ corresponding to an external potential $V(t)$.²²⁷ Likewise, the time-dependent density can be reproduced by the Kohn-Sham potential

$$\rho(\mathbf{r}, t) = \rho[\nu_{KS}](\mathbf{r}, t) \quad (4.28)$$

The linear density response ρ_1 can be evaluated through²²⁸

$$\rho_1(\mathbf{r}, t) = \int_{-\infty}^{\infty} dt' \int d^3 r' \chi(\mathbf{r}, t, \mathbf{r}', t') \nu_1(\mathbf{r}' t') \quad (4.29)$$

where ν_1 is the first order perturbation and χ is the density-density response function, which after Fourier Transform to the frequency domain, yields:²²²

$$\chi(\mathbf{r}, \mathbf{r}', \omega) = \sum_{I=1}^{\infty} \left[\frac{\langle \Phi_{gs} | \hat{\rho}(\mathbf{r}) | \Phi_I \rangle \langle \Phi_I | \hat{\rho}(\mathbf{r}') | \Phi_{gs} \rangle}{\omega - \Omega_I + i\eta} - \frac{\langle \Phi_{gs} | \hat{\rho}(\mathbf{r}') | \Phi_I \rangle \langle \Phi_I | \hat{\rho}(\mathbf{r}) | \Phi_{gs} \rangle}{\omega + \Omega_I + i\eta} \right] \quad (4.30)$$

where $\Omega_I = E_I - E_{gs}$, the excitation energy of state I , $\hat{\rho}$ is the one-particle density operator and η is a convergence factor. When the frequency of the perturbation is equal to the excitation energy, it produces a pole in the response function. This produces a criterion for calculating the excitation energies from the response function. In the Kohn-Sham formulation, the response function is²²⁸

$$\chi_s(\mathbf{r}, \mathbf{r}', \omega) = \sum_{j,k=1}^{\infty} (f_k - f_j) \frac{\psi_j(\mathbf{r}) \psi_k^*(\mathbf{r}) \psi_j^*(\mathbf{r}') \psi_k(\mathbf{r}')}{\omega - \omega_{jk} + i\eta} \quad (4.31)$$

where f_i and f_k are occupation numbers of the orbitals in the Kohn-Sham ground state (1 for occupied, 0 for unoccupied) and ω_{jk} is the energy difference between Kohn-Sham eigenstates. Excitations can be thought of as dynamical processes where the system transitions from one eigenstate to another, such that the excitation is an *eigenmode* of the system.²²⁸ Excitation energies are calculated practically using Casida equation.²²⁹

A well-known failing in TDDFT is the poor description of charge-transfer (CT) excitations, where there is minimal orbital overlap between occupied and virtual orbitals involved in a transition. TDDFT is known to underestimate CT-excitation energies with LDA, GGA, and hybrids, since self-interaction means virtual orbital energies are systematically too low in energy. The RSH functionals have been shown to mitigate this error for CT excitations, with tuned RSH functionals showing equivalent performance wave function methods for the prediction of excitation energies.²³⁰⁻²³² Within the current work, the RSH functional ω B97X-D is used in density functional calculations to incorporate these benefits.²³³

4.4.2 ADC(2) and CC2

In addition to TDDFT, in this thesis post Hartree-Fock methods are used to calculate excited states of molecular systems. This section shall briefly outline the coupled cluster to approximate second order (CC2) and algebraic diagrammatic construction to second order (ADC(2)) methods, which are, like TDDFT, are based on linear response theory. The poles of the response function are found when the perturbation (wavelength of the electric field) is equal to an eigenvalue of system. The response function containing the linear terms can be solved as a generalised eigenvalue problem.

The CC2 method was formulated in 1995 as an approximation of the Coupled Cluster Singles and Doubles (CCSD) method to provide accurate excitation energies but with reduced computational cost.²³⁴ In CC2, the single excitations of CCSD are retained but the double excitations are approximated, reducing the scaling from N^6 to N^5 and with comparable ground state accuracy to MP2.²³⁵ Response functions of CC2 provide accurate transition moments and excitation energies deviated by 0.05-0.15 eV for organic molecules, making it a popular method in probing excited-state properties of molecules.^{236,237}

CC2 is formulated as a generalised eigenvalue problem:

$$\mathbf{A}\mathbf{X} = \mathbf{\Omega}\mathbf{X} \quad (4.32)$$

where $\mathbf{\Omega}$ is a diagonal matrix containing the excitation energies and the matrix \mathbf{A} has elements:²³⁶

$$\mathbf{A}_{\mu_i\nu_j} = \langle \Phi_{HF} | t_{\mu_i}^\dagger \exp(-\hat{T}) [\hat{H}_e, \hat{\tau}_{\nu_j}] \exp(\hat{T}) | \Phi_{HF} \rangle \quad (4.33)$$

where \hat{T} is the cluster operator, t_{μ_i} are the cluster amplitudes and $\hat{\tau}_{\nu_j}$ is the excitation operator.¹⁰ The CC Jacobian is non-Hermitian, which causes numerical problems when excited states become degenerate.^{10,162,235} By being non-Hermitian, it means that the excitation energies must be calculated twice, for the eigenvector acting on the right (as in Equation 4.32 and also acting on the left. This causes numerical instabilities close to state crossings.¹⁰

As an alternative but closely related approach, propagator methods are also used to calculate excitation energies and transition moments. The polarizer propagator introduces the effect of an external field, for instance the absorption of a photon. In the ADC(2), the polarizer propagator acts on the MP2 ground state to give excitation energies at similar accuracy but reduced computational cost compared to CC2.^{238,239} The advantage of ADC(2) over CC2 is that the matrix \mathbf{A} is Hermitian and the excited states can be obtained by diagonalising, unlike in CC2 where Equation 4.32 must be solved twice, for left and right eigenvectors.

ADC(2) is size-consistent and computationally more efficient than CC2, explaining its popularity for investigating large molecules in recent years.²⁴⁰ Propagator methods arose from Green's Functions - mathematical techniques to solve differential equations. The one-electron propagator measures the probability of an electron to move from a to b in time t , whilst the two-electron propagator does the same for two correlated electrons. The *polarizer* propagator describes the time evolution of the polarization of the system with respect to an external perturbation.²⁴¹ As such, the polarizer propagator acts on the ground-state wavefunction propagates time-dependent density fluctuations of the many-body system. The polarizer propagator takes a similar form to the density-density response function in Equation 4.30, where poles correspond to vertical excitation energies.

4.4.3 Methods to Locate Minimum Energy Conical Intersections

Locating conical intersections is important in determining the feasibility of nonradiative decay mechanisms.¹⁷ In particular, the MECI between the ground and first excited state is a local minimum on the S_1/S_0 intersection seam and represents the lower bound for feasible crossings. Various methods to locate the geometry of MECIs for molecular systems have been developed using the gradient difference and nonadiabatic couplings vectors.^{242–246}

In the majority of this work, we use the CIOpt algorithm of Levine, Coe, and Martinez to locate MECIs for single-reference methods, where the derivative coupling vectors are not required.¹⁹ In CIOpt, Lagrange multipliers are used to find the minimum of the objective function

$$F_{JI}(\mathbf{R}, \sigma, \alpha) = E_{JI}(\mathbf{R}) + \sigma G_{JI}(\Delta E_{JI}(\mathbf{R}, \alpha)) \quad (4.34)$$

where

$$E_{JI}(\mathbf{R}) = \frac{E_I(\mathbf{R}) + E_J(\mathbf{R})}{2} \quad (4.35)$$

and

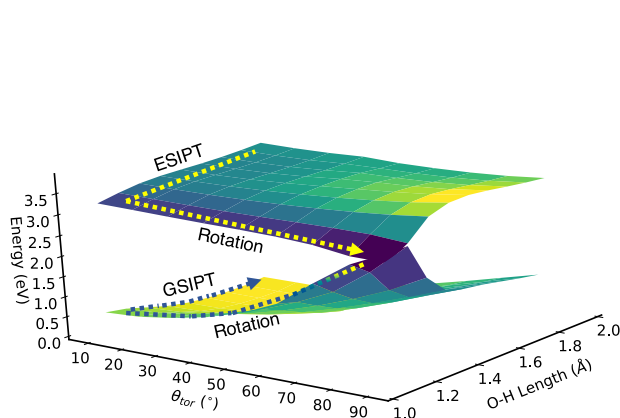
$$\Delta E_{JI}(\mathbf{R}) = E_J(\mathbf{R}) - E_I(\mathbf{R}) \quad (4.36)$$

where $G_{JI}(\Delta E_{JI}(\mathbf{R}, \alpha))$ is a penalty function. Equation 4.34 minimises the average energy of states I and J with the penalty function penalising any step which increases the energy gap. σ alters the penalty weight whilst α is a smoothing factor. The interfacing of CIOpt with a variety of electronic structure codes allows MECIs to be located for a variety of quantum chemical methods.

The topology of conical intersections calculated by different quantum chemical methods has attracted debate in the community.^{247–250} It has been shown that CASSCF and MS-CASPT2 wavefunctions show the correct double-cone topology and a “true” conical intersection. However, surfaces obtained with TDDFT instead have a linear crossing due to there being no nonadiabatic coupling vector.²⁴⁸ ADC(2) methods also show a linear intersection, whereas CC2 surfaces have the correct conical characteristics but can suffer from numerical errors.²⁴⁹ Therefore multireference methods are certainly preferable for modelling S_1/S_0 crossings. However, single-reference methods can provide a qualitative description of the crossings and can produce reliable geometries. Dynamics simulations with these methods have shown for multiple systems that ADC2 and

CC2 can provide reasonable results.^{248,249} In the case of TDDFT, a careful selection of the functional is required.^{251,252} With the computational cost of multireference methods and the sensitivity of their active space, in this work we use a combination of single- and multireference methods, where MECIs obtained with TDDFT, ADC(2), and CC2 methods are compared to those obtained with CASSCF.

5 Nonradiative Decay Mechanisms in 2'-hydroxychalcones



5.1 Introduction

Computational methods have the potential to explain the intriguing luminescence properties of the 2'-hydroxychalcone (**HC**) materials introduced in Section 3.4. **HC** derivatives **1-5** of Figure 3.5 have strikingly different emission characteristics in the solid state, for which we wish to disentangle the intra- and intermolecular contributions. This chapter addresses the intramolecular interactions present in the five systems. The effect of the substituents on the four level ES IPT photocycle are analysed through a combination of static and nonadiabatic dynamics simulations, investigating the relaxation mechanisms and the competition between different deactivation channels in vacuum. These simulations show that a strong electron donating group (EDG) in the *para* position alters the topology of the potential energy surface (PES), destabilising the E* state, thereby assisting and accelerating proton transfer. Our results provide detailed understanding into the fundamental relaxation mechanisms of **H**Cs and the role of the substituents, which is the initial step in unravelling the effect of aggregation on the emission properties.

The computational methods used shall be first described, followed by analysis of the vertical excitations, minima on the excited state, and the feasible relaxation channels. Finally the results of

nonadiabatic dynamics rationalise those obtained in static calculations. The majority of the work presented in this chapter was published in reference 253. To complement the published work, herein there is additional analysis of the nonadiabatic dynamics simulations, where rate constants and lifetimes are explored in more detail using kinetic modelling. The relevant Supporting Information of ref. 253 is incorporated into the chapter and designated appendices. Figures are reproduced from ref. 253 by permission of the PCCP Owner Societies.

5.2 Computational Methods

The ground state geometries of the five compounds were optimised in vacuum using resolution of identity Møller-Plesset perturbation theory to second order (MP2) with the def2-SV(P) and def2-TZVP basis sets.^{254–256} Vertical excitation energies were calculated in vacuum using CC2 and ADC(2) methods under the resolution of identity approximation with the def2-TZVP basis set.^{234,235,257–259} Core electrons were frozen for all MP2, ADC(2) and CC2 calculations. The performance of the ADC(2) and CC2 methods is compared, whilst the effect of the basis set is considered for ADC(2).

Geometry optimisation in the first excited state was carried out in vacuum for **1-5** with ADC(2) and CC2 methods using the same basis sets as the ground state optimisation. These calculations were performed with Turbomole v7.0.²⁶⁰ The level of theory considered to discuss the features of the surfaces is CC2/def2-TZVP, unless otherwise specified.

The CIOpt software package of Levine, Coe, and Martinez was used to determine the location of the minimal energy conical intersection (MECI) structures.¹⁹ The MECI structures were obtained for **1-5** at the CC2/def2-TZVP, ADC(2)/def2-TZVP, and ADC(2)/def2-SV(P) levels of theory. In the case of **1**, the S₁/S₀ conical intersection was optimised with state-averaged CASSCF (SA-CASSCF) with the MOLPRO program.²⁶¹ The active space considered 12 electrons in 11 orbitals including 2 states in the average with the 6-31G(d) basis set (SA-2-CASSCF(12,11)). The CASSCF(14,13) active space was also considered, shown in Appendix A. The PESs were explored through linear interpolation of internal coordinates (LIIC) pathways with ADC(2)/def2-TZVP level of theory. In the case of **1**, the intermediate LIIC geometries were relaxed with the θ_{tor} angle fixed at the CC2/def2-TZVP level of theory. The geometries along the intersection seam also were located using CIOpt.

The absorption spectra of **1-5** were simulated using the nuclear ensemble method. 500 nuclear configurations were generated based on a Wigner distribution of the harmonic frequencies calculated at MP2/def2-SV(P) level of theory.¹¹⁶ Five excited states at ADC(2)/def2-SV(P) level of theory were calculated for each individual geometry. For **1** and **5**, trajectory surface hopping (TSH) nonadiabatic dynamics simulations were performed using NEWTON-X interfaced with Turbomole, at ADC(2)/def2-SV(P) level of theory.²⁶² The initial conditions for the dynamics were generated from the absorption spectra considering an energy window of ± 0.15 eV in the absorption spectra, simulating laser excitation.²⁶³ The geometries contributing to these energy windows were used as initial for the trajectory propagation along with their velocities and momenta. S_0 , S_1 , and S_2 states were included in the dynamics.

For compound **1**, an energy window at absorption maximum of 3.35 ± 0.15 eV was selected for the nonadiabatic dynamics. 50 trajectories were statistically distributed between S_1 (30) and S_2 (20), according to their oscillator strengths. The same protocol was used for compound **5**, with 50 trajectories (S_1 : 30 and S_2 : 20) from an energy window of 3.39 ± 0.15 eV. The maximum simulation time was 500 fs, with a time step of 0.5 fs and the quantum equations were integrated with 0.025 fs using interpolated quantities between classical steps. Nonadiabatic effects were included using the fewest-switches surface hopping algorithm with decoherence corrections (0.1 Hartree). Nonadiabatic couplings between S_2 and S_1 were estimated approximately using an approximated wave-function and the numerical method.²⁴ The trajectories were terminated when the energy gap between S_1 and S_0 was less than 0.1 eV.

5.3 Results

5.3.1 Vertical Excitations

The vertical excitation energies for the first three excited states were calculated for structures **1-5** and are summarised in Table 5.1. Using CC2/def2-TZVP as reference, it is evident that the behaviour of **5** is somewhat different to **1-4**. In **1-4**, there is negligible substituent effect, with a bright $\pi\pi^*$ state predicted for S_1 , where the energy varies by less than 0.05 eV across the four structures. S_2 is a dark $n\pi^*$ state involving the carbonyl nonbonding pair, whilst S_3 is also a dark $\pi\pi^*$ excitation. In compound **5**, the first two excited states are $\pi\pi^*$ with a red shift of 0.17 eV

State	ADC(2)/def2-SV(P)			ADC(2)/def2-TZVP			CC2/def2-TZVP		
	ΔE	f	Character	ΔE	f	Character	ΔE	f	Character
Compound 1									
S ₁	3.53	0.604	$\pi\pi^*$	3.36	0.869	$\pi\pi^*$	3.43	1.135	$\pi\pi^*$
S ₂	3.58	0.391	$n\pi^*$	3.44	0.090	$n\pi^*$	3.67	0.009	$n\pi^*$
S ₃	3.97	0.013	$\pi\pi^*$	3.77	0.008	$\pi\pi^*$	3.84	0.003	$\pi\pi^*$
Compound 2									
S ₁	3.53	0.483	$\pi\pi^*$	3.38	0.806	$\pi\pi^*$	3.43	1.167	$\pi\pi^*$
S ₂	3.59	0.551	$n\pi^*$	3.46	0.196	$n\pi^*$	3.68	0.023	$n\pi^*$
S ₃	3.96	0.010	$\pi\pi^*$	3.77	0.007	$\pi\pi^*$	3.85	0.005	$\pi\pi^*$
Compound 3									
S ₁	3.59	1.022	$\pi\pi^*$	3.40	1.063	$\pi\pi^*$	3.47	1.286	$\pi\pi^*$
S ₂	3.64	0.075	$n\pi^*$	3.51	0.013	$n\pi^*$	3.75	0.002	$n\pi^*$
S ₃	4.06	0.046	$\pi\pi^*$	3.86	0.038	$\pi\pi^*$	3.96	0.034	$\pi\pi^*$
Compound 4									
S ₁	3.53	0.404	$\pi\pi^*$	3.36	0.857	$\pi\pi^*$	3.42	1.105	$\pi\pi^*$
S ₂	3.57	0.589	$n\pi^*$	3.42	0.096	$n\pi^*$	3.65	0.005	$n\pi^*$
S ₃	3.86	0.002	$\pi\pi^*$	3.65	0.008	$\pi\pi^*$	3.72	0.028	$\pi\pi^*$
Compound 5									
S ₁	3.42	0.647	$\pi\pi^*$	3.20	0.522	$\pi\pi^*$	3.26	0.633	$\pi\pi^*$
S ₂	3.52	0.012	$n\pi^*$	3.39	0.066	$n\pi^*$	3.54	0.390	$\pi\pi^*$
S ₃	3.67	0.337	$\pi\pi^*$	3.50	0.358	$\pi\pi^*$	3.66	0.094	$n\pi^*$

Table 5.1: Vertical excitation energies, oscillator strengths, and orbital character for compounds **1-5** at various levels of theory. The corresponding ground state was calculated with the MP2 method with the corresponding basis set. All energies are in eV.

compared to **1**, with the oscillator strength of S₂ increased at the expense of S₁, with the $n\pi^*$ state shifted to S₃.

The electron density difference maps between S₁ and S₀, Figure 5.1, reveal the origin of differing excitation pattern in **5**. For **1-4**, the excitation to S₁ involves density transfer from the unsaturated bridge of the system (connecting the phenol and dimethylaniline rings) to the carbonyl π^* orbital. For **5**, electron density is transferred not from the bridge but from the phenol ring, due to the electron-rich conjugation of the methoxy group. Considerable electron density is transferred from the hydroxyl oxygen, increasing the acidity of the proton. The S₂ state in **5** has the same character as S₁ in **1-4**. Thus the strong electron donor in **5** perturbs the electron density with respect to the other four compounds, changing the character of the bright state with a greater electron depletion at the hydroxyl oxygen. This shall be shown to be important in the following sections as we analyse the relaxation in the excited state.

Comparing the performance of ADC(2) and CC2 methods, when the same basis set is used

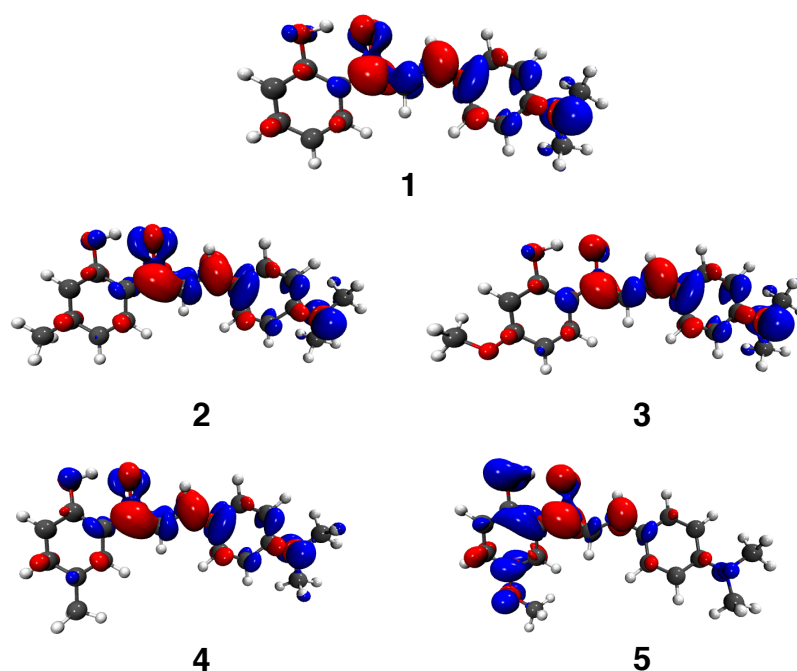


Figure 5.1: Electron density difference maps (S_1-S_0) for **1-5**, showing electron density loss in the ground state (blue) and gain in the excited state (red), calculated at CC2/def2-TZVP level of theory.

(def2-TZVP), ADC(2) vertical excitation energies are about 0.1 eV deviated to the red with respect to the CC2 values. In the case of ADC(2), the def2-SV(P) basis set shifts the energies to the blue in about 0.1 eV. With this basis set there is mixing of the S_1 and S_2 states, where S_2 borrows intensity from S_1 due to $\pi\pi^*$ and $n\pi^*$ mixing, which is present in CC2 but to a lesser degree. The simulation of the spectra, Figure 5.2, using a Wigner-distributed sample of nuclear configurations at the ADC(2)/def2-SV(P) level of theory shows a red shift of 0.1-0.2 eV due to vibrational broadening. Similar shifts are expected for all levels of theory.

5.3.2 Excited State Minima

Minima in the first excited state for all compounds were optimised using ADC(2) and CC2 methods. The respective energy levels are depicted in Figure 5.3. An electron donating group (EDG) in *meta* (**2** and **3**) has a negligible effect on the energies of E^* . However, if the substituent is in *para* (compounds **4** and **5**), no stable E^* minimum can be located. For **1-3**, relaxation to a local minimum in E^* is *via* intramolecular rotation. To describe this mode, the torsional rotation angle

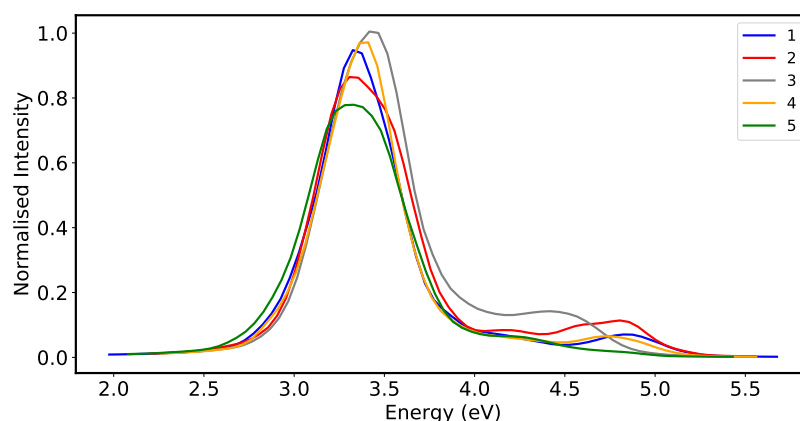


Figure 5.2: Simulated absorption spectra of **HC 1-5** at ADC(2)/def2-SV(P) level of theory.

θ_{tor} is defined in Figure 5.4.

Two E^* minima can be found depending on the direction of rotation and in the case of **1**, both minima are energetically equivalent. For **1-3**, the energy difference between these minima is very small (< 0.01 eV) and the two minima (forward or backwards rotation) can be considered degenerate. Torsion through 180° results in cis-trans isomerisation, with the trans isomer about 1 eV less stable than cis in S_1 (at ADC(2), Figure 5.10). Consequently, full cis-trans isomerisation is unlikely.

At the E^* minimum $\theta_{tor} = 44^\circ$ for **1**, there is a stabilisation of approximately 0.54 eV with respect to the FC state. Compounds **2** and **3** pass through similar minima, with $\theta_{tor} = 46^\circ$ and 54° respectively. Potential energy curves and our nonadiabatic dynamic simulations show that ESIPT from this geometry is improbable. Therefore when occupied the E^* minimum acts as a sink for the wavepacket to prevent ESIPT, as confirmed by Zahid *et. al* experimentally.²⁰² The emission energies from the E^* state for **1**, **2** and **3** are 1.63, 1.59, and 1.46 eV respectively, but with negligible oscillator strength.

In the K^* state, where the proton has migrated, the system relaxes *via* intramolecular rotation about θ_{tor} . Two minima with very similar energies can be also located depending on the direction of rotation. The θ_{tor} value ranges between 40° and 60° . These minima are about 1 eV below the excitation energy corresponding to the FC geometry, and are more stable than E^* minima. As such a bias towards the ESIPT mechanism can be expected, whilst the relative stabilisation with respect to the S_1 energy for the FC geometry is quite similar for all the derivatives (about 1 eV).

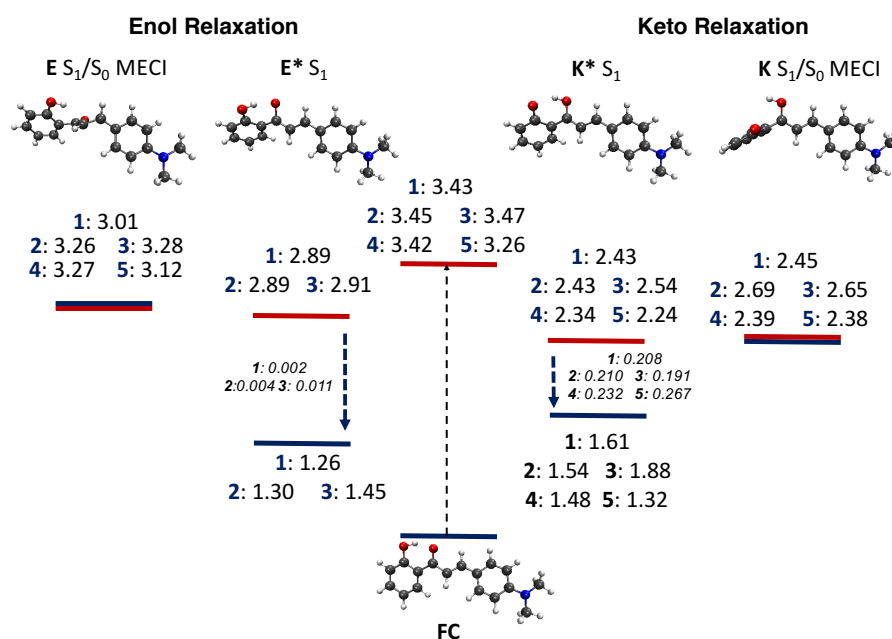


Figure 5.3: Relative energies (in eV) for all derivatives calculated at CC2/def2-TZVP level of theory. In all cases, the energy of the ground state was taken as reference. S_1 - S_0 oscillator strengths at S_1 minima are also given in italics.

The emission from K^* is in the range of 0.7-1.0 eV for all molecules, but has negligible oscillator strength. S_1 energies (for K^* and E^*) with ADC(2) method are in good agreement the obtained with CC2 (within the 0.1-0.2 eV range). At the same time, ADC(2) destabilises the K ground state with respect the CC2 method. This behaviour has consequences for the optimisation of MECI and the description of the S_1/S_0 crossing seam using the ADC(2) method, which are discussed in the next section.

5.3.3 Relaxation Channels

From the Franck-Condon state, the wavepacket can relax through the enol channel to the E^* minimum, or the ESIPT channel to the K^* minimum. These two competing channels are depicted in Figure 5.3. In each channel, the MECI was located to determine the feasibility of nonradiative decay *via* a nonadiabatic crossing. For **1**, the MECI geometries were optimised with CC2 methods using the def2-SV(P) and def2-TZVP basis sets. For comparison, the conical intersections were also located with CASSCF(12,11)/6-31G(d) and CASSCF(14,13) levels of theory. The ge-

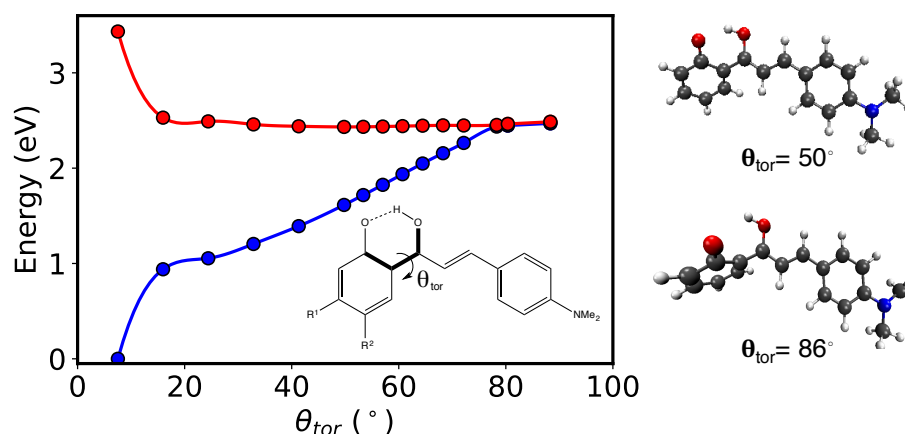


Figure 5.4: Relaxed linear interpolation pathway between the FC state and the MECI. LIIC located six geometries between the FC state K^* minimum, followed by LIIC to locate 10 geometries between the K^* minimum and MECI. All geometries were relaxed at CC2/def2-TZVP level of theory with θ_{tor} fixed.

ometry of the K^* S_1/S_0 MECI obtained with the CC2 method is in very good agreement with that obtained with CASSCF, $\theta_{tor}=88^\circ$ (89° with CASSCF method). The route-mean-square deviation (RMSD) deviation between the two geometries is just 0.08 \AA . The geometries obtained with both basis sets are very similar.

For **1**, the MECI lies at only 0.02 eV above the K^* minimum, whilst the substituents slightly increase the energy of the MECI ($0.1\text{-}0.2 \text{ eV}$) in **2-5**. Nevertheless, the MECIs remain accessible during the relaxation. To determine if any barriers exist between the K^* minimum and the MECI, we optimise the intermediate states of a linear interpolated pathways, fixing θ_{tor} , at CC2/def2-TZVP level of theory for **1**. This is shown in Figure 5.4. At the K^* minimum, $\theta_{tor} = 50^\circ$, and further 30° rotation takes the molecule to the intersection seam. In this region of the potential energy surface, the S_1 energy does not change significantly with θ_{tor} , which can be associated with an extended crossing seam as previously described by Robb *et al.* in an analogous ESIPT system.²⁶⁴

The static calculations suggest that the dominant relaxation process involves a proton transfer step followed by rotation about θ_{tor} . ESIPT is facilitated by the K^* minimum, which is more stable than E^* . Experimentally, **4** and **5** do not show fluorescence either in solution or solid state. In the case of the solid state, the lack of fluorescence has been associated with the crystal packing, however these calculations suggest that the character of the substituent might also play a role. This

shall be further investigated in the next chapter.

The ADC(2) geometries for the K^* S_1/S_0 MECI of all studied compounds show a θ_{tor} angle significantly deviated from CC2 and CASSCF values, with the crossing seam reached at a much smaller angle. The ADC(2) MECI structures are very similar to the K^* minima, rotated by a further 10° . This behaviour is associated with the description of the ground state with the MP2 method, which could artificially destabilise S_0 and thus the S_1/S_0 crossing occurs at smaller angles. Similar results were found with def2-SV(P) and def2-TZVP basis sets.

The non-ESIPT relaxation channel is also accessed *via* intramolecular rotation in the E^* state, leading to a second MECI. The stabilisation of these MECI structures involves relaxation through θ_{tor} , which is significantly larger for **1** with a value of about 124° (144° with CASSCF). For **1**, we also observed relaxation through the H-C-C-H dihedral angle (88°). For the rest of the S_1/S_0 MECI structures (**2-5**), only θ_{tor} deviates from the plane. For **1-3**, the E^* MECIs are slightly higher in energy than the E^* minima (0.2-0.3 eV). Considering the small energy gap and the absence of barriers, the crossing seam region should be accessible. Another mechanism is the direct relaxation to the MECI from the FC geometry, which is the only possibility for **4** and **5**, considering the lack of a stable E^* minimum. These calculations show that the competition between the ESIPT and the relaxation to E^* will depend on the substituent. In the case of **4-5**, a heavy bias towards the ESIPT is expected. Nonadiabatic dynamic simulations confirm this analysis.

5.3.4 Nonadiabatic Dynamics

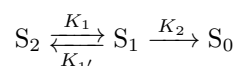
For these systems, the S_1 PESs obtained with ADC(2) are in a good agreement with the CC2 prior to the conical intersection. The greater computational efficiency of ADC(2) over CC2 also makes it attractive for the study of the first steps of the excited state dynamics of **HC** systems, although the results when the energy of S_1 and S_0 converge must be analysed with care. In particular, it is expected that excited state lifetimes may be underestimated. From a technical point of view, there are known problems with the stability of CC2 for TSH dynamics, and as such ADC(2) is the method of choice employed here.¹⁶²

Compounds **1** and **5** represent the extreme cases, with most significant difference in the electronic structure of the excited states. The dynamics simulations thus use **1** and **5** as exemplars, a strategy which will also be used in Chapter 6. The PESs show that rotation around the angle θ_{tor}

is activated during relaxation (in E^* and K^*). TSH allows analysis of the competition between different relaxation pathways and the role of rotation in the mechanism. The first steps of the photorelaxation of **1** and **5** were explored using nonadiabatic dynamics considering two excited states (S_2 and S_1), which are close in energy. The simulations confirm that the main deactivation pathways are associated with relaxation to the K^* and E^* minima, with both mechanisms involving rotation about θ_{tor} . The competition between the two relaxation channels strongly depends on the substituent.

First we analyse the decay rates of the electronic states by fitting a kinetic model of the population of the S_2 , S_1 , and S_0 adiabatic states. For each of **1** and **5**, 50 trajectories were run, 60% of which started on the S_1 electronic surface and 40% on the S_2 surface. At each time step, for S_2 and S_1 , the number of trajectories on each electronic surface represents the population of that state. Since a trajectory is stopped when the S_1 - S_0 energy gap is less than 0.2 eV, the S_0 population is simply the number of halted trajectories. Throughout the dynamics, the electronic population of the state coefficients was monitored compared to the population of the adiabatic states to ensure consistency of the algorithm. As such, the number of trajectories in each state is a viable method to monitor the populations.

The TSH simulations allow population transfer between S_2 and S_1 , and vice versa. Population can also transfer to S_0 , through halted trajectories. Based on this, the following reaction scheme is used to model the populations:



This yields the set of differential equations

$$\frac{dS_2(t)}{dt} = K_{1'}S_1(t) - K_1S_2(t) \quad (5.1)$$

$$\frac{dS_1(t)}{dt} = K_1S_2(t) - K_2S_1(t) - K_{1'}S_1(t) \quad (5.2)$$

$$\frac{dS_0(t)}{dt} = K_2S_1(t) \quad (5.3)$$

which were integrated using the open-source computer algebra system Maxima and solved using the least-squares method implemented in the `optimize.curve_fit` function of the `scipy`

Compound	K_1	$K_{1'}$	K_2
1	14.40	0.10	4.62
5	98.86	6.66	10.48

Table 5.2: Calculated rates of population transfer between electronic states for **1** and **5**. Rates are given in units of ps^{-1} .

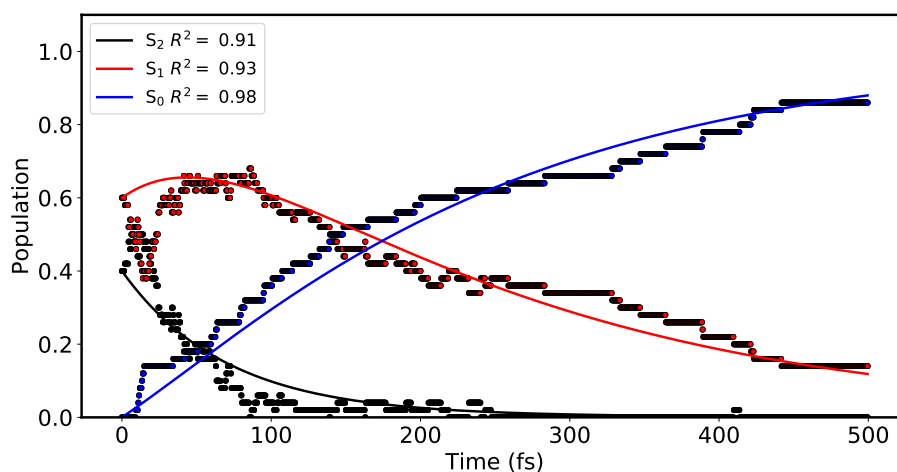


Figure 5.5: Fit of the rate constants for excited state decay of S_2 , S_1 , and S_0 for compound **1**.

python package.^{265,266} The global fits for the populations of S_2 , S_1 and S_0 are shown in Figures 5.5 and 5.6 for **1** and **5** respectively. The calculated rates of K_1 , $K_{1'}$ and K_2 are given in Table 5.2. It should be stated that the relatively few number of trajectories (50) renders the calculated rates to be no more than qualitative. Nevertheless, the analysis can provide a general understanding of the excited state decay process.

In compound **1** there is initially a transfer of population from S_1 to S_2 , shown by the markers in Figure 5.5. Although this transfer is included in the model, through $K_{1'}$, the calculated rate is too low to pick up this small fluctuation and it is missed in the fit, accounting for the worse fit of S_2 and S_1 compared with S_0 . This effect is not present in compound **5**.

In both compounds there is fast population transfer from S_2 to S_1 , followed by a longer-lived S_1 state. The decay of S_2 in **5** is nearly seven times faster than in compound **1**. In the S_1 state, decay to S_0 is more than twice as fast in **5** than in **1**, and thus the excited state is less stable with the addition of the methoxy group. The longer lifetime of S_1 for compound **1** can be attributed to the stability of the E^* channel, where seven trajectories remain beyond the 500 fs simulation time. For compound **5**, just one trajectory remained active at 500 fs.

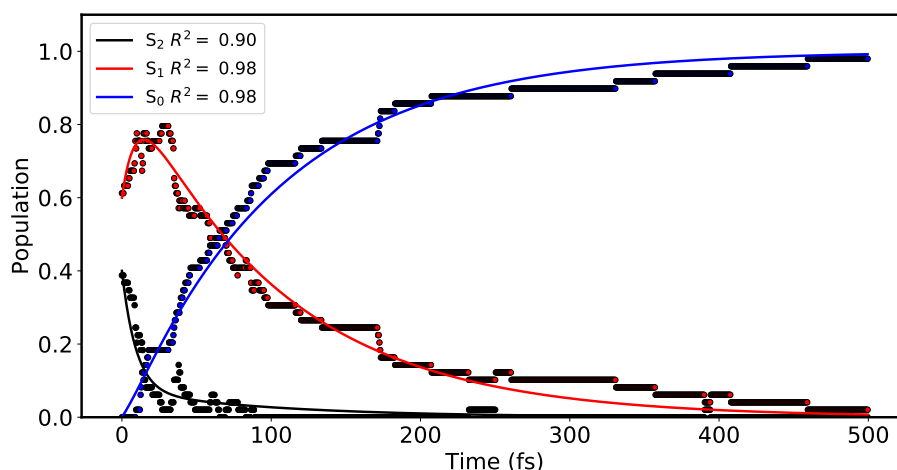
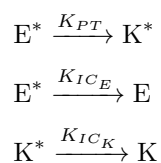


Figure 5.6: Fit of the rate constants for excited state decay of S_2 , S_1 , and S_0 for compound **5**.

To further analyse the excited state decay pathways, we track the populations of the enol and keto tautomers during the dynamics. Four states are of interest: E^* , K^* , E , and K , representing the excited and ground state species of each tautomer. A classification for E^* and K^* based on bond distances is used. Throughout the dynamics, the distance D between the hydroxyl proton and the phenol (O_P) and carboxyl oxygen (O_C) is tracked. When $D_{O_P} \leq D_{O_C}$, the molecule is in the E^* state, and when $D_{O_P} > D_{O_C}$ the molecule is in the K^* state. Early in the dynamics, the O-H stretch vibration is active, which in some trajectories causes large oscillations in the O-H distance and a fluctuation between E^* and K^* states. As such, we further impose on the classification that the molecule is in E^* until the final oscillation occurs. This separates the vibrational relaxation from the ES IPT process. As the E and K species reside on the S_0 surface, which is never explicitly occupied, their population is classified by identifying whether the molecule is in E^* or K^* when the trajectory is halted due to the energy gap of S_1 and S_0 becoming less than 0.2 eV. It is then assumed that population decays through conical intersection to the corresponding ground state in E or K . If in E^* at $t = x$, the trajectory is then classified as E for the remaining $500-x$ femtoseconds of the analysis, and likewise for K^* . At each timestep, the number of trajectories in E^* , K^* , E , and K are counted, with the total population summing to 50, the total number of trajectories. Note that each trajectory can only occupy one species at any time, and all trajectories begin the simulation in the E^* state.

In a similar vein to the global fits for the adiabatic states, the tautomer populations were mod-

elled using a set of three rate equations,



where K_{PT} represents the ESIPT rate, K_{ICE} is the internal conversion process in enol and K_{ICK} is the keto internal conversion.

After integration with the maxima package, the following integrated rate equations were obtained:

$$\mathbf{A} = \mathbf{B} \cdot \mathbf{C} \quad (5.4)$$

$$\mathbf{A} = \begin{bmatrix} E^*(t) \\ K^*(t) \\ K(t) \\ E(t) \end{bmatrix} \quad (5.5)$$

$$\mathbf{B} = \begin{bmatrix} 1 & 0 & 0 \\ \frac{-K_{PT}}{K_{PT}+K_{ICE}-K_{ICK}} & \frac{K_{PT}}{K_{PT}+K_{ICE}-K_{ICK}} & 0 \\ \frac{K_{PT}K_{ICK}}{(K_{PT}+K_{ICE}-K_{ICK})(K_{PT}+K_{ICE})} & \frac{-K_{PT}}{K_{PT}+K_{ICE}-K_{ICK}} & \frac{K_{PT}}{K_{PT}+K_{ICE}} \\ \frac{-K_{ICE}}{K_{PT}+K_{ICE}} & 0 & \frac{K_{ICE}}{K_{PT}+K_{ICE}} \end{bmatrix} \quad (5.6)$$

$$\mathbf{C} = \begin{bmatrix} \exp(-(K_1 + K_2)t) \\ \exp(-K_3t) \\ 1 \end{bmatrix} \quad (5.7)$$

The global fits for the tautomer states are shown in Figures 5.7 and 5.8, and the calculated rates are shown in Table 5.3. Again, due to the relatively few trajectories, these models provide only a qualitative picture of the decay of each species. In compound **1**, K_{PT} (the rate of ESIPT) is 2.71 ps^{-1} , more than five times slower than in compound **5**. Note that all ESIPT events happen on the S_1 surface. The increased rate in **5** can be traced back to the electronic densities in Figure

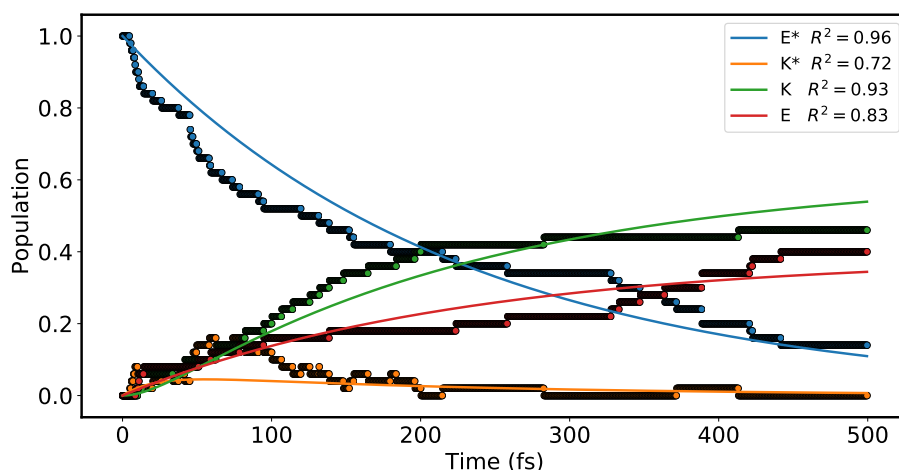


Figure 5.7: The population of the E*, K*, E, and K states for compound **1** from TSH simulations.

Table 5.3: Obtained rates for proton transfer, internal conversion in E* and K*, for **1** and **5**, in ps⁻¹.

Compound	K_{PT}	K_{ICE}	K_{ICK}
1	2.71	1.71	47.14
5	14.00	2.52	36.69

5.1, where in compound **5** the phenol oxygen loses density and the proton is more acidic than in **1**. In Figure 5.7, the fit for the K* decay in compound **1** is quite poor, and thus it is expected that K_{PT} is underestimated by this model. Alternative models were made by introducing bounds for the coefficients, and the best fit for K* decay gave a rate constant of 5.00 ps⁻¹, but to the detriment of the other fits (E*, E, K). From these TSH simulations, K_{PT} for compound **1** is expected to be between 2-6 ps⁻¹, and between 2-5 times faster in compound **5**. Certainly, more trajectories would enable a more quantitative picture of the process.

The internal conversion rates are more similar for the two compounds. These timescales are within the same magnitude of those obtained by Zahid *et. al*, although direct comparison is complicated by the fact that the experimental timescales involve solvation, which is not included in these simulations.²⁰² The calculated internal conversion rates are expected to be overestimated, due to the instability of the S₀ state with the ADC(2) method as discussed in Section 5.3.3. This means that the conical intersection is accessed at lower rotation angles than with CC2.

In the case of **1**, both pathways enol and keto decay pathways are similarly populated in the dynamics simulations (K*: 48%, E*: 52%). The population of the different pathways depends on

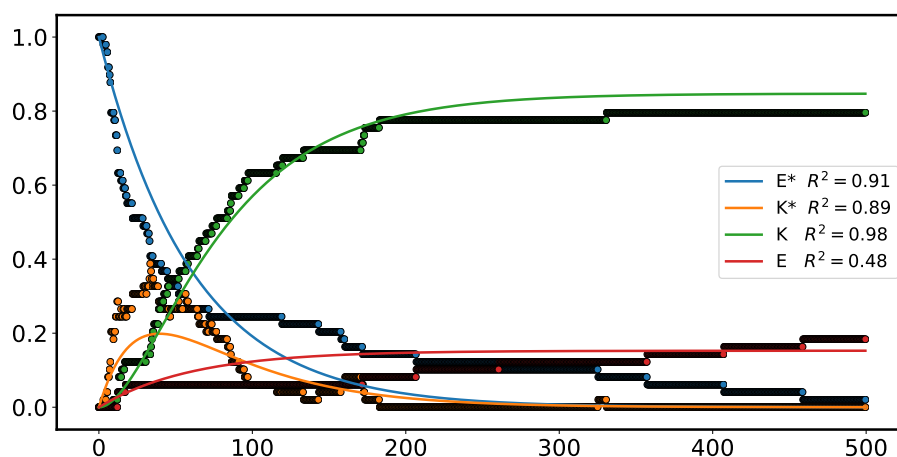


Figure 5.8: The population of the E*, K*, E, and K states for compound **5** from TSH simulations.

the initial state. For trajectories started in S_2 , the fraction is larger (K*: 60%, E*: 40%). For **1**, the significant population of the E* channel is associated with the stabilisation of the E* minimum and the lower acidity of the proton due to the electronic density distribution, as shown in Figure 5.1. Conversely, compound **5** shows a significant bias for the K* channel, with ESIPT occurring in 80% of trajectories, showing a similar channel preference regardless of the initial state. The methoxy group results in the increased acidity of the proton and lack of stable E* minimum, and a heavy bias for the ESIPT channel. This is evident from the fast population transfer from E* to K* in Figure 5.8.

For **1** and **5**, the average time for the first proton transfer is 85 ± 86 fs and 43 ± 62 fs respectively, with all trajectories exhibiting ESIPT finding the ground state before the maximum simulation time (500 fs). Note that these averages differ from those which we published in reference 253, where the first proton transfer was defined as the time at which $D_{OP} > D_{OC}$, regardless of whether the proton then migrated back in an oscillatory manner. This lead to average times of 59 fs and 10 fs for the ESIPT process, which are perhaps underestimated due to not separating the vibrational oscillation from the ESIPT process.

Analysis of the trajectories shows three steps in the ESIPT mechanism can be identified:

1. Relaxation and oscillation in the excited state (E* form)
2. Proton transfer (ESIPT)
3. Relaxation in K* followed by internal conversion

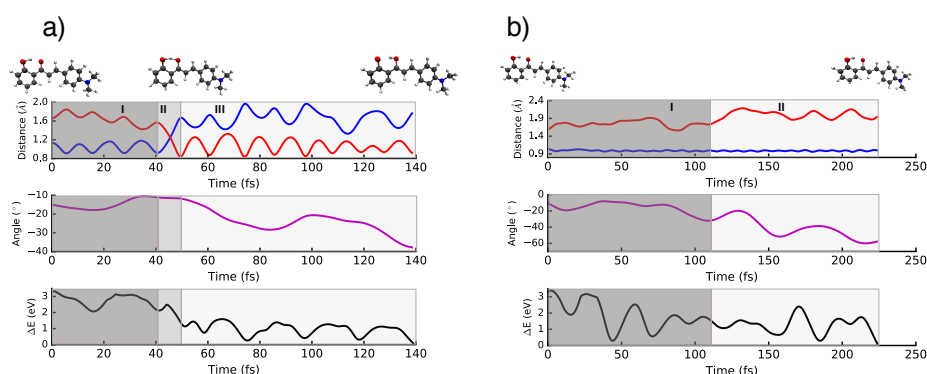


Figure 5.9: Two exemplar trajectories of compound **1**. Panel a), left, shows a trajectory undergoing ES IPT, with the associated O-H distances, dihedral angle, and energy gap between S_1 and S_0 . The same parameters are shown in panel b) for a trajectory which relaxes in the E^* channel.

These three steps are illustrated for a typical trajectory in panel a) of Figure 5.9. During step 1, the angle decreases to $\theta_{tor}=11^\circ$ to facilitate the proton transfer in step 2. In some trajectories, the proton oscillates somewhat before transferring. ES IPT in step 2 occurs at 45 fs. In step 3, the molecule relaxes in the keto form *via* dihedral rotation after which dihedral rotation of 37° results in state convergence after 139 fs, which is underestimated considering the limitations of the ADC(2) method. The region with S_1/S_0 gap of 0.1 eV is accessed in an average time of 76 fs post-ES IPT for **1** and 47 fs for **5**. Considering the features of the PES at ADC(2)/def2-SV(P) level of theory, these times are underestimated with respect to real internal conversion times, but they provide a relative indication of how fast the molecules reach the crossing seam region and the effect of the substituent.

Alternatively to ES IPT, the molecule can remain in the E^* state. The mechanism of intramolecular rotation in E^* comprises two steps:

1. Relaxation in the E^* minimum, which is close to the Franck-Condon geometry.
2. Further relaxation leading to the internal conversion

Both processes involve the rotation around the angle θ_{tor} . 20% of the trajectories deactivated through this channel did not reach the crossing region within the simulation time. In the case of **5**, where there is not a E^* minimum close to the Franck-Condon geometry, the molecule relaxes directly to the crossing seam region. On average, the crossing region is reached within 228 fs for **1** and 241 fs for **5**.

In panel b) of Figure 5.9, a typical trajectory undergoing E* relaxation is shown. At 0 fs, $\theta_{tor} = -10.5^\circ$, and for the first 110 fs of the simulation (step 1), the angle oscillates about the equilibrium value (-11.0° at ADC(2)/def2-SV(P) level of theory). Then, the rotation deviates the phenoxy group from the plane prohibiting ESIPT and the molecule reaches the CI region at 225 fs, with an $\theta_{tor} = -57.6^\circ$. The dynamics support the assertions from the PESs that proton transfer from the twisted E* form, with a barrier of 1.2 eV, is improbable. Relaxation in E* therefore competes with ESIPT in compound **1** due to the close proximity of a local minimum close to the Franck-Condon geometry. Proton transfer followed by internal conversion is the faster process, with an average time duration of 123 fs, compared to 228 fs for rotation in E*.

The nonadiabatic dynamic simulations employed here do not allow the prediction of post-internal conversion behaviour, but the analysis of the PES can help understand the following steps in the mechanisms. Post-ESIPT, two relaxation pathways are possible once the MECI is populated. The first completes the four-level photocycle and returns the system to the ground state cis-enol form *via* GSIPT. The second continues the rotation about θ_{tor} to produce the trans-keto form of **HC**. Optimisation at the MP2/def2-TZVP level show this structure is more than 1 eV less stable than the ground state, suggesting that GSIPT will be preferential. This is shown schematically in Figure 5.10 at ADC(2) level. The TSH simulations clearly illustrate the effect of a strong electron donor in the *para* position on the ESIPT process in **H**Cs. The population of the ESIPT channel and rate of proton transfer is greatly increased as is subsequent convergence of the ground and first excited state.

5.4 Conclusions

In this chapter computational methods have been applied to investigate the photochemistry of five derivatives of **HC**, an ESIPT-active compound with potential application in organic lasers and optoelectronics. Experimental data show that **H**Cs are non-emitting in solution and only fluoresce through AIE.¹⁸² The calculations provide theoretical description of the ESIPT process and subsequent relaxation mechanisms of **H**Cs in gas phase, which represents the first step for the understanding of the photochemistry of these systems.

Through calculation of vertical excitation energies and corresponding absorption spectra, we find that electron donating groups have but a small influence of the absorption characteristics of

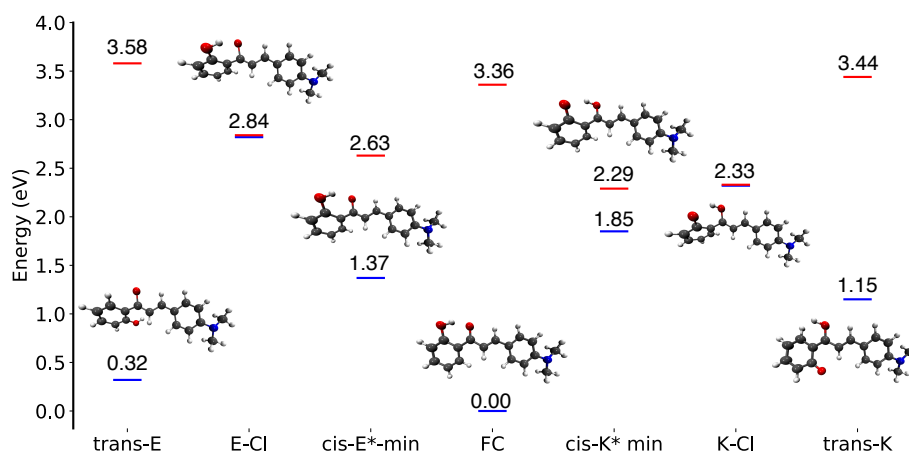


Figure 5.10: Energies of important optimised energies on the PES of **1**. Ground states optimised at MP2/def2-TZVP, whilst excited state minima optimised at ADC(2)/def2-TZVP level of theory.

HC. It takes a strong electron donor in the *para* position to alter the vertical excitation energy, on account of the increased conjugated electron density. On the other hand, relaxation back to the ground state is far more sensitive to the electron donating power of the substituent and its positioning on the phenol moiety. Dual-emission is inhibited with an EDG in *para* for **HCs**. This is quite unexpected, with a comprehensive study on the effects of substituents in common ESIPT-compounds finding that electron donating groups in any position favour the E* form, showing the complex nature of ESIPT chromophores.¹⁴⁰

The ground state is accessible *via* nonradiative channels from both E* and K* states. This analysis has recently been confirmed experimentally, employing transient absorption and emission spectroscopy, as discussed in Section 3.4.2.^{202,203} S₁/S₀ MECI structures were found for all compounds, associated with an extended crossing seam. Both mechanisms involve the activation of an intermolecular rotation mode about the θ_{tor} angle. The competition between E* and K* channels depends strongly on the position and nature of the substituent. Proton transfer is more favourable with electron donating groups in *para*, correlating with donating power and increased electron density loss at the phenol oxygen. Nonadiabatic surface-hopping dynamic simulations provide a full picture of relaxation energetics and timescales.

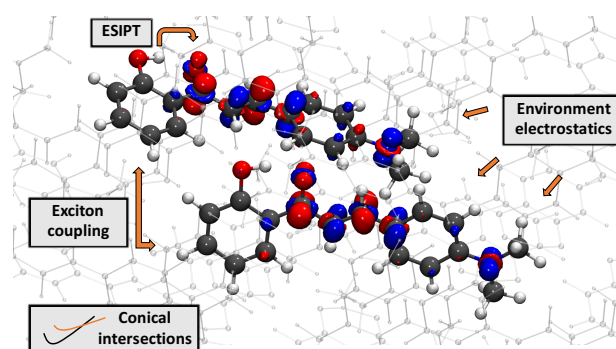
ESIPT is strongly favoured for **4-5**, where there are not stable E* minima. For compound **5**, the reaction coordinate is completely downhill correlating with intramolecular rotation. The dynamic simulations show a bias towards the K* relaxation mechanism. Experimentally, **4** and **5**

do not fluoresce either in solution or solid state. Cheng *et al.* suggested that for the solid material, this behaviour is related to the crystal morphology.¹⁸² Our calculations show that the character of the substituent and the electronic effects in the monomers might also play a role in the mechanism.

The conical intersection in both the enol and keto channels offer a route for ultrafast internal conversion and reversion to the ground state equilibrium structure. The fact that these conical intersections are reached *via* the main excited state relaxation coordinate, intramolecular rotation, and that they are energetically accessible, suggests that they are the main cause of nonradiative decay in these systems. This is an important discovery, and shows that the AIE behaviour of these systems can be interpreted through the RACI model (Section 3.2.3). This model is less established than the FGR-RIM, with fewer examples in the literature, in part due to its more recent proposal.

In the next chapter the knowledge of the electronic properties of **1** and **5** shall be used to probe the excited state decay process in the molecular crystal, viewed through the lens of the RACI model. The question remains of why **5** is still nonemissive in the solid state whilst **1** undergoes a switch-on of fluorescence. To probe this, we shall examine the intermolecular interactions in the molecular crystal and their importance in relation to the electronic properties of the chromophore.

6 Inter- and Intramolecular Interactions in the Solid State



6.1 Introduction

In Chapter 5, the nonradiative decay mechanisms in vacuum were established for the **HC** derivatives **1-5** (Figure 3.5). The two extreme cases were compounds **1** and **5**, where the methoxy group of **5** alters the electronic structure of the chromophore. This results in a slight red shift in the absorption, but a more pronounced effect on the relaxation mechanism. Whilst for compound **1** relaxation through the enol and keto channels is evenly distributed, ESIPT is greatly preferred in compound **5** due to the increased acidity of the migrating proton. All systems can relax to the ground state *via* an accessible conical intersection in either the enol or keto channel.

In the solid state, compounds **1-3** undergo AIE whereas **4** and **5** remain dark. In this chapter, a combination of theoretical models are used to understand the emission properties in the solid state. In particular, we focus how inter- and intramolecular processes determine the emissive properties in the crystal environment. To provide a complete picture of the factors affecting decay mechanisms in these materials, we use a combination of solid state and excited state embedding calculations to systematically account for the different intermolecular interactions present in the molecular crystal. This involves creating cluster models where a central chromophore is treated

with a QM electronic structure method and the exterior molecules are described with an MM force field, in the QM:MM ONIOM approach (Section 2.3.5). As for our nonadiabatic dynamics simulations in Section 5.3.4, in this chapter the two extreme compounds, **1** and **5**, shall be used as exemplar systems (Figure 6.1). In **1**, chromophores aggregate in a slip-stacking, herringbone structure in an edge to face arrangement. Conversely, in **5** the dominant configuration is the face to face π - π stacking of chromophores. In Chapter 7, the dimer configurations shall be investigated further.

With the conical intersections located in vacuum in Chapter 5, we approach the the solid state modelling with the intention of understanding how the crystalline environment changes the structure, energy, and accessibility of the conical intersections in these systems. Does the RACI interpretation for AIE apply for compound **1**, and is an accessible conical intersection responsible for the nonfluorescence of compound **5** in the solid state? This chapter answers these questions.

The work herein was published in reference 267. The data shall be presented in dedicated sections here, incorporating the Supporting Information, rather than the letter format chosen for publication, although the order of the discussion remains similar. Important to note that while in ref. 267 the compounds were labelled as **1** and **2**, in this work the original numbering of Chapter 5 is retained - thus compound **2** of ref. 267 is compound **5** herein. This chapter is organised in the following way. First, the computational methodology is discussed, where we detail the combination of electronic structure methods and embedding models. Second, since the electronic structure method is TDDFT for this section, we benchmark vacuum-phase results against those in Chapter 5. Next, the absorption in the solid state is analysed taking into account monomer and dimer chromophores and the excitonic interactions present in the molecular crystal. Excited state minima and conical intersections are then optimised to determine the excited state relaxation mechanism in the molecular crystal and rationalise the observed fluorescence of **1** and the nonradiative decay of **5**. Finally, the results are summarised to offer some design rules for ESIPT/AIE systems. All calculations and analyses were performed by myself apart from the Ewald embedding calculations, implemented and performed by Miguel Rivera. All figures are reprinted with permission from ref. 267. Copyright 2018 American Chemical Society.

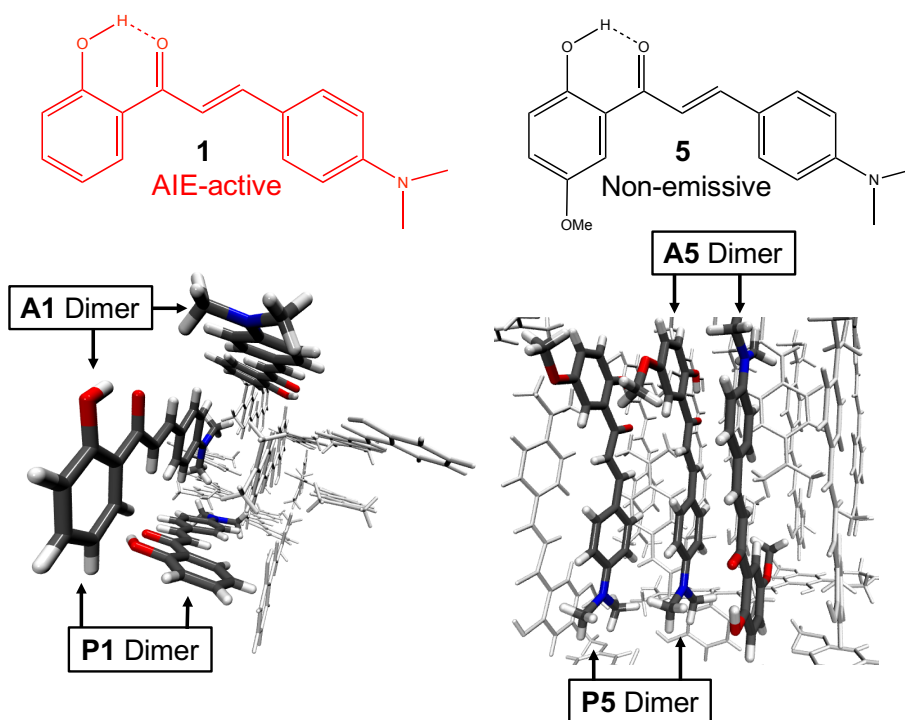


Figure 6.1: The molecular and crystal structures of the **1** and **5** Compound **1**, left, displays AIE behaviour, whereas **5**, right, is nonemissive in both aqueous and solid phases. Also labelled are the parallel (**P**) and antiparallel (**A**) dimer configurations.

6.2 Computational Methodology

The cluster models of **1** and **5** are based on the experimental crystal structures deposited with the CCDC, codes 941991 and 1061608 respectively.¹⁸² The crystal structures of **1** and **5** were initially optimised using Quantum Espresso in the periodic DFT framework.²⁶⁸ Optimisation of each unit cell was carried out with DFT-D2 (PBE) with a plane-wave cutoff of 30 Ry and a Monkhorst-Pack k-point grid of 2x3x2 in accordance with the shape of the unit cell. Clusters of varying size were cut from the DFT-D2-optimised cell for the ONIOM calculations.

The solid state photochemistry of **1** and **5** is modelled by applying the ONIOM scheme in a QM:MM protocol using DFT and TDDFT as the QM electronic structure method.^{62–64} This is an attractive route to efficiently evaluate the mechanism of AIE, as the chromophore can be treated within the necessary QM framework whilst the surrounding crystal structure can be evaluated using MM methods. For each cluster, the surrounding molecules were fixed in their lattice posi-

tions during geometry optimisation of the central chromophore and computed with the AMBER force field using ESP charges derived from a vacuum HF/3-21G* calculation of a monomer cut from the crystal structure, allowing electrostatic embedding of a QM-derived electronic density - a scheme we denote AMBER(HF).⁷⁸

For all models discussed in the following sections, the focus is four important regions of the PES; the Franck-Condon point (FC), enol (E*) and keto (K*) minima, and the S₁/S₀ MECI. These were established as important points in the vacuum calculations of Chapter 5. Ground and excited state minima and the MECI structures were calculated at the ONIOM(ω B97X-D/6-31G(d)):AMBER(HF) level within the DFT and TD-DFT framework. Energies at the ground and excited state minima were recalculated with the 6-311++G(d,p) basis set. Additionally, RI-CC2/def2-TZVP embedded calculations were performed. The CIOpt algorithm of Levine, Coe and Martinez was again applied to determine the location of the minimal energy conical intersection (MECI) structures.¹⁹ The nature of the MECIs were confirmed with the CASSCF method in both vacuum and solid state, explained in detail below.

For each of **1** and **5**, three ONIOM((TD-)DFT):AMBER(HF) clusters of differing size are evaluated:

- **M7**: all molecules within 7Å of a central monomer chromophore
- **M15**: all molecules 15Å from the central monomer
- **D7**: all molecules within a 7Å-radius from the centroid of a dimer chromophore

The cluster models are visualised in Figures 6.2-6.4. Two **D7** dimer models were considered due to the prominence of two dimer arrangements in each of the crystal structure, where monomers are arranged parallel (**P**) and antiparallel (**A**). The parallel stacked dimer model is denoted **D7-P** and the antiparallel configuration is **D7-A**. These stacking arrangements are shown in Figure 6.1.

ONIOM calculations were performed with the electrostatic embedding scheme. Post optimisation, single point calculations in vacuum of each ONIOM((TD-)DFT):AMBER(HF) geometry were performed to evaluate how the environment influences the energy. To assess the role of the quantum mechanical electrostatic potential during relaxation, we also perform optimisation for the **M7** and **M15** models with mechanical embedding. The nature of vertical excitations in solid state was assessed using the CALCDEN method, which classifies electronic excitations based on the electronic density localisation between donating and accepting orbitals.^{116,269}

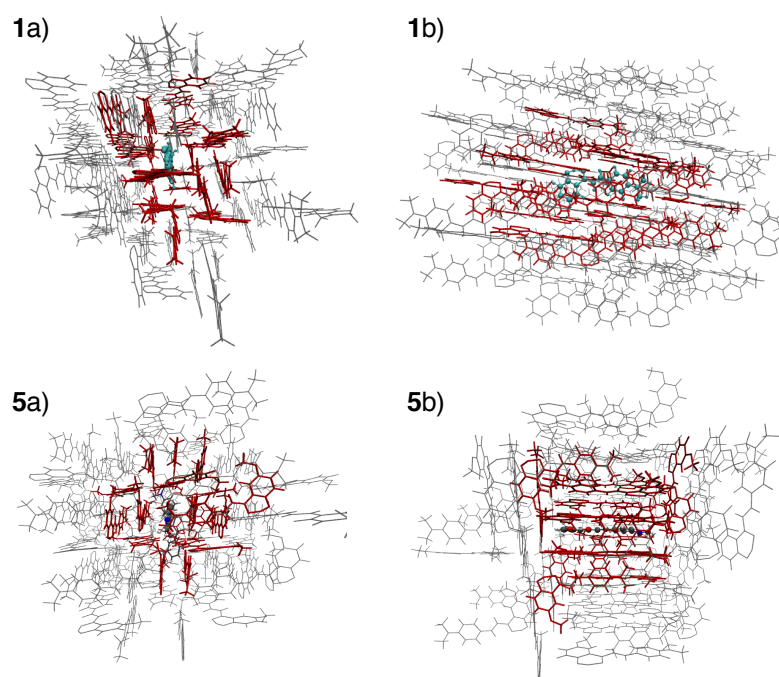


Figure 6.2: Two viewpoints *a* and *b* of the **M7** and **M15** models for compounds **1** and **5**. The central molecule is shown in cyan, surrounded by an increasing radius of 7 Å (red, **M7**) and 15 Å (red+grey, **M15**).

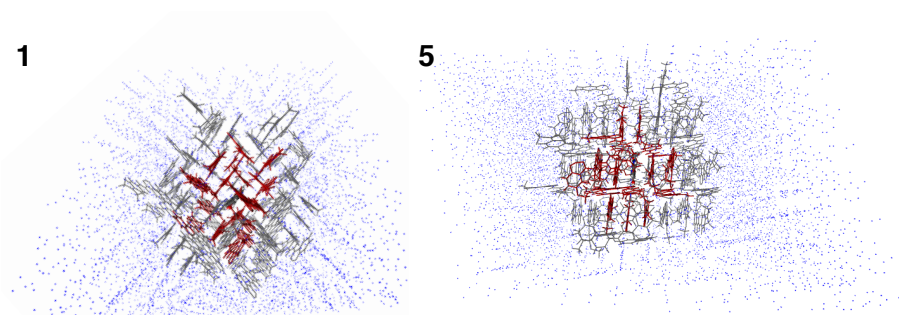


Figure 6.3: Visualisation of the **Ewald** model for compounds **1** and **5**, where the **M15** model (cyan + red + grey) is embedded in Ewald point charges, shown in blue.

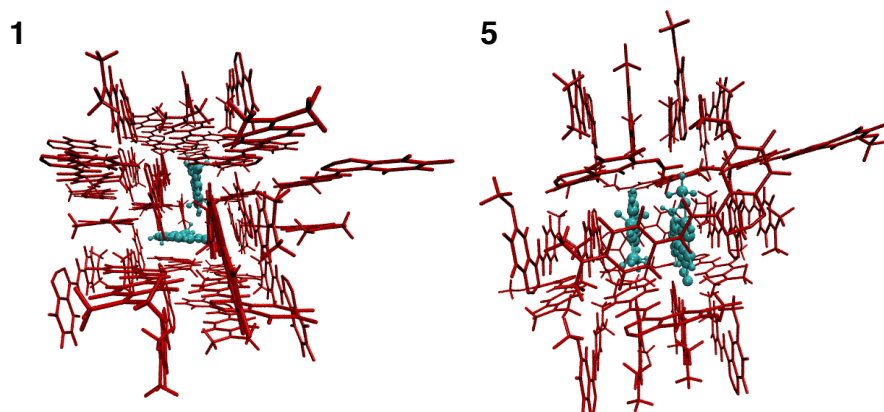


Figure 6.4: The **D7** model for compounds **1** and **5**. The dimer chromophore is shown in cyan, and the surrounding molecules within a radius of 7\AA are shown in red.

To simulate the long-range periodic electrostatic environment experienced by the chromophore, the **M15** model was embedded in point charges derived from the Ewald method of Derenzo, Klintonberg and Weber, as described in Section 2.3.5.^{86,87} In the **Ewald** model, the chromophore was embedded in a set of point charges for each of the S_0 and S_1 minima and MECI geometries found with **M15** model. The initial charges were the same ESP charges used in the ONIOM models. 500 points had a fixed charge value, 1000 sample sites were used and the supercell was comprised of $4 \times 4 \times 4$ unit cells.

The topology of the PES between the K^* minimum and the MECI was explored for the **M15** model through LIIC, using the 6-31G(d) basis set. A relaxed geometry scan of the torsional angle θ_{tor} was also performed for the **M15** model with the 6-31G(d) basis set to probe the PES of the K^* state. All ONIOM calculations were performed with Gaussian 09 (rev D.01).²⁷⁰

The energies at the FC state and K^* minimum for the **M15** chromophore were calculated at the RI-CC2/def2-TZVP level of theory using point charge embedding with TURBOMOLE v7.0.^{258,260} The point charges were located at the atomic positions of the MM-atoms in the **M15** model.

We validate the TDDFT calculated MECI geometry of **1** and **2** in the solid state by optimising the conical intersection with the state-averaged complete active space self-consistent field method, using an active space of 12 electrons in 11 orbitals with the 6-31G(d) basis set

(SA-CASSCF(12,11)/6-31G(d)):AMBER(HF). The MECI geometry is optimised within the **M7** model with AMBER force field to describe the MM-level, in which all the positions of all MM atoms are frozen during the optimisation. All CASSCF calculations were performed using the MOLCAS@UU v8.0 binaries, using the Tinker v.6.3.3 interface for the QM/MM calculations.^{271,272}

Intermolecular interactions are studied within Kasha's exciton framework (Section 2.3.2). The diabaticization scheme of Troisi was implemented to calculate the excitonic couplings J (Section 2.3.4).⁴⁹ The dimer chromophore optimised in S_0 in each **D7** model were extracted and single point calculations were performed of the dimer and the constituent monomers to construct the adiabatic Hamilton and the transformation matrix from the transition dipole vectors. The exciton couplings were calculate using the `exciton_coupling` python package developed by myself, which has been made open-source.²⁷³

The multi-model approach ensures size-consistency of the MM-region, evaluates the role of short and long-range interactions, explicitly models the long-range electrostatic potential from the crystal, and determines the role of excitonic coupling on the mechanistic interpretation.

6.3 Results

6.3.1 Benchmarking of TDDFT

Since the electronic structure method of choice in this chapter is TDDFT, it is important to initially benchmark against the post-Hartree Fock methods used in Chapter 5. In this section we briefly compare the vertical excitations, relaxation pathways, and conical intersection geometries. Previous studies have shown that TDDFT performs well compared to CC2 for studying ESIPT.²⁷⁴

For the vertical excitations in vacuum with TD- ω BX-D/6-311++G(d,p) (Table 6.1), the results of **1** and **5** compare well with CC2/def2-TZVP (Table 5.1). The character of the first three states is the same across the methods, with S_1 as the bright state $\pi\pi^*$ for **1**. For compound **5**, with TDDFT S_2 borrows intensity from S_1 , as with CC2 and ADC(2). The relative red shift of **5** is also similar (0.17 with CC2, 0.12 with TDDFT). It is evident that at the Franck-Condon geometry TDDFT can provide the same trends as CC2 and ADC(2), but at lower computational cost.

The excited state minima and MECIs in the enol and keto channels were also optimised for **1-5** in vacuum with TD- ω BX-D/6-311++G(d,p). The energies are shown in Figure 6.5. For **1**

and **5**, the surfaces were also obtained at TD- ω BX-D/6-31G(d) level, shown in Appendix B. The energies obtained are very similar to ADC(2) and CC2, with the keto minima at lower energy than the enol minima for **1-3**. As with ADC(2) and CC2, no enol minima were obtained with TDDFT, and thus the same propensity for ESIPT will be witnessed for **5**. The enol minima occur at more planar θ_{tor} angles for **1-3**, and therefore a larger emission energy is predicted. For **5**, similar is seen with the keto minimum, where the equilibrium geometry is more planar and thus a larger energy gap is present.

For the MECIs in vacuum, the geometry obtained with TDDFT compare well with those obtained with CASSCF and CC2. Indeed, the TDDFT geometry is most similar to CASSCF and does not suffer from the problems of ADC(2). The K* MECI in vacuum was calculated for **1** and **5** with the SA(2)-CASSCF(12,11)/6-31G(d). The geometries are compared to those obtained in vacuum at the TD- ω BX-D/6-311++G(d,p) level of theory in Figure 6.6. There is an excellent agreement between the CASSCF(12,11)/6-31G(d) calculated MECI geometry (shown in cyan) and the TD- ω BX-D/6-311++G(d,p) geometry (black). For compound **1**, left, the RMSD between the two methods is 0.11 Å. For compound **5**, the geometries are more deviated, with an RMSD of 0.59 Å. This deviation arises due to the dihedral angle at the amino group of the molecule, which is 13° for TDDFT and 60° for CASSCF. The dihedral angles of the deprotonated phenol ring, the coordinate which drives the convergence of states, are a good match (89.9° for TDDFT vs 90.2° for CASSCF). The agreement between the TDDFT K* conical intersection with the geometry of the CASSCF-predicted MECI in vacuum show that the protocol we employ to explore the PES with TDDFT is robust. As such the choice of TDDFT should not alter the conclusions obtained with ADC(2) and CC2. In this chapter, we also carry out single point calculations with CC2, but TDDFT is the main method chosen due to its computational efficiency and readily available implementation for QM:MM methods in ONIOM with Gaussian software. The conical intersections are also calculated using the QM:MM scheme incorporated in Molcas, using SA(2)-CASSCF(12,11)/6-31G(d):AMBER(HF) to validate the conical intersections calculated with TDDFT in ONIOM.

6.3.2 Absorption in the Molecular Crystal

In this section examine the absorption in the molecular crystal. For all models, the crystal environment shifts the bright state to the red with respect to absorption in vacuum. The bright state

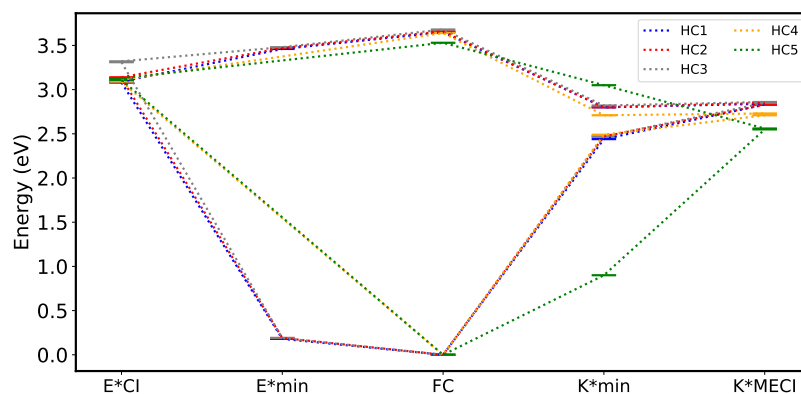


Figure 6.5: The critical points on the PES for **1-5** obtained at (TD)- ω BX-D/6-311++G(d,p) in vacuum.

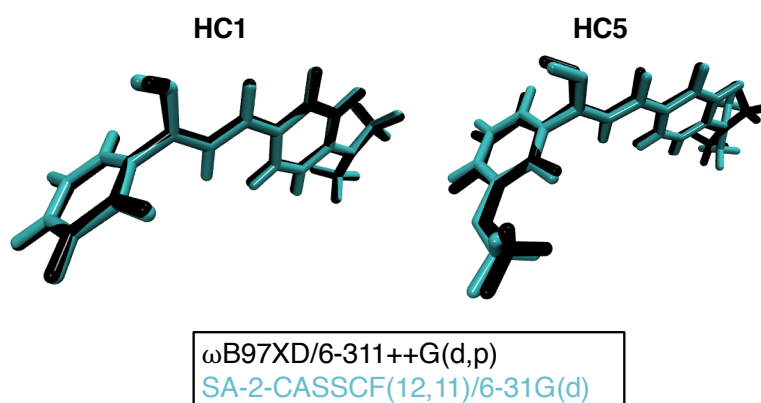


Figure 6.6: Comparison of the TD- ω BX-D/6-311++G(d,p)(black) and SA-CASSCF(12,11)/6-31G(d) (cyan) MECI geometries for compounds **1** (left) and **5** (right).

calculated for **1** with the **M** and **D** models (Table 6.1) are in very good agreement with the experimental value of 3.3 eV.¹⁸² The bright state is calculated as 2.93 eV with RI-CC2/def2-TZVP. In the case of **5**, where no experimental absorption spectrum has been published, the energies predicted with all models are in the range of 3.4-3.5 eV. In this case the RI-CC2/def2-TZVP value of 3.33 eV aligns better with TDDFT than in **1**. There is no significant intermolecular charge transfer upon excitation in either material.

The electrostatic potential generated by the whole crystal (in the **Ewald** model) has a negligible effect for the vertical excitations of **1**, with a convergence of 3.3 eV for the bright state. In the case of **5**, a more polar structure, the effect is more significant, with a shift in the energy of around

Table 6.1: Excitation energies and oscillator strengths for the first three excited singlet states of **1** and **5** in various models. Energies calculated at ω B97X-D/6-311++G(d,p) level of theory and given in eV.

		Compound 1		Compound 5	
		Energy (eV)	Osc.(f)	Energy (eV)	Osc.(f)
Vacuum	S ₁	3.65	1.143	3.53	0.870
	S ₂	3.95	0.007	3.87	0.244
	S ₃	4.16	0.002	3.93	0.013
M7	S ₁	3.20	1.177	3.42	0.905
	S ₂	4.10	0.001	3.74	0.236
	S ₃	4.27	0.030	4.00	0.002
M15	S ₁	3.30	1.174	3.40	1.005
	S ₂	4.07	0.002	3.72	0.147
	S ₃	4.18	0.018	4.01	0.015
Ewald	S ₁	3.30	1.192	3.50	0.815
	S ₂	4.06	0.002	3.81	0.320
	S ₃	4.16	0.015	3.90	0.008
D7-P	S ₁	3.16	0.017	3.18	0.029
	S ₂	3.26	2.128	3.51	1.379
	S ₃	3.57	0.003	3.60	0.001
D7-A	S ₁	3.10	0.061	3.05	0.000
	S ₂	3.35	2.063	3.42	1.947
	S ₃	3.79	0.006	3.61	0.012

0.1 eV. Since this is in the order of the shift associated with vibrations and does not change the nature of the excited states, even the smaller cluster models (**M7** and **D7**) can capture the main electrostatic influence on the photoexcitation.¹¹⁶ However, more accurate crystalline properties would be achieved by using a more sophisticated approach for the low-level system rather than molecular mechanics, such as QM:QM' embedding methods currently under development in the Crespo-Otero group.^{89,90} This is particularly important for finding equilibrium structures on the excited state surface.

In going from a monomer chromophore to a dimer chromophore, the bright state shifts from S₁ to S₂. For the Frank-Condon (FC) geometry, the electronic density is delocalised over both molecules in the chromophore. As a consequence of excitonic coupling, the bright state is blue shifted in 0.06 eV and 0.15 eV for **1** and 0.23 eV and 0.32 eV for **5** (**M7** model as reference). This is typical of H dimers within the Kasha excitonic coupling model, with oscillator strengths of S₂ almost double those of the monomer species in S₁.⁴¹ While the splitting is more significant for **5**, this does not alone explain the different properties of **1** and **5**. The role of H and J dimers in the aggregates will be investigated in the next chapter.

Table 6.2: J coupling values (eV) between units in dimers of **1** and **5** in the **D7** models

	Compound 1	Compound 5
	J (eV)	J (eV)
D7-P	0.060	0.112
D7-A	0.105	0.150

The largest coupling (Table 6.2) in each compound occurs when the monomers are aligned antiparallel (**A**), of the order of 100 meV, which are in the order of those obtained for some organic semiconductors.⁵⁰ These couplings result from the favourable alignment between the nitrogen of one monomer and carbonyl group on the other monomer (approximately 4.5Å). Recently, the effect of excitonic couplings on the nonradiative constants for AIE was evaluated.¹¹⁸ For a set of five highly aromatic conjugated molecules, with J s in the order of 10 meV, the authors found that excitonic coupling always increases the nonradiative decay constants. Based on these vibronic models, in the E^* form, a larger J on the nonradiative vibrational decay should be expected for **5**. In the next chapter, the excitonic couplings of the **HC** crystals shall be investigated in more detail.

6.3.3 Radiative vs. Nonradiative Decay

Relaxation to either E^* or K^* minima will follow photoexcitation. The emission energies and oscillator strengths for each model are collected in Table 6.3. In the case of **1**, significant reabsorption is expected due to the small Stokes shift for the E^* minimum. This has been recently confirmed experimentally.²⁰² For **5**, oscillator strengths from E^* are extremely small. In this context, no significant emissive response is expected from the E^* state of either material. For **1**, relaxation in E^* involves localisation of the electronic density on one molecule, whereas delocalisation is observed for **5**. In vacuum and the **M7/15** models, E^* is not stable for **5**. It is stable in the dimer models due to state mixing where some of the S_2 character of the monomer mixes with S_1 , such that there is less electron density lost from the phenol oxygen in S_1 .

Geometries of the E^* and K^* minima are planar in the solid state. Since no double proton transfer K^* minimum was found for **1**, emission is expected from a localised K^* state. The experimental emission spectrum for **1** can be assigned to the K^* state ranging from 1.5-2.1 eV. The predicted values are blue shifted to 2.7 eV (CC2/def2-TZVP predicts emission at 2.2 eV). The flatness of the S_1 surface with respect to the dihedral angle suggests that emission from a range of

Table 6.3: Emission energies and oscillator strengths from the enol and keto minima on the S_1 PES for various models. Energies reported at TD- ω BX-D/6-311++G(d,p) level of theory and given in eV.

	Compound 1		Compound 5	
	E* (<i>f</i>)	K* (<i>f</i>)	E* (<i>f</i>)	K* (<i>f</i>)
M7	3.03 (1.207)	2.67 (1.191)	-	2.15 (0.461)
M15	3.10 (1.225)	2.61(0.977)	-	2.17 (0.490)
Ewald	3.12 (1.214)	2.66 (1.052)	-	2.18 (0.486)
D7-P	3.01 (0.479)	2.56 (0.725)	2.45 (0.002)	2.15 (0.312)
D7-A	2.96 (0.119)	2.59 (0.616)	2.81 (0.000)	2.32 (0.388)

geometries is possible. To investigate this, a relaxed geometry scan was performed at TD- ω BX-D/6-31G(d):AMBER(HF) for both **1** and **5**, where θ_{tor} was incrementally increased in the **M15** model and frozen during relaxation, shown in Figure 6.7. Between 0 and 40°, the S_1 surface is quite flat, whilst the energy gap between S_1 and S_0 states ranges from 2.7 eV ($f=0.973$) to 2.2 eV ($f=0.496$). The flatness of the surface, and the high oscillator strengths along the coordinate, suggest that emission from a range of dihedral angles less than 40° is possible, in particular since dihedral rotation energetically favourable relaxation pathway in vacuum. Also important to take into account when considering the emission energies are the limitations of the QM:MM method. All of the exterior atoms are frozen and treated at MM level, without the possibility of any mutual polarisation between the regions. As such, the environment cannot respond to the changes in electronic density of the chromophore, which can be rather large in the case of ESIPT systems. As such, the additional relaxation from mutual charge polarisation is not present here, and the emission energies are somewhat overestimated. The dimer models partially alleviate this by having a polarisable molecular counterpart, and the emission energy is reduced.

In **5**, there exists a double- K^* state, where both monomers undergo ESIPT. This state is non-emissive in S_1 ($f=0.002$) lying 0.5 eV above the bright FC state. The localised single proton transfer state in **5** has emission in the range 2.2-2.3 eV (1.7 eV with CC2). Oscillator strengths, though half the value of the obtained for **1**, are still significant (0.312 and 0.388). Therefore, while emission from **1** should be brighter than from **5**, radiative mechanisms alone cannot explain the negligible quantum yield of **5**. The structural similarity of the E^* and K^* minima, namely that the E^* state is planar, means that the pathways no longer compete in the excited state. The bifurcation seen in vacuum is not expected to exist in the solid state, and relaxation to K^* can follow relaxation in E^* . To maximise the quantum yield, efficient population transfer K^* is important, since little

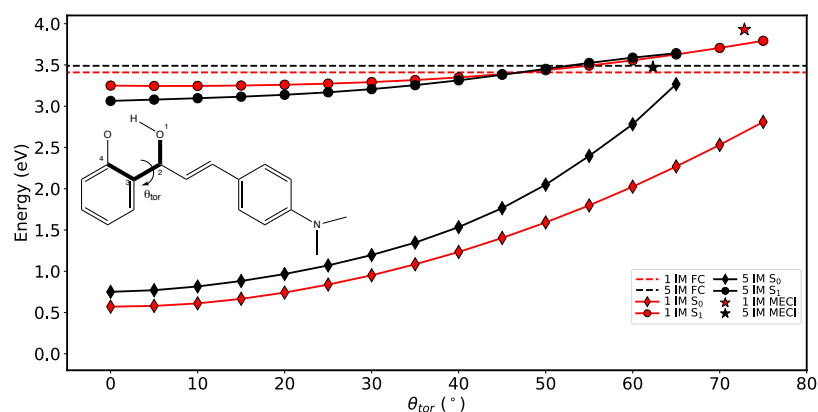


Figure 6.7: Relaxed geometry scan of the dihedral angle θ_{tor} calculated at ONIOM(ω B97X-D/6-31G(d)):AMBER level of theory for compounds **1** (red) and **5** (black) in the **M15** model. Also plotted are the bright excitation energies (dashed lines) and the MECI energy (stars) for both compounds in the **M15** model.

emissive response will be witnessed from E^* due to the small Stokes shift.

The location of the nearest CI to the E^* and K^* minima can help understand the balance between radiative and nonradiative decay. In Chapter 5, we saw that in vacuum both pathways lead to energetically accessible conical intersections *via* intramolecular rotation. In the solid, intramolecular rotation in E^* is completely blocked and the E^* CI is accessed instead *via* a stretch of the bridging unsaturated bond. This is associated with an energy cost of upward of 5 eV from the FC S_1 energy for both crystals. Consequently, molecular aggregation completely blocks the E^* nonradiative decay pathway in both **1** and **5**. For **1**, the S_1/S_0 MECI associated with the K^* state lies 0.5-1.0 eV above the S_1 energy for the FC geometry (Figure 6.8). For **5**, the S_1/S_0 MECI is classically accessible with a barrier of 0.4 eV from the K^* minimum. While less favourable than in gas phase (barrier 0.2 eV), the system has enough energy to access the conical intersection. Therefore, in compound **5** the excited state population can decay nonradiatively through the MECI and back to the ground state, whereas in **1** the population remains in the K^* state until fluorescence.

LIIC between the K^* minimum and MECI show the existence of a barrier of 1.4 eV (w.r.t to FC S_1) to reach the MECI for **1** compared to 0.14 for compound **5** (Figure 6.9). It is important to state that the LIIC barriers represent an upper bound for barriers on the PES and the true barriers will be smaller, since coordinated relaxation was neglected at each step. However, the barriers here offer further evidence that the MECI of **1** is inaccessible and **5** is not.

To further explore the electrostatic effect, the critical points of the PES were re-optimised

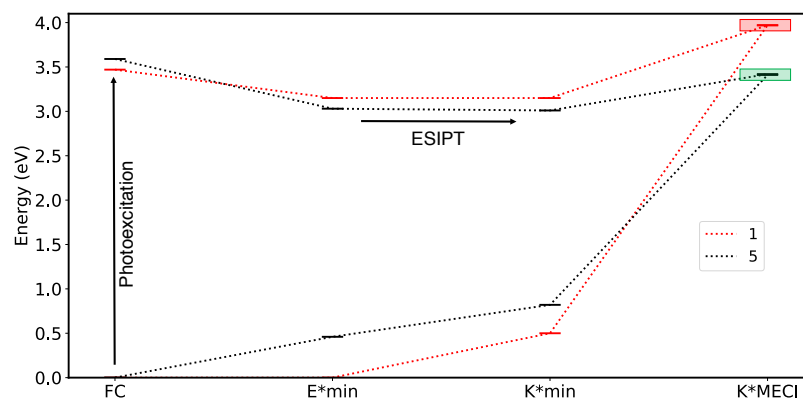


Figure 6.8: Energy of the S_0 and S_1 states at the Franck-Condon (FC) point, E^* and K^* minima, and the MECI of **1** and **5** with the **D7** model with ONIOM(ω B7X-D/6-31G(d)):AMBER level of theory. The accessibility is colour coded.

without electrostatic embedding for the monomer models. The energies in comparison to those obtained with electrostatic embedding are given in Table 6.4. Crucially, the accessibility of the MECI depends on its stabilisation with respect to the initially populated excited states. For compound **1**, the electrostatic potential stabilises the S_1 state at the FC region but has a smaller effect on the energy of the MECI. Both of these factors decrease the accessibility of the nonradiative channel. A similar effect is seen for both the **M7** and **M15** models, suggesting that these are short to medium range effects and are not as a result of long-range Coulombic interactions. For **5**, the stabilisation of the MECI is larger than for the S_1 state. Therefore the accessibility of the MECI in **5** is aided by the short-range electrostatic interactions with the surrounding molecules when treated at QM-level.

Moreover, within the mechanical embedding approach, the MECI geometries are similar, but both MECI have energies lying above the photopopulated state for **5** and below for **1**. This indicates that steric hindrance in the crystal determines level of distortion of the MECIs, but a quantum-mechanical treatment of Coulombic interactions modulate their total energies. The same conclusions can be drawn from the monomer models, for which the energy levels of **M15** are shown in Appendix C. As mentioned above, there is no E^* minimum located for **5**. As such, it is expected that the short range interactions present in the dimer chromophore restrict torsional relaxation, whilst long range electrostatic interactions, imperfectly included in these models due to the lack of self-consistent polarisation, can help stabilise the excited state, particularly when the

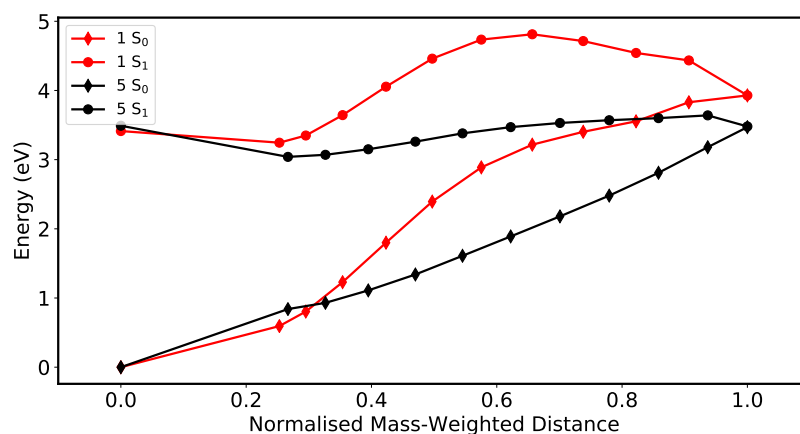


Figure 6.9: Linear interpolation of internal coordinates between the Franck Condon state, the S_1 minimum, and the MECI for **1** and **5**.

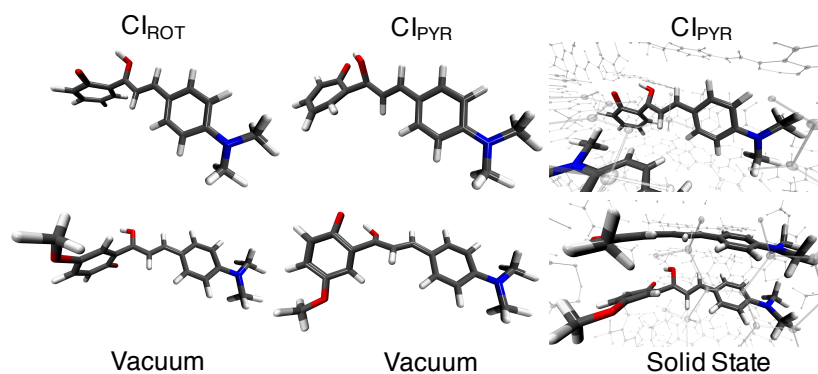


Figure 6.10: Geometry of the K^* MECI in vacuum (left and center) and in the solid state (right) for **1** (top) and **5** (bottom).

geometry of the chromophore most resembles the exterior charge distribution, as at absorption.

The K^* MECI is accessed *via* a combination of intramolecular rotation (ROT) and carbonyl pyramidalisation (PYR), with a puckering of the deprotonated phenol ring (Figure 6.10). In contrast with the most stable conical intersections (CI_{ROT}) in vacuum, the MECI structures in the solid state (CI_{PYR}) display a significant pyramidalisation of the carbonyl carbon, with a puckering angle of 41° . The puckering angle is defined as the angle between the (protonated) carbonyl and plane made by the α carbons. The pyramidalisation is at the expense of θ_{tor} , which decreases with respect to the vacuum MECI. This is caused by the steric restrictions of the surrounding molecules, meaning CI_{ROT} can no longer be accessed and the pyramidalised conical intersection

Table 6.4: Relative energies for the FC, E* and K* minima, and MECI on the PES for **1** and **5** for the **M7** and **M15** models, with ME and EE during the optimisation. All values presented in eV relative to the corresponding ground state and are calculated at ONIOM(ω B97X-D/6-31G(d)):AMBER level of theory. The oscillator strength f is also given.

Mechanical Embedding (ME)									
Compound 1									
		FC	E*min	K*min	MECI				
M15	S ₀	0.00	0.18	0.82	4.02	0.00	-	0.82	3.71
	S ₁	3.74	3.56	3.32	4.03	3.60	-	3.07	3.71
	f	1.150	1.207	0.503	-	0.749	-	0.475	-

M7	S ₀	0.00	0.18	0.84	3.93	0.00	-	0.80	4.05
	S ₁	3.73	3.56	3.32	3.93	3.60	-	3.06	4.06
	f	1.511	1.204	0.563	-	0.744	-	0.484	-
Electrostatic Embedding (EE)									
Compound 1									
		FC	E*min	K*min	MECI				
M15	S ₀	0.00	0.10	0.59	3.93	0.00	-	0.84	3.47
	S ₁	3.41	3.31	3.25	3.93	3.49	-	3.04	3.48
	f	1.202	1.253	0.928	-	0.926	-	0.487	-

M7	S ₀	0.00	0.08	0.48	4.04	0.00	-	0.88	3.48
	S ₁	3.32	3.23	3.20	4.05	3.50	-	3.05	3.49
	f	0.664	1.232	1.146	-	0.815	-	0.459	-

becomes the MECI. For **5**, the K* MECI has similar geometric parameters as **1**, but with a smaller pyramidalisation of the carbonyl group (21°). Interestingly, a similar CI_{PYR} conical intersection can be found in vacuum for both compounds, (Figure 6.10), with the CI_{PYR} lying 0.9 eV above the CI_{ROT} for **1** and 0.6 eV for **5**. Therefore, the crystal changes the order stability of the conical intersection manifold, stabilising CI_{PYR} over CI_{ROT} compared to in vacuum. In vacuum, CI_{PYR} is energetically accessible in both **1** and **5**, lying 0.04 below the S₁ state for **1**. For **5**, CI_{PYR} lies 0.33 eV below the initial excitation energy in vacuum. CI_{ROT} in vacuum is also accessed at lower rotational distortion and lower energy than the corresponding CI for **1**. As such, since the accessibility of the conical intersection for **5** is witnessed in vacuum, the larger stability of the MECI in the solid state compared to **1** is mainly explained by the electronic effects provided by the methoxy substituent, aided by the electrostatic potential discussed above. As a result, **5** has enough energy to deactivate through the conical intersection and return to the ground state via the nonradiative pathway, a channel infeasible for compound **1**.

Table 6.5: Comparison of MECI angle parameters for **1** and **5** in vacuum and the solid state

	Compound 1		Compound 5	
	θ_{puck}	θ_{tor}	θ_{puck}	θ_{tor}
Vacuum CI _{ROT}	8°	89°	5°	90°
Vacuum CI _{PYR}	65°	36°	62°	27°
Solid (sD) CI _{ROT}	65°	41°	67°	21°

6.4 Summary and Conclusions

In summary, the analysis of two materials with contrasting emissive properties illustrates how the balance of intermolecular and intramolecular factors can control the radiative and nonradiative mechanisms underlying their light response. To directly answer the questions at the start of the Chapter, we have shown that the AIE behaviour of compound **1** can be interpreted through the RACI model. A previously accessible conical intersection in vacuum is too high in energy to be classically populated in the solid state, due to the electrostatic and steric restrictions from the surrounding molecules. In contrast, in compound **5** the conical intersection is low enough in energy to be populated and the system can return nonradiatively to the ground state.

The relaxation mechanisms for **1** and **5** shown in Figures 6.11 and 6.12. After initial photoabsorption the excited state is delocalised in the enol form, where π - π interactions in **5** increase the excitonic coupling, which plays a role at the Franck-Condon state where absorption is delocalised. In the next chapter, the delocalisation of the exciton in the enol channel shall be scrutinised. The systems relax in E^* , where a minimum exists on the PES and emission with very small Stokes shift is possible, but self-absorption would most likely be witnessed. Nonradiative decay through a conical intersection in the enol channel is unlikely due to its high energy.

Alternatively, localisation allows ESIPT, followed by relaxation. For **1**, the nearest MECI in the K^* channel is classically inaccessible and so fluorescence is witnessed. For **5**, the MECI is lower in energy, due to the difference in electronic density distribution in S_1 on account of the methoxy group, and the wavepacket can funnel nonradiatively to S_0 . For the K^* channel, the crystal changes the relative energy of two conical intersections present in gas phase, stabilising a structure where the carbonyl group pyramidalises. The calculations show that either nonradiative delocalised transport processes (E^* channel) or localised deactivation through the ESIPT (K^* channel) are more likely in **5** than in **1**. The interplay of all discussed factors results in an enhance

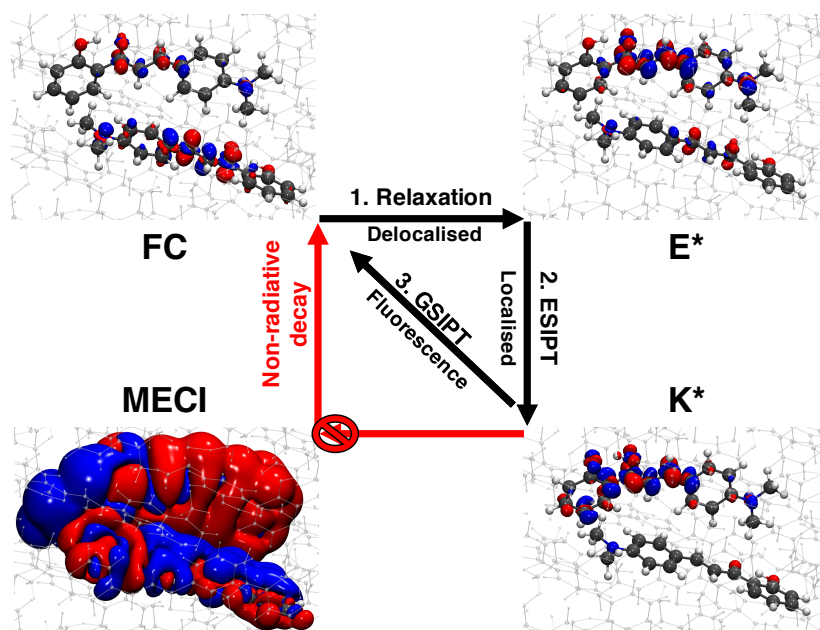


Figure 6.11: The mechanism for nonradiative decay in compound **2**. Also shown are S_1 - S_0 electron density differences (red: S_1 , blue: S_0).

emissive response of **1** and no fluorescence in **5** in the solid state.

From these results, some design principles can be proposed for more efficient solid-state emitters. As strong electrostatic interactions aid the deactivation through nonradiative pathways, it is clear why many of the reported AIE fluorophores are nonpolar. For the ESIPT chromophores, stabilising E^* over K^* minima could be favourable because the E^* nonradiative pathway through a conical intersection is hampered in the solid state. For this, the nature of the E^* state must be altered to induce a larger Stokes shift. Alternatively, if the E^* state is made more unstable by increasing the lability of the transferring proton, the population transfer to the K^* channel will increase. To maximise returns, access to the pyramidal K^* MECI can be further hindered by imposing geometrical restrictions, such as introducing fused rings to the molecular structure. Other studies in ESIPT systems have shown that torsional restraint can also be achieved by coordination to metals.²⁷⁵ For the K^* channel, efficient localisation of excited state to one monomer, bias for K^* over E^* decay and an energetically inaccessible conical intersection are all highly desirable. Indeed path agnosticity for compound **1**, which is evenly distributed for E^* and K^* , may prevent efficient transfer to the emissive K^* state. This is remedied in **5** by the bias for ESIPT but the low-lying MECI prevents fluorescence. The design of a chromophore to combine the K^* bias of

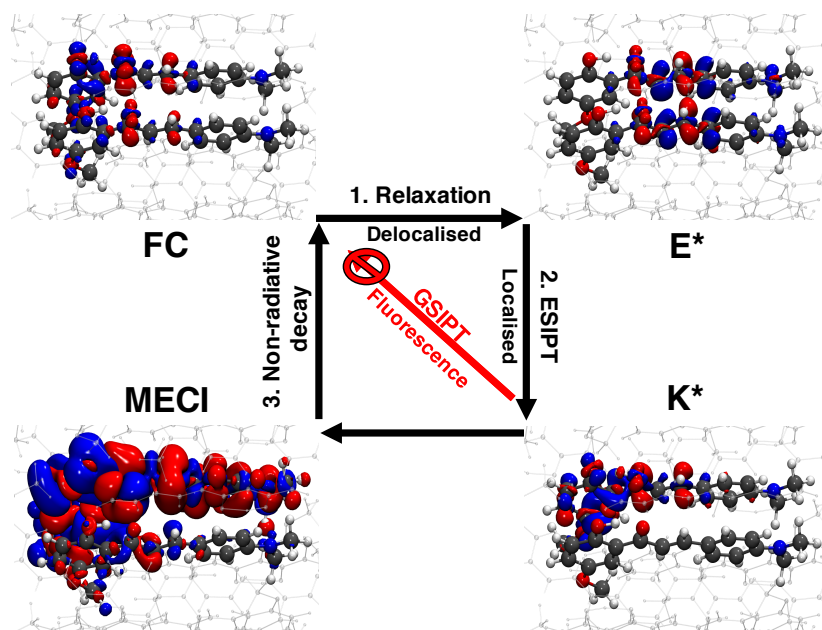
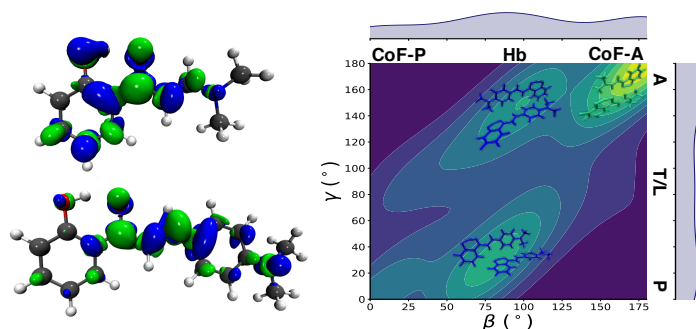


Figure 6.12: The mechanism for nonradiative decay in compound **5**. Also shown are S_1 - S_0 electron density differences (red: S_1 , blue: S_0).

5 with the stability of **1** would surely be a promising candidate for a highly efficient fluorophore. In the next chapter a new class of AIE system based on the **HC** family shall be introduced and investigated, building on the conclusions of Chapters 5 and 6 for fluorophore design.

7 Connecting Chromophore Design with Crystal Morphology



7.1 Introduction

In Chapters 5 and 6 the PESs of a range of **HC** derivatives were mapped, first in vacuum and then crystalline form. Through the topology of the PESs and the associated energy differences between states, we elucidated the AIE mechanism of **HC1** and the nonemission of **HC5**. In doing so, we isolated three key design principles to increase the quantum yield of fluorescence for ESIPT chromophores in the solid state:

1. bias for K^* decay over E^*
2. localisation of excited state to one monomer
3. an energetically inaccessible conical intersection

In this Chapter the scope of the study is extended as these design rules are applied to a new set of ESIPT systems. To the test set we add two fluorine-substituted **HC** derivatives, **HC6** and **HC7**.¹⁸³ Additionally, four completely new compounds with lasing properties are considered. Closely related to **HCs** are the family of **HP** derivatives.¹⁸⁴ In contrast to **HCs**, and other organic fluorophores, **HP** compounds contain only a single aryl group and have remarkable Φ_{PL} , ranging

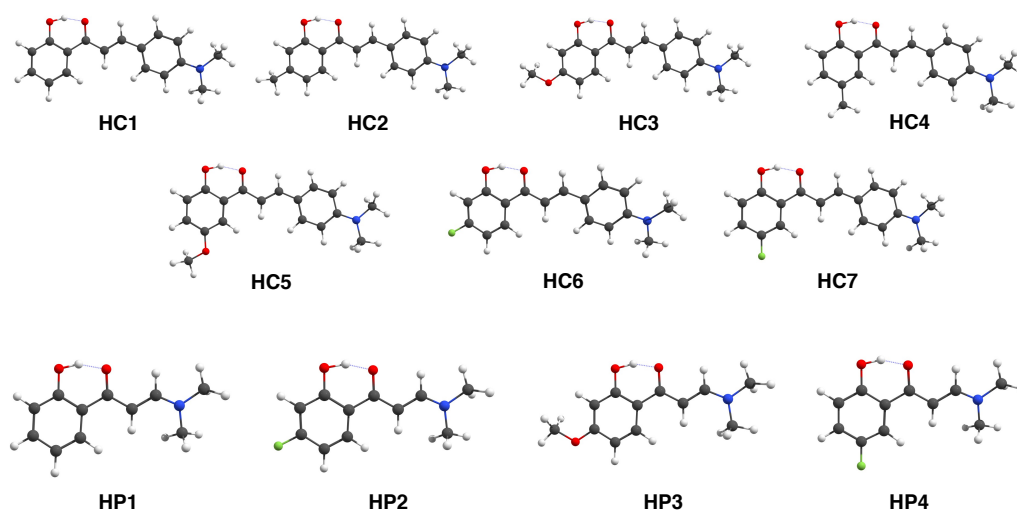


Figure 7.1: The molecular structure of the seven **HC** and four **HP** compounds under investigation.

from 0.72-0.84. This has been qualitatively attributed experimentally to the herringbone packing mode and molecular rigidity reducing nonradiative decay. The increased quantum yield of the **HPs**, with respect to the **HCs**, make them prime candidates to test the efficacy of our design rules. The eleven compounds studied in this Chapter are summarised in Table 3.1 and shown in Figure 7.1. Herein we investigate the factors which mediate the increased fluorescence activity for **HP** compared to **HC** systems. In the following sections we address molecular and material properties of the eleven compounds to investigate why the **HPs** systems have an increased Φ_{PL} compared to their **HC** counterparts. We will show how a combination of electronic properties and crystal packing give the **HP** systems an increased potency for each of the three design rules, resulting in increased fluorescence in the solid state. Particular focus will be given to **HC1**, **HC5**, and **HP1**, which will act as exemplar systems due to their differing fluorescence behaviour.

After outlining the computational methods used, we address the molecular properties of the **HC** systems. We map the PESs of **HP1-4** in vacuum, to locate the nonradiative decay channels and gauge the substituent effects, showing how the increased bias for the keto channel promotes ESIPT in these systems, fulfilling design rule one. We then move to the crystalline state and show how a stable K^* minimum and inaccessible conical intersection promote radiative decay in **HP1**, satisfying design rule three. We compute the radiative decay rates for **HC1**, **HC5**, and **HP1** *via* two methods to compare the exemplar compounds, and examine the Huang-Rhys factors to qualitatively assess the FGR-RIM interpretation for nonradiative decay.

We then turn our attention to the intermolecular properties of the eleven molecular crystals. The crystal structures are analysed with particular attention paid to the dimer configurations present. We examine how the dimer arrangements mediate the excitonic coupling between molecular sites in the crystal and afford localisation of the excited state. Following this, an exciton hopping model based on Marcus Theory is applied to examine the different hopping rates in the enol state and examine the competition between localisation and exciton diffusion, and how the **HP** systems show greater charge localisation to fulfil the second design rule. All calculations and analyses were performed by myself except for the implementation of the Voronoi cells, which was done by Miguel Rivera, and the TDDFT optimisations in vacuum of **HP1-4**, which were carried out by Matthew Hollis-Smith. At the time of writing, a manuscript based on this chapter is in the final stages of preparation for publication.

7.2 Computational Details

Crystal structures of compounds **HC1-7** and **HP1-4** were obtained from the CCDC as described in references 182–184. **HP1-4** were optimised in vacuum in the S_0 and S_1 enol and keto states at the (TD-) ω B97X-D/6-311++G(d,p) level of theory. Conical intersections were optimised at the same level of theory using CIOpt.¹⁹ Relaxed geometry scans of the torsional rotation angle θ_{tor} in the keto S_1 state (K^*) were performed for the same compounds. Proton migration scans of the ES IPT process were also performed in vacuum for **HC1**, **HC5** and **HP1**. All scans were calculated at TD- ω B97X-D/6-31G(d).

Crystal structures of all **HC** and **HP** compounds were optimised using Quantum Espresso in the periodic DFT framework.²⁶⁸ Optimisation of each unit cell was carried out with DFT-D2 (PBE) with a plane-wave cutoff of 30 Ry and ensuring Monkhorst-Pack k-point convergence in each case. As the exemplar parent **HP** compound, the full excited state decay mechanism of **HP1** was established through QM:MM cluster models using density functional and multireference methods. A monomer and trimer chromophore at the centroid of the 20Å cluster were optimised in the ground and excited states at ONIOM((TD-) ω B97X-D/6-31G(d):AMBER) level of theory. The S_1/S_0 MECI in both monomer and trimer cluster models were calculated using a modified version of the CIOpt algorithm.¹⁹

For **HP1** MECI in the monomer cluster models was also obtained with the state-averaged com-

plete active space self-consistent field method, employing the S_0 and S_1 states in the averaging, as in Chapter 6.. The active space consisted of 12 electrons in 11 orbitals (SA-2-CASSCF(12,11)). The 6-31G(d) basis set was using for the QM region and the AMBER force field was used to describe the MM region. The potential energy profile was refined with multistate complete active space second-order perturbation theory (MS-3-CASPT2(12,11)/6-31G(d):AMBER), incorporating the S_0 , S_1 , and S_2 states. The TD-DFT:MM geometries from the trimer models at the Franck-Condon, S_1 minimum, and MECI were taken as the reference geometries, where the central molecule was taken for the CASPT2 calculation and the remaining two molecules of the trimer were added to the MM region. A three state average was used. The orbitals chosen for the active space are shown in Appendix D.

Crystalline emission spectra for **HC1**, **HC5** and **HP1** in E^* and K^* minima were simulated using the nuclear ensemble method as implemented in the NEWTON-X software suite.²⁶² 100 initial conditions were sampled from the harmonic frequencies calculated at ONIOM(TD- ω B97X-D/6-31G(d)):AMBER level from 7Å cluster models. The S_1 - S_0 energy gap was computed for each initial condition in embedded point charges to reflect the positions of the MM charges. No MM-level energies were computed, and as such the fluorescence spectra are of only the electronic energies.

To calculate solid state reorganisation energies in the adiabatic approximation (λ_A , Equation 3.10) for each compound we generated cluster models based on the 2x2x2 supercell, where all molecules which lay within 20Å of the central monomer chromophore were included in the cluster. Geometries were optimised for all eleven clusters in S_1 and S_0 states within the ONIOM protocol at ω B97X-D/6-31G(d):UFF using electrostatic embedding. MM charges were derived automatically using the QEq method.⁷⁹ The UFF force field was chosen here due to the automatic charge assignment, allowing the highthroughput generation of structures and input files. In the cases of **HC1-4** and **HC6-7**, λ_A was calculated for both enol and keto pathways. For **HC5** and **HP1-4**, only the λ_A associated with keto relaxation was used since no E^* minimum was located in the monomer QM:MM relaxation. Reorganisation energies in the normal-mode approximation (λ_{NM}) were calculated using the DUSHIN program for **HC1**, **HC5** and **HP1**.¹³¹ Frequencies for an ONIOM-optimised monomer chromophore were calculated in an array of point charges representing the molecular crystal, at TD- ω B97X-D/6-31G(d) level. This lead to one imaginary frequency in each case.

Exciton couplings J were calculated for dimers in each optimised crystal structure. A 2x2x2 supercell was constructed for each system and a dimer was defined as any molecular pair with an interatomic distance less than or equal to the van der Waals radii of the atoms, plus a damping factor of 1.5Å. This selection criterion has previously been used in similar applications.²⁷⁶

To analyse the spatial environment for the monomers at the centre of the cluster models in the each crystal, Voronoi cells partition the crystal into molecular regions. These cells define all the points in space which are closer to the reference molecule than an exterior molecule. Dividing the Voronoi cell volume by the van der Waals volume gives a molecule-independent Voronoi index V_i for each crystal structure. To generate the Voronoi cells, a cluster of molecules was extracted from its crystalline positions. A real space grid was generated at an arbitrary resolution and at each point of this grid, the distance to each atom was calculated and scaled by the corresponding van der Waals radius. All voxels with the lowest scaled distance belonging to an atom of the central molecule were marked as belonging to the accessible of the molecule, resulting in an irregular polyhedron of finite volume.

All density functional calculations were performed in the Gaussian 09 suite of programs.²⁷⁰ CASSCF and CASPT2 calculations used OpenMolcas with the Tinker v.6.3.3 interface.²⁷¹

7.3 Results

7.3.1 Potential Energy Surfaces of HP Derivatives in Vacuum

The 2-hydroxyphenylpropanone (**HP**) compounds synthesised by Tang *et al.* show remarkable AIE behaviour. Before studying the root of their fluorescence in the solid state, in this section the PESs are mapped in vacuum at (TD-)DFT level. This enables the isolation of the substituent effect and to understand the effect of removing an aryl ring from the **HC** structure.

In Figure 7.2, the energy levels of the key regions of the PES are shown for **HP1-4**. Vertical excitation to S_1 in vacuum is predicted at 4.16 eV for **HP1**, a blue shift of 0.51 eV compared to **HC1**. There is a blue shift of 0.09 eV for **HP2** and a red shift of 0.18 for **HP4** compared to **HP1**. These excitations are all bright and HOMO-LUMO in character. The difference density plots show that density is lost from the phenol oxygen and donated to the C=O carbonyl, as for S_1 in **HC5** (Figure 7.3). Results from Chapter 5 show that this electronic structure promotes ESIPT.

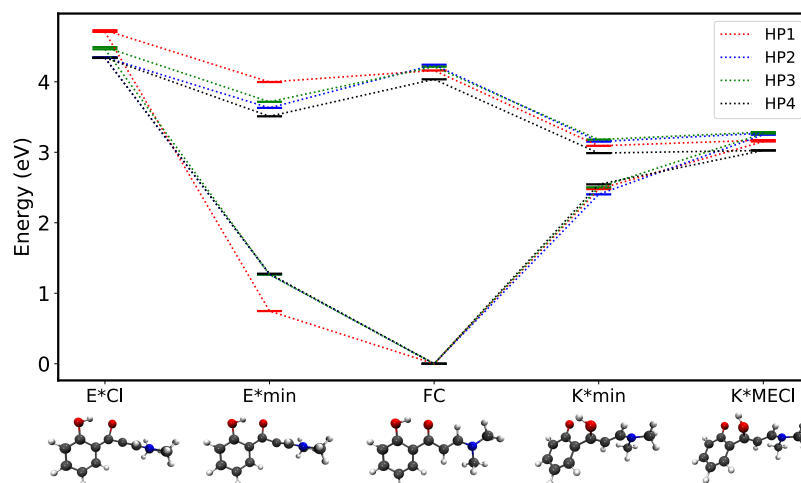


Figure 7.2: The critical points on the PES for **HP1-4** obtained at (TD-) ω BX-D/6-311++G(d,p) in vacuum. Also shown are the optimised geometries at each point for **HP1**.

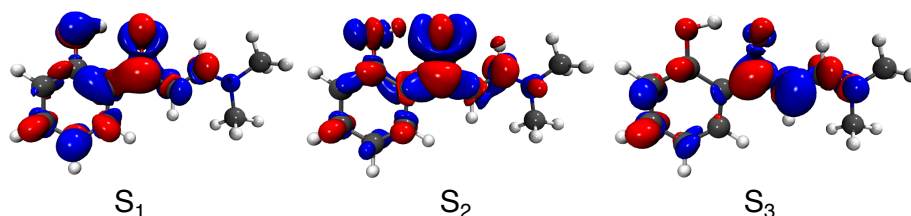


Figure 7.3: Electron density difference maps for the first three excitations of **HP1**. Blue regions represent electron density loss from the ground state and red represent electron density gain in the excited state, with isovalue of 0.002. Calculated at TD- ω B97X-D/6-311++G(d,p) in vacuum.

In **HP2** and **HP3**, there is some donation from the amino N. In **4**, electron density is lost from the fluorine.

The experimental absorption in DCM is centred at 3.43 eV for **1**, and thus the TDDFT excitation energies are largely overestimated. When a solvent cavity is introduced through the polarizable continuum model (PCM), the S_1 energy is red shifted to 4.01 eV - an improvement but still largely overestimated compared to experiment. Another RSH functional, CAM-B3LYP,²⁷⁷ performs little better, with the bright state at 3.98 eV. It is for this reason that in the solid state calculations in Section 7.3.3, the CASPT2 method is applied to determine the energetic pathways.

In the enol channel relaxation is not *via* rotation about θ_{tor} , instead occurring through partial cis-trans isomerisation about the carbon-carbon double bond. Fluorescence from this state is

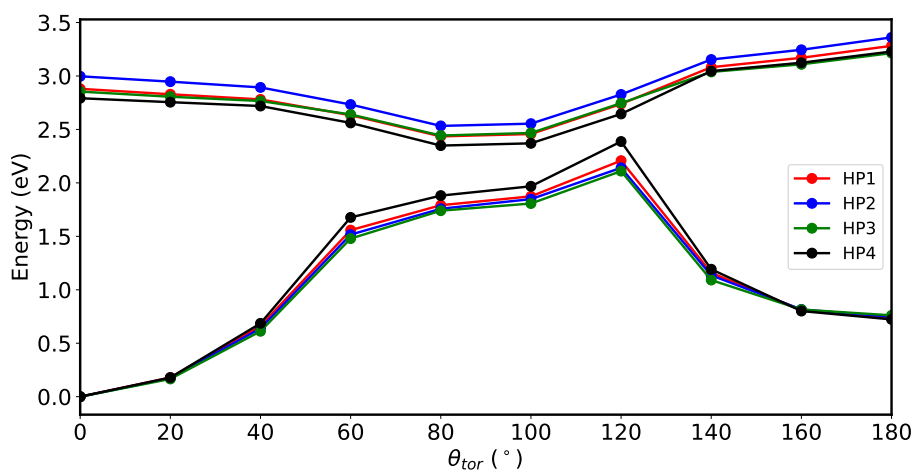


Figure 7.4: Relaxed geometry scan of θ_{tor} for **HP1-4**, calculated at TD- ω B97X-D/6-31G(d) level of theory in vacuum.

dipole forbidden with negligible oscillator strength. The conical intersection on the enol channel is inaccessible, with a distortion of the carbonyl group.

The relative energetic stability of the keto channel is expected to result in a large bias and high population of K^* . As for the **HC** systems, relaxation is *via* rotation about θ_{tor} (defined in Figure 7.6) and is heavily favoured, as shown by the relaxed geometry scan of θ_{tor} in Figure 7.4. There is destabilisation of the ground state through the rotation but the keto state remains stable through 180°. We shall return to this concept in Section 7.3.2. Full isomerisation is not expected due to the high energy of the trans-keto state in both S_1 and S_0 compared to the cis-keto conformer. The conical intersection is energetically accessible in vacuum, with the substituent effects relatively minor. This is to be expected, since experimental results show that both absorption and emission energies show only minor (< 0.15 eV) substituent dependence.

7.3.2 HP Bias for ESIPT

In this section, it is shown that the K^* population is enhanced by the inherent bias for ESIPT in the **HPs** compared to the **HCs**. The electronic densities show that in the bright excitation of **HC1**, electron density is mainly donated from the unsaturated bridge and the dimethylaniline moiety (Figure 7.3). In contrast, in **HC5** and to a greater extent **HP1** (due the removal of the second aryl group), electron density is decreased at the phenol oxygen in the excited state (Figure 5.1). NBO

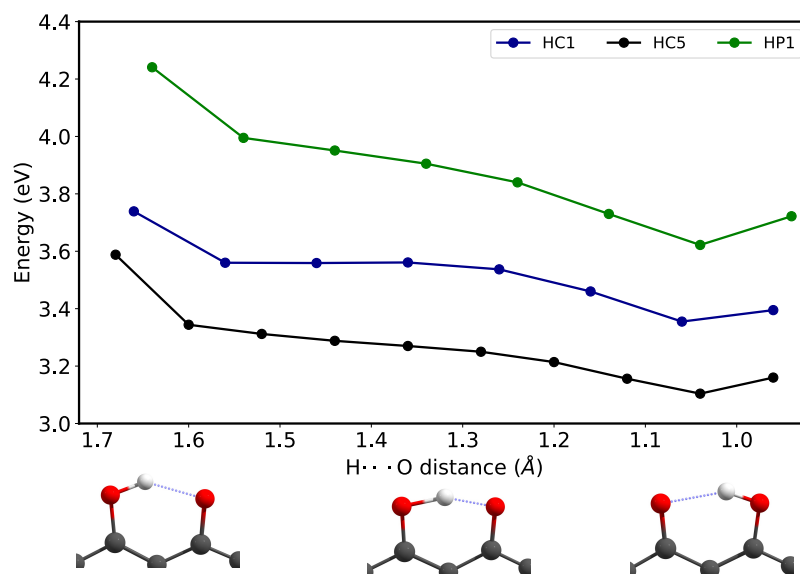


Figure 7.5: Relaxed geometry scan of the phenol hydrogen to carbonyl oxygen distance for **HC1**, **HC5** and **HP1**, calculated at TD- ω B87X-D/6-31G(d).

charge analysis of the phenol oxygen shows that Δq increases from +0.01 to +0.05 to +0.09 for **HC1**, **HC5** and **HP1** respectively. This increases the bias for ESIPT in **HC5** and **HP1** due to the increased acidity of the transferring proton, as shown by the excited state PES relaxed geometry scan in Figure 7.5. **HP1** shows a stabilisation of 0.62 eV, compared to 0.48 eV for **HC5** and 0.38 for **HC1**.

In the K^* channel in vacuum, relaxed geometry scans along the torsional relaxation mode (Figure 7.6) show that for **HC5**, the onset of the conical intersection seam is reached at 60° , due to the overload of electronic density at the protonated carbonyl group. Contrastingly in **HP** systems, the conical intersection seam is not found along torsional relaxation mode. While the electronic density distribution in **HP** systems leads to a strong bias for ESIPT, as for **HC5**, it does not destabilise the ground state during rotation to the same extent. **HP** systems are thus inherently more stable in the K^* channel. However, for all **HC** and **HP** systems, the MECI in non-aggregated form is energetically accessible post photoexcitation and thus nonradiative decay is witnessed experimentally. The proton lability in the **HP** systems, on account of electron density distribution, and the stability of the K^* minimum, means they obey design rule one more strictly than in the **HC** systems.

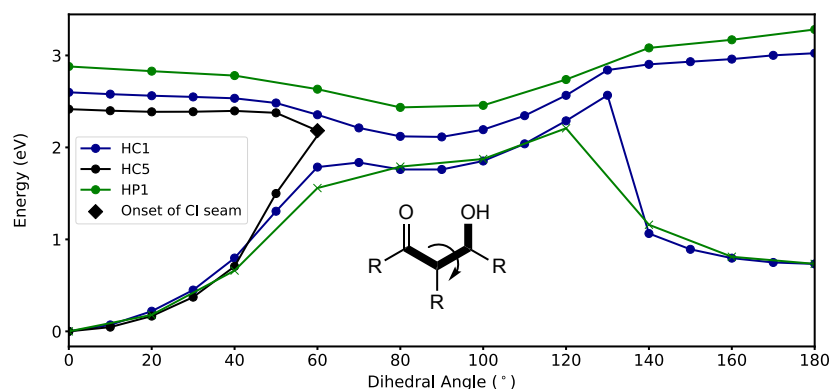


Figure 7.6: Relaxed geometry scan of the torsional angle (shown inset, θ_{tor}) for **HC1**, **HC5** and **HP1** in vacuum, calculated at TD- ω B87X-D/6-31G(d). For **HC5**, the scan cannot proceed further than 60° due to the convergence of the two electronic states.

7.3.3 Relaxation Pathways in the Molecular Crystal

Results from Chapter 6 showed that efficient population transfer to the K^* tautomer is only one prerequisite for fluorescence. The accessibility of the nearest conical intersection can dictate the luminescent response. For **HC1**, fluorescence is possible due to the high energy conical intersection in the solid state. On the other hand, for **HC5**, whilst ES IPT is more efficient than in **HC1**, the Φ_{PL} is essentially zero and AIE is not seen. This can be attributed to dominance of nonradiative decay as a result of a low-lying MECI being classically accessible post electronic excitation. While intermolecular factors play a role in the conformation of the MECI, the energetic accessibility is determined by the electronic structure of the chromophore. To assess the accessibility of the MECI in the solid-state in **HP1**, we construct the excitation-decay pathway in the using QM:MM cluster models. The calculated PES for **HP1** in vacuum and the solid state is shown in Figure 7.7. Geometries were optimised at the Franck-Condon, the K^* minimum and the MECI with (TD-) ω B97X-D/6-31+G(d):AMBER using a trimer chromophore. The central monomer, where ES IPT and the MECI occur, was then used as the chromophore in MS-3-CASPT2(12,11)/6-31G(d):AMBER single point calculations, with the two other members of the trimer demoted to the MM-level. This eased the computational expense in the MS-3-CASPT2(12,11):AMBER calculations, which are necessary to accurately predict the energy of the S_1 excitation in the solid state. The MECI geometry obtained with the trimer with TD-DFT compares well with the geometry obtained at MS-2-CASSCF(12,11):AMBER, with an RMSD of 0.08(9) Å. With the

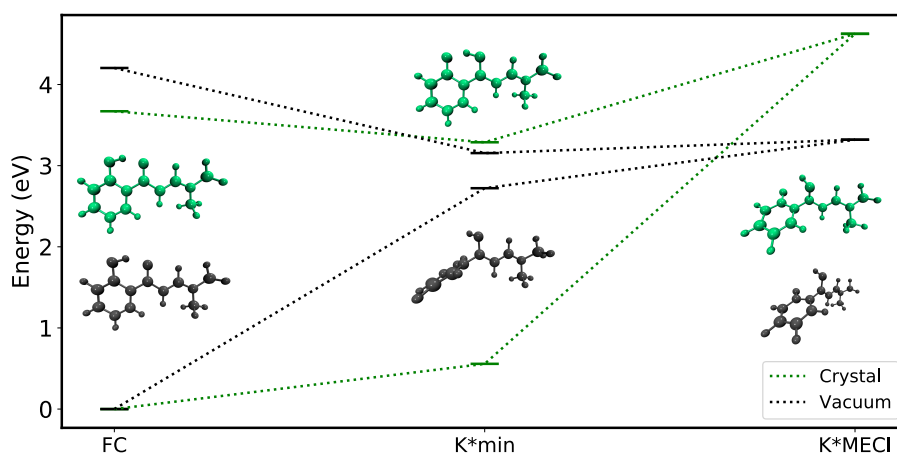


Figure 7.7: Calculated energies and geometries at critical points on PES. Geometries obtained with (TD)- ω B97X-D/6-31G(d):(AMBER), with energies calculated at MS-3-CASPT2(12,11):(AMBER). The average energy of the S_1 and S_0 states is shown for the MECI.

monomer model, the RMSD is 0.09(2) Å .

At the MS-3-CASPT2(12,11)/6-31G(d):AMBER level, absorption for **HP1** is calculated at 3.67 eV ($f=0.868$), in fair agreement but blue-shifted by 0.41 eV compared with the crystalline absorption maximum of 3.26 eV.¹⁸⁴ With a four-state average (MS-4-CASPT2), this improves further to 3.52 eV. With TD- ω B97X-D/6-31G(d):AMBER, the bright state is calculated at 4.25 eV in the trimer model and 4.23 eV in the monomer model, a large overestimation of the absorption energy. When the 6-311++G(d,p) basis set is used, the prediction is slightly improved with the bright state occurring at 4.10 eV. With TD-CAM-B3LYP/6-31G(d):AMBER, the bright state is 4.20 eV. The accurate prediction of the initial photoabsorption is crucial in understanding the excited state mechanism and as such we proceed with using MS-3-CASPT2(12,11)/6-31G(d):AMBER for the energies (which is denoted CASPT2 for brevity).

Post photo-excitation, relaxation in S_1 via ESIPT is expected to be dominant relaxation channel in **HP1** due to the negligible oscillator strength ($f=0.016$) of the S_2 state, which is $n\pi^*$ in character. Fluorescence in the molecular crystal is centred at 2.34 eV, thus displaying a Stokes shift of 0.94 eV. The emission wavelength predicted at CASPT2 is 2.73 eV, again in fair agreement and with similar blue-shift as calculated for absorption. Certainly, allowing relaxation of the exterior atoms and mutual polarisation would allow further geometric relaxation and a more accurate emission energy. Also, addition of Ewald point charges to reflect the periodicity of the

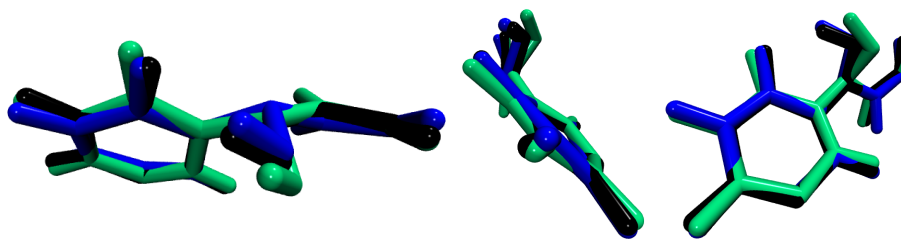


Figure 7.8: Overlaid structures of the MECI for **HC1** (blue) and **HC5** (black), and **HP1** (green), shown from three viewpoints. Only the atoms shared by all three compounds are shown.

crystal would improve emission further. However, this was outside the scope of the current work.

The MECI in **HP1** lies 1.46 eV above the K^* minimum and 1.08 eV above the bright absorption state. As such, it is classically inaccessible and **HP** emission can be attributed to the trapping of the excited state at the K^* minimum, followed by radiative decay. The degeneracy of the S_1 and S_0 states on going from CASSCF to CASPT2 is lifted slightly, with a gap of 0.2 eV at CASPT2 level. As the substituent effects in the crystalline samples are minor in the **HP** samples (absorption and fluorescence), it can be assumed that this mechanism can be applied to all four systems in the family. It would be of interest to synthesise a **HP** system with a methoxy group the *para* position, as in **HC5**, to assess its AIE behaviour.

In Figure 7.8, the MECI geometries of **HC1**, **HC5**, and **HP1** are compared. All three involve the pyramidalisation of the protonated carbonyl group combined with torsional rotation of the deprotonated phenol moiety. In **HC1** and **HP1**, the compounds which undergo AIE due to the high energy of the MECI, the torsional angles are 50° and 53° respectively. In **HC5**, where the MECI is energetically accessible, the pyramidal distortion is only 28° . The same effect is seen in vacuum, where the MECI of **HC5** is also onset at lesser distortion than the other systems, as discussed above. Thus the stability of the **HC5**, and the high energy MECIs of **HC1** and **HP1**, are mainly due to the electronic effects of the chromophore. Rather, the role of the packing and the crystalline environment as a whole is to promote efficient localisation of the excited state at the expense of exciton hopping the enol state, as will be investigated in Section 7.3.8. Such is the propensity for localisation and ESIPT in **HP** and the high energy MECI, a largely increased Φ_{PL} is witnessed as a result, fulfilling design rules two and three.

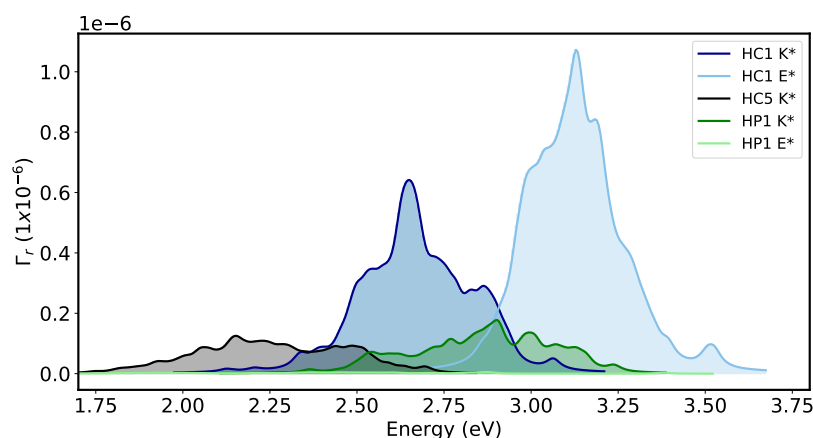


Figure 7.9: Emission spectra in molecular crystal for 7 Å clusters for **HC1**, **HC5** and **HP1**, calculated at TD- ω B97X-D/6-31G(d) in point charges. Single point energies were calculated for 100 initial conditions based upon a Wigner distribution of the excited state frequencies calculated at ONIOM(TD- ω B97X-D/6-31G(d):AMBER) level.

7.3.4 Radiative Decay Rates

In this section we calculate the emission rate k_r for **HC1**, **HC5**, and **HP1**. This can be done either through the Einstein spontaneous emission relationship (Equation 3.2) or through integrating the simulated spectrum (Equation 3.3). The oscillator strength between S_1 and S_0 states at the K^* minimum is 0.549 at CASPT2 level (0.281 TDDFT trimer model, 0.331 with TDDFT monomer), indicating that emission will be bright. First, we compute the radiative decay rates from the E^* and K^* states using ONIOM(TDDFT) by computing the fluorescence spectrum and calculating k_r through Equation 3.3. The spectra for **HC1**, **HC5** and **HP1** are given in Figure 7.9 and radiative rates for **HC1**, **HC5** and **HP1** are given in Table 7.1.

For **HC1**, k_{r,K^*} is comparable with **HP1** in both E^* and K^* . However, **HC1** exhibits lower quantum efficiency, owing to the competing exciton hopping in the enol state, which will inhibit localisation and thus ESIPT. Thus in **HC1** there is competition between delocalisation, emission from E^* , and emission from K^* . Due to the proximity of the E^* band to the absorption, only K^* fluorescence will significantly contribute to the quantum yield.

For **HP1**, emission from E^* is negligible and emission is expected from the K^* state. The highly distorted E^* minimum, is expected to play little role in the photochemistry and population transfer to K^* should dominate. The radiative rate from K^* is of similar magnitude to **HC1**, and

Table 7.1: Radiative decay rates k_r in the solid state in the enol (E^*) and keto (K^*) regimes for **HC1**, **HC5**, **HP1** calculated through spectral integration. In parenthesis is the rate calculated *via* the Einstein relationship of Equation 3.2. All rates in s^{-1} .

System	k_{r,E^*}	k_{r,K^*}
HC1	4.68×10^8 (1.78×10^9)	2.99×10^8 (2.83×10^8)
HC5	-	9.54×10^7 (1.02×10^8)
HP1	5.58×10^6 (4.49×10^6)	1.10×10^8 (1.23×10^8)

as such the higher quantum yield of **HP1** is on account of the lower nonradiative decay rate and lack of other competitive pathways, such as exciton hopping. In Table 7.1, given in parenthesis are the rates obtained from the more simple Einstein relationship. This method compares well to the more complex spectral method, where the Wigner distribution of geometries based on harmonic frequencies should provide a more realistic radiative rate. Based on these rates the Einstein relationship can provide a qualitative estimate for k_r without the need for computing the fluorescence spectrum, which is a far more computationally demanding approach. However, that is most likely due to the fact that in these systems, the steric hindrance of the molecular crystal means there is little geometric relaxation and the excited state PES resembles the ground state PES, since there is not the steric freedom to explore outside of the harmonic potential.

7.3.5 Huang-Rhys Factors

As discussed in Section 3.2.2, reorganisation energies and Huang-Rhys (HR) factors are often used to qualitatively account for the FGR-RIM interpretation of AIE. In this section we address this model for the **HC** and **HP** systems. The HR factors in vacuum and molecular crystals were calculated for **HC1**, **HC5**, and **HP1**. In vacuum, ground and excited states were optimised at (TD-) ω B97X-d/6-31G(d) level. In the molecular crystal, a cluster model consisting of a central chromophore and all molecules within a 7\AA , taken from the optimised unit cell for each system. Ground and excited states were optimised at ONIOM((TD-) ω B97X-d/6-31G(d):AMBER) level, and frequencies were calculated at (TD-) ω B97X-d/6-31G(d) level using point charge embedding. The DUSHIN program was used to calculate the Huang-Rhys factors and the associated reorganisation energies (λ_{NM}).¹³¹

For **HP1** and **HC5**, it is found that λ_{NM} overestimates the reorganisation energy with respect to λ_A . In **HP1**, λ_A is 1.24 eV compared to 2.19 eV for λ_{NM} . In **HC5**, the NM approximation is 0.4 eV larger than λ_A . In both **HP1** and **HC5**, the HR factors are reduced in moving from

vacuum to the solid state, in particular for rotational modes. The RIM interpretation of AIE prescribes that switch-on of fluorescence upon aggregation is due to dampening of rotational modes, which dissipate the excited state nonradiatively, as witnessed by a reduction in the HR factors. While **HC1**, **HC5** and **HP1** show this effect, **HC1** and **HP1** show AIE while **HC5** is dark in both dispersed and aggregated forms. The dampening of the HR factors does not result in luminescence in **HC5**, suggesting that the excited state wavepacket decays through the MECI.²⁵³ Furthermore, due to the anharmonicity of the PES, the validity of the scheme in these cases is not clear. To explore this further, Figures 7.10-7.12 show the Huang-Rhys (HR) factors in vacuum and solid state for **HC1**, **HC5** and **HP1**. The different y-axis scales for the Huang-Rhys factors between plots should be noted. Each system is discussed in turn below.

For **HC1** in vacuum (Figure 7.10, left), the geometric similarity between the planar E* excited state minimum and the ground state equilibrium geometry yields negligible HR factors. This leads to λ_{NM} of 0.08 eV, which underestimates the λ_A of 0.36. For K*, the PES in vacuum is highly anharmonic, and intramolecular rotation leads to a highly distorted geometry with respect to the ground state. As a consequence, the HR factors are extremely large and the harmonic approximation is not applicable for determining the reorganisation energy, as illustrated by a value of 99 eV ($\lambda_A=3.64$ eV). Moving to the molecular crystal (Figure 7.10, right), in E* the HR factors are of similar magnitude as in vacuum but in K* they are markedly reduced and suppressed to fractional values. The largest K* HR factor is the O-H stretching mode, since the geometry remains planar and has the largest displacement between S₀ and S₁ as it is the ES IPT coordinate. The K* λ_{NM} is 4.67 eV, with $\lambda_A=0.59$ eV.

In **HC5** there is no stable E* minimum in either vacuum or the solid state for the monomer chromophore. In vacuum, the HR factors are much less than in **HC1** due to the rotation angle at the minimum being less distorted. The molecule is more planar and is closer in structure and vibrational signature. At larger rotation angles the MECI is reached. HR factors are reduced in the solid state, in particular for the rotational modes, but with the O-H stretch HR factor increasing.

For **HP1**, large reorganisation energies, and correspondingly large HR-factors, are associated with low-frequency rotational modes. Indeed, such is the displacement between modes in the ground and excited states, the total reorganisation energy is 41 eV, whereas the adiabatic value 3.89 eV. As such, the harmonic approximation is invalid here due to the excited state potential energy surface anharmonicity. In the solid state, the normal modes associated with rotation are

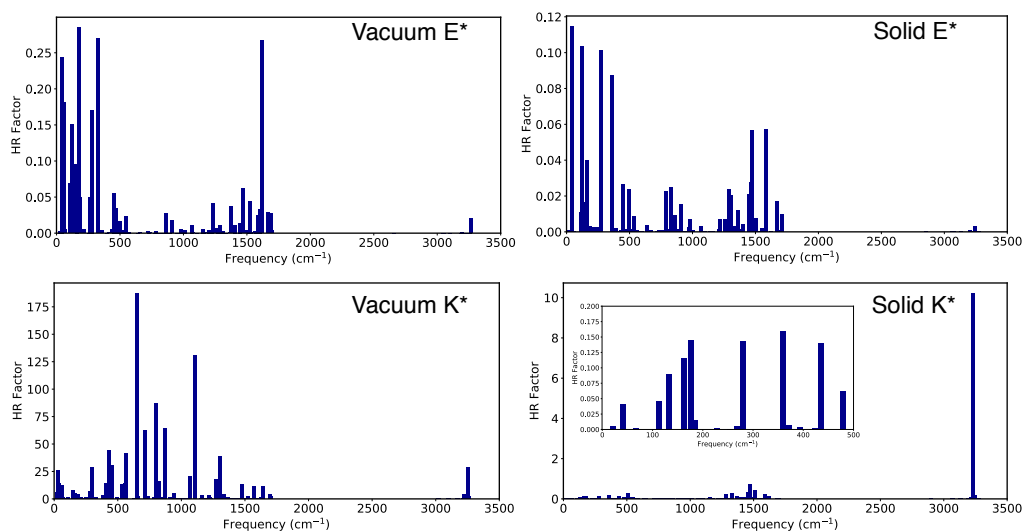


Figure 7.10: Huang-Rhys factors associated with each normal mode calculated *via* the Duschinsky rotation matrix between the E* and S₀, and K* and S₀ electronic states for **HC1**. Frequencies 0-500 cm⁻¹ in the solid state are shown in the inset.

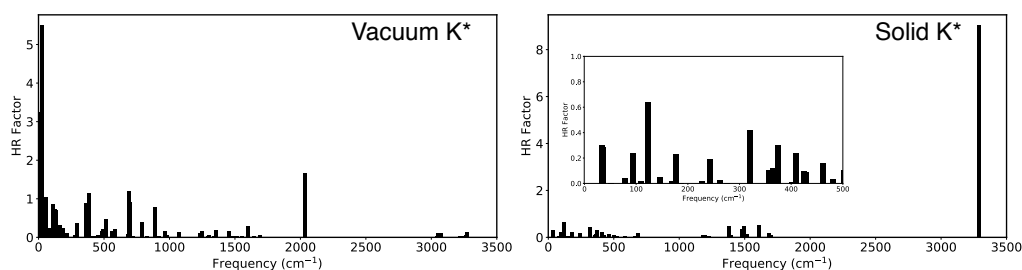


Figure 7.11: Huang-Rhys factors associated with each normal mode calculated *via* the Duschinsky rotation matrix between K* and S₀ electronic states for **HC5**. Frequencies 0-500 cm⁻¹ in the solid state are shown in the inset.

significantly reduced, whilst the largest HR factor is associated with the stretching of the phenol oxygen. This is to be expected, since it is along this coordinate that ESIPT occurs, and hence it has the largest HR-factor. In solid state, λ_{NM} is 2.19 eV, compared with λ_A of 1.24 eV.

In the case of the **HC** and **HP** systems, the AIE behaviour can not be directly attributed to the reduction of the HR factors in the solid state compared to vacuum. Such is the complexity of the PES, where ESIPT and rotation occur in the excited state (in vacuum), the surfaces are highly anharmonic and the validity of the FGR-RIM scheme is not clear. As such, it is not the focus of our investigation into the AIE behaviour of these systems.

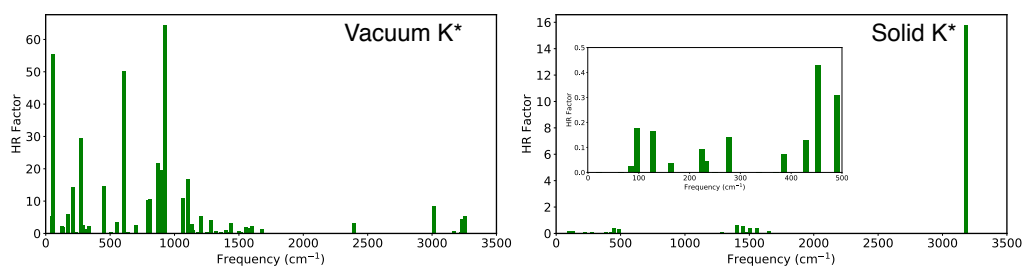


Figure 7.12: Huang-Rhys factors associated with each normal mode calculated *via* the Duschinsky rotation matrix between K^* and S_0 electronic states for **HP1**. Frequencies 0-500 cm^{-1} in the solid state are shown in the inset.

7.3.6 Analysis of Crystal Packing

In this section we use several techniques to analyse the crystal structures of the eleven compounds of Table 3.1. The crystalline environment of each crystal is examined initially from the perspective of a monomeric chromophore. To this end, we use Voronoi cell volumes V_{cell} and van der Waals volumes V_{vdW} to determine a Voronoi index $V_i = V_{cell}/V_{vdW}$, a metric indicating the normalised accessible volume for a monomer in the crystal. V_i values (Figure 7.13) range from 1.29-1.48, showing that despite the substituent and packing differences, the each monomer in the system has between 30%-50% of its van der Waals volume to freely vibrate, rotate or translate. For the **HC** systems, the average V_i is 1.36 ± 0.06 , and 1.30 ± 0.01 for the **HP** systems. The accessible volume for the **HC** systems shows greater variation but is overall slightly higher than for the less varied **HP** systems. The increased volume for the **HC** systems theoretically allow for greater nuclear relaxation in the excited state. However, reorganisation energies (Section 7.3.8) for the **HP** systems are larger than for **HC**, showing the importance of the electronic effects over geometric considerations.

Exciton transport has been occurs through hopping between molecular sites, and thus it is important to understand the possible intermolecular transport channels in the **HC** and **HP** systems.¹³² To determine the intermolecular relationships, we examine the topology of the molecular crystals of **HC** and **HP** families by considering dimer configurations. Crystal morphologies are commonly described qualitatively as herringbone, face-face, edge-tail, *etc.* Here we take a more of quantitative approach by constructing maps of each crystal, based on a geometric description of the dimers. These maps allow the topology of the crystal to be analysed graphically.

Dimers are quantified through three angle variables, α , β , and γ . These are depicted in Figure

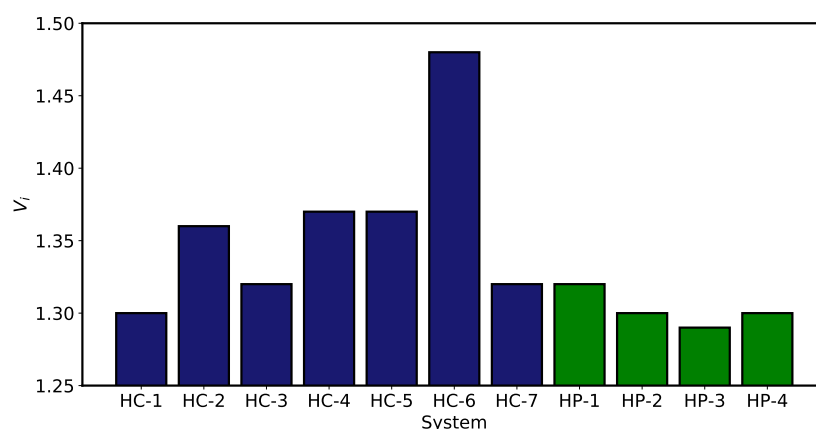


Figure 7.13: Voronoi indices for **HC** and **HP** crystal structures.

7.14, and example dimers with associated angles are given in Figure 7.15. Three axes, x , y , z , are defined on each molecule i and j of the dimer, where x and y are the long and short axes of the molecule, and z is the orthogonal vector. These vectors comprise an orthogonal basis to describe the dimer. The angles are then defined as:

- α : The azimuthal angle between the monomers shown as the black angle in Figure 7.14. Calculated as the angle between the z -axis located at the centroid of monomer i , and the vector connecting two centroids. α is calculated twice, once with each monomer as the reference. The smallest angle is chosen, such that $0^\circ \leq \alpha \leq 90^\circ$.
- β : The angle between the two short-axis vectors y of each molecule, shown in green in Figure 7.14. β ranges from 0° to 180° , tracking whether monomers are aligned cofacially parallel ($\beta = 0^\circ$, CoF-P), or cofacially antiparallel ($\beta = 180^\circ$, CoF-A), or in a herringbone edge-face manner (90° , Hb), and all configurations in between. β is commonly described as the “herringbone” angle.
- γ : The angle between the long-axis vectors x , ranging from 0° (parallel, P) to 180° (antiparallel, A). At $\gamma = 90^\circ$, the dimer is T- or L-shaped, dependent on the x -slip.

In Figure 7.14b the distribution density of the α angle is shown for the cofacially stacked **HC** and **HP** systems. The distribution is heavily skewed towards 90° , indicating that for the majority of cofacial dimers, there is little overlap between the centroids of the monomers. As such, it can be expected that in each molecular crystal there are few dimers with the configuration required

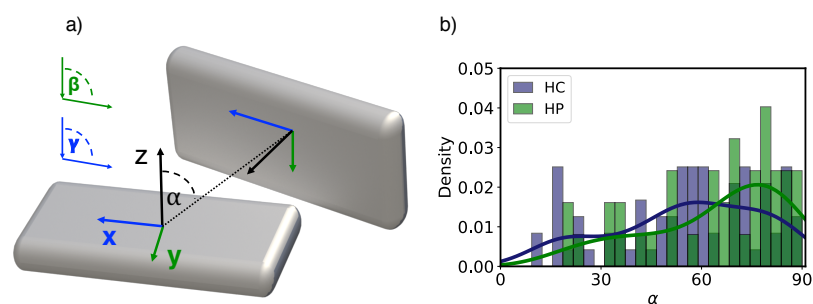


Figure 7.14: Panel a), left; schematic of two monomers, and the α , β , and γ angles used to classify dimer configurations. Panel b), right; distribution of α angles for dimers in **HC** and **HP** systems.

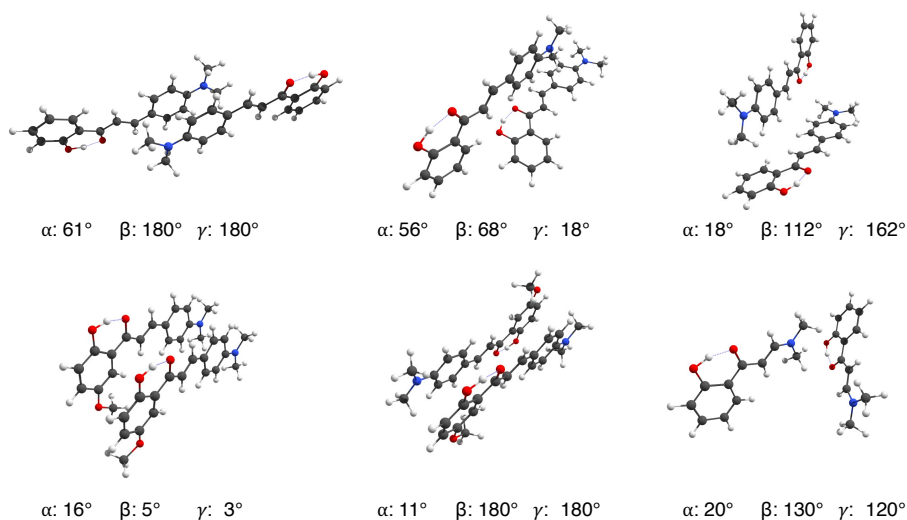


Figure 7.15: Example dimers and associated α , β and γ angles in **HC1**, **HC5**, and **HP1**.

for efficient charge or energy transfer, and that transfer will occur through only a few particular dimers.

Figure 7.16 shows the dimer distribution densities for the β and γ angles for **HC** (top row) and **HP** (bottom row). Key regions are highlighted as an example in the upper plot of panel a); for example at $\beta=90, \gamma=0$, a herringbone (Hb) stack is witnessed with the long axes arranged in parallel. For both **HC** and **HP** systems, the majority of dimers have β and γ angles close to 180° (top right of plot), indicating that the most common dimer configuration is a cofacial arrangement where the carbonyl groups align antiparallel, at opposing ends of the molecule from each other. This results in an antiparallel alignment of the S_1 transition dipole moment of each monomer. However, as panels b) and c) show, when the α angle is used as a filter, the configurations with

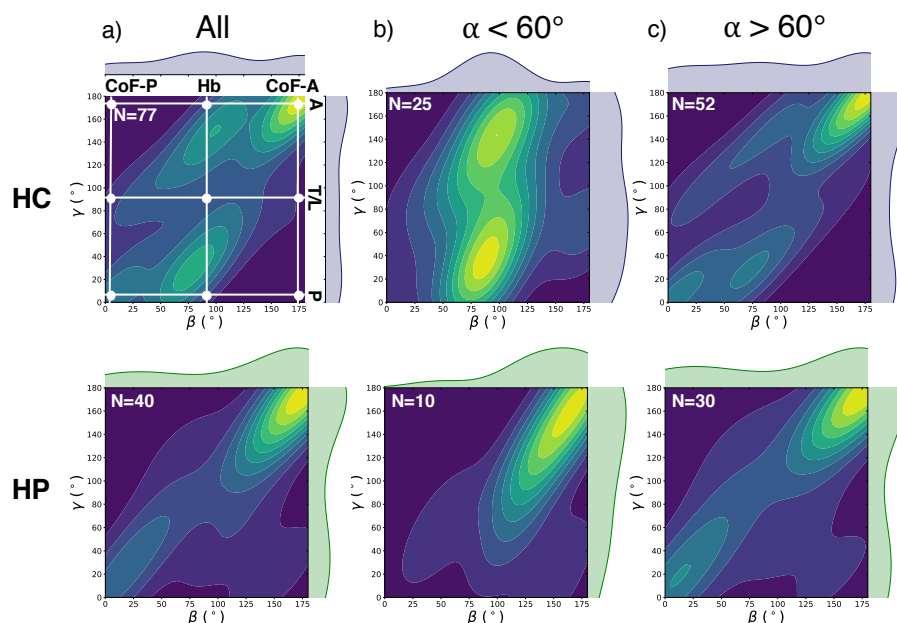


Figure 7.16: Panel a), left; Probability density map of the β and γ angles for **HC** (top) and **HP** (bottom) dimers. Key configurations are labelled on the axes, as explained in the text. Panel b), centre; probability density for the subset of dimers where $\alpha < 60^\circ$. Panel c), right; probability density for the subset of dimers where $\alpha > 60^\circ$.

more acute azimuthal angles are mostly herringbone in nature for **HC**, with carbonyl groups at the same ($\gamma = 0^\circ$) or opposite ends of the dimer ($\gamma = 180^\circ$). There also exist dimers close to this arrangement, with deviations in both x and y . In the relatively few **HP** systems with $\alpha < 60^\circ$, configurations lie on the diagonal between herringbone and cofacial.

The cofacial arrangements favoured by the Kasha model occur at large slip displacements in the x or y plane ($\alpha > 60^\circ$), and are more like edge-edge coplanar arrangements rather than the well-known π -stack. Only in **HC5** is there significant cofacial π -stacking between dimers, with other cofacial arrangements in **HC** and **HP** having larger x -slip, as is common for aromatic groups. For **HC** compounds, 63% of the cofacially aligned dimers have a x -slip of less than half a molecule, whereas 68% of cofacially-aligned **HP** dimers have a x -slip of more than half a molecule, as shown in Figure 7.17. So while the cofacial, π -stacked arrangement is rare for both families, it is more prominent in **HC** compounds than their mono-aryl **HP** counterparts. The cofacial arrangement is particularly dominant in **HC5**.

Overall, the significant dimer arrangement in **HP** compounds is a herringbone structure, with

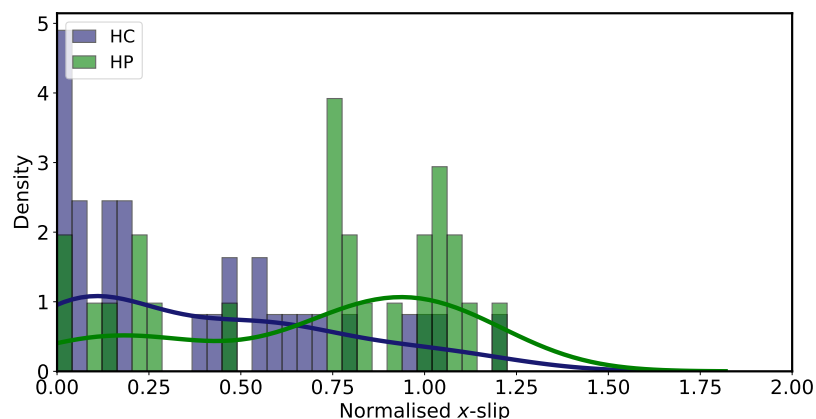


Figure 7.17: The density of slip distances for each molecular dimer in the x -plane (long axis) for cofacial dimers. The slip is normalised by the length of the long axis x for each molecule, such that slip is molecule independent.

the majority of cofacial arrangements having a large x or x -slip with minimal $\pi\pi$ interactions due to the single aryl groups aligning at $y=180^\circ$. The α angle is generally larger than in **HC**, indicating a larger slip, with overlapping monomers distributed around a cofacial stacking. The prominence of the herringbone arrangement in **HC** systems is replaced by a propensity for a T-shape packing, quantified by the γ angles distributed around 90° . In the next section, we show how these geometric parameters influence the exciton coupling in the **HC** and **HP** families.

7.3.7 Intermolecular Interactions in the Molecular Crystal

Localisation of the electronic excited state onto one monomer of the molecular crystal has been shown to be an important step in the relaxation process of ESIPT systems in the solid state in Chapter 6. For the dimers discussed above, the coupling J_{ij} between monomers i and j is calculated in Troisi's diabaticization scheme based on the orthogonal transformation of adiabatic states to diabatic states (Equation 2.33).^{49,278} In this Chapter this method is extended to assess the effect of a third monomer k on the exciton coupling, where in a trimer chromophore, \mathbf{H}^D becomes a 3x3 matrix

$$\begin{bmatrix} E_i^D & J_{ij} & J_{ik} \\ J_{ji} & E_j^D & J_{jk} \\ J_{ki} & J_{kj} & E_k^D \end{bmatrix} = \begin{bmatrix} C_{11} & C_{12} & C_{13} \\ C_{21} & C_{22} & C_{23} \\ C_{31} & C_{32} & C_{33} \end{bmatrix} \begin{bmatrix} E_i^A & 0 & 0 \\ 0 & E_j^A & 0 \\ 0 & 0 & E_k^A \end{bmatrix} \begin{bmatrix} C_{11} & C_{12} & C_{13} \\ C_{21} & C_{22} & C_{23} \\ C_{31} & C_{32} & C_{33} \end{bmatrix} \quad (7.1)$$

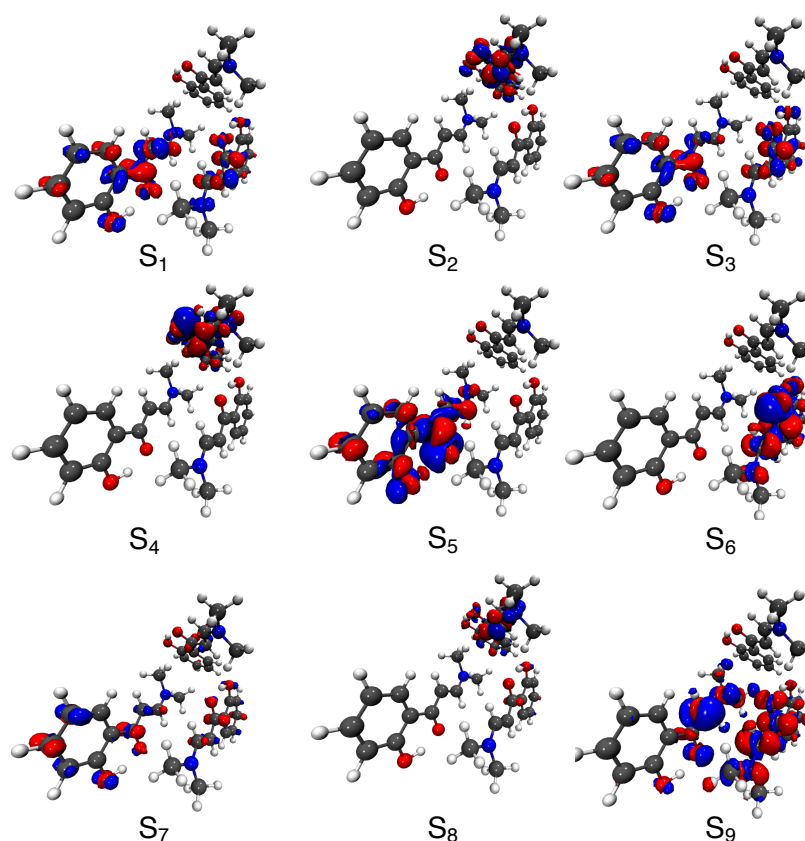


Figure 7.18: Electron density difference maps for the first nine excited state of the **HP1** trimer. The same colour scheme is used as in Figure 5.1

where the coupling J_{ij} between monomers i and j incorporates the effect of monomer k , which can be quantified through comparison of the dimeric and trimeric J_{ij} . Analysis of excitations at the Franck-Condon geometry for a trimer chromophore shows that for **HP1**, the bright state is delocalised over two of the molecules arranged in a cofacial arrangement. This is shown in Figure 7.18. A delocalised state over the whole trimer is not observed. Analysis of the excitations of the three types of dimer inherent in the trimer reveal that in each case, regardless of the stacking arrangement and despite the close aggregation of monomers, the excitation is delocalised over no more than two monomers.

To quantify the effect of the third molecule on the exciton coupling, the exciton coupling for a trimer system was calculated in **HP1**, **HC1**, and **HC5**. It is found that the addition of a third molecule has only a small effect on the dimer coupling in **HP1** and **HC1**, where the increased

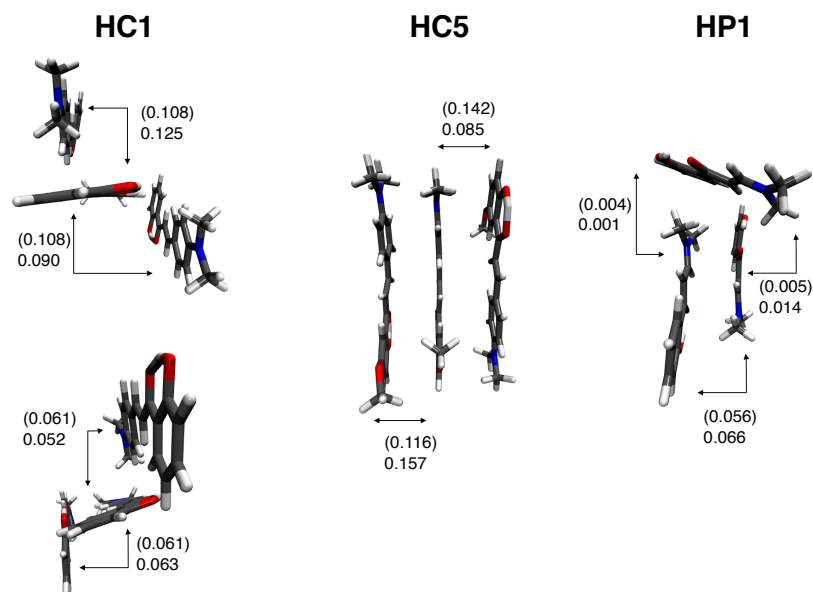


Figure 7.19: Schematic of the trimers extracted from unit cells of **HC1**, **HC5** and **HP1**. Exciton couplings considering the trimer are shown. In parenthesis are the couplings considering only a dimer. Calculated at ω B97X-D/6-311++G(d,p) level of theory.

coupling in one dimer is compensated for by the decreased coupling in the other dimer, with difference of less than 0.02 eV. The largest effect is seen in **HC5** due to the cofacial packing of the trimer system, where the central monomer is sandwiched by two cofacially stacked monomers, one parallel and one antiparallel, as shown in 7.19. For **HC1**, two trimers are used to capture both parallel and antiparallel stacked dimers.

These perturbations are no larger than the inherent modulation of couplings in the dynamic regime.^{46,49} As such, focus from here will be on dimer couplings where the presence of exterior molecules has been neglected. The exciton couplings for all dimers and the identity of the dimer with the largest J are shown in Figure 7.20.

In **HC1-4**, where the closest packed dimers are herringbone in nature, similar dimer configurations are present. For **HC-2**, the identity of the dimer with the largest coupling changes due to a lateral displacement of one monomer increasing the centroid distance to 8.5 Å and thus reducing the coupling in the herringbone stacked dimer. The identity of the largest coupled dimer changes to a cofacial, edge-edge stacked dimer with $\alpha = 87^\circ$, where minimal overlap reduces the coupling J . For **HC-1,3,4**, the herringbone stacking pattern is exhibited where the largest coupling is found in **HC1**, where the monomers are most tightly packed. In **HC5-7**, face-face stacked dimers

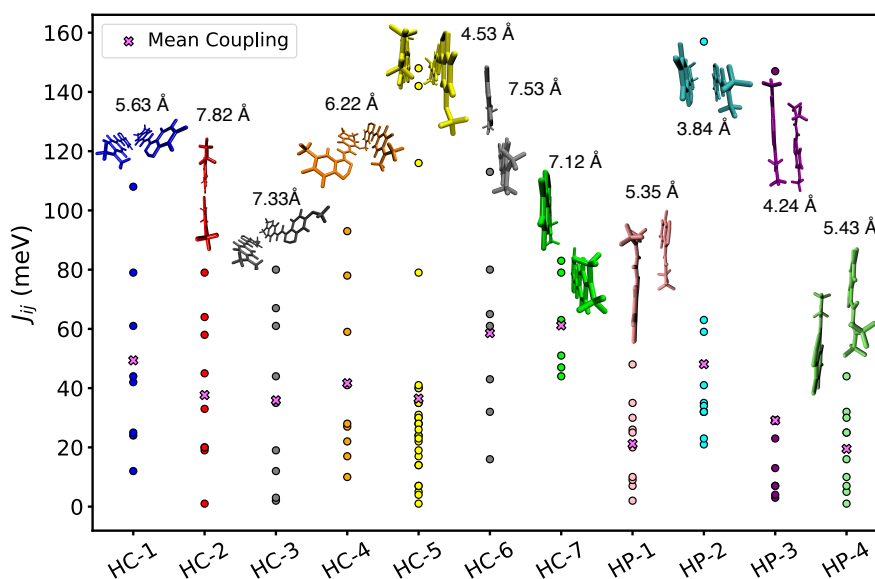


Figure 7.20: Exciton couplings J between monomers i and j in the dimers identified in **HC** and **HP**. The mean coupling is also shown, along with the distance in angstroms between the constituent monomer centroids.

are more prevalent in the crystal structure. The size of the coupling in **HC6** is reduced compared to **HC5** due to the y displacement of one of the monomers. It is further reduced in **HC7** due to an increased x -slip. In the **HP** compounds, the large α and x -slip values systematically reduce the average coupling. In each **HP** derivative there exists one close packed, cofacial dimer which exhibits the largest coupling. In **HP2-3**, the crystal structures afford more efficient cofacial stacking with x -slip values of only 1 Å, resulting in the largest couplings of all investigated systems.

As shown in Figure 7.21a, the coupling J correlates linearly with half of the energy splitting for the S_1 and S_2 states of the dimer. This is somewhat surprising, given the simplicity of the original model (Section 2.3.2), the polarity of the molecules in question and their generally nonparallel stacking. The energy splitting is perhaps the simplest way to obtain the exciton coupling in the Kasha regime, although it is more expensive than using atomic-centred transition charges, or the PDA approximation, since the supermolecular calculation must be done rather than one monomer calculation. At small intermolecular distances ($<4\text{Å}$), these computationally efficient metrics can underestimate the couplings due to them only considering the Coulomb interaction.⁵² The linear correlation here shows that the general Kasha interpretation of the coupling applies here and that the diabaticization method to obtain the couplings reproduces the supermolecular coupling.

Table 7.2: Dimer types located for each molecular crystal. Significant increase in **HC5** dimers due to rotational flexibility of the methoxy group.

System	H-aggregates	J-aggregates	Total
HC1	4	4	8
HC2	5	4	9
HC3	4	5	9
HC4	7	2	9
HC5	19	10	29
HC6	4	3	7
HC7	6	0	6
HP1	5	5	10
HP2	5	6	11
HP3	4	5	9
HP4	5	5	10

The role of H- and J-aggregates is investigated by assigning dimers based on the oscillator strength of the S_1 (J) and S_2 (H) excitation, which offers better resolution than using the energy shift. This is summarised in Table 7.2. In **HC** systems, 60% of dimers are J-aggregates, while in **HP** systems the J-aggregate population is 58%. For **HC-4** and **HC-5**, which are nonemissive, the J-aggregate population drops to 22% and 32%, respectively. Important to note, however, is that emission in K^* is from a localised excited state, and thus monomer regime should dominate the emission characteristics. In ESIPT systems, the role of H- and J-aggregates is expected to be prominent only at absorption, and the J-aggregates are not responsible for the AIE behaviour due to the localised emission.

In the Kasha model, for a perfectly stacked dimer with no x -slip, the oscillator strength of the S_2 state should be double that of the monomer state. Figure 7.21b shows the relationship between the x -slip in the dimers and the oscillator strength, namely the difference in oscillator strength between the S_2 and S_1 states in the dimer, normalised by the corresponding monomer excitation energy. These systems generally fit the Kasha model, as when the x -slip is zero, the model predicts an enhanced S_2 intensity of 2.10 for the **HCs** and 1.83 for the **HPs**. With increasing x -slip, the difference in oscillator strength between the two states decreases until the inversion to J-aggregates is witnessed ($f_{S_1} > f_{S_2}$). For the **HCs** this occurs at a x -slip of 52% and at 46% for the **HPs**. The largest group of outliers are cofacially stacked dimers, where a larger shift is seen at lower slip distances due to the minimal x -slip and archetypal stacking.¹⁷⁶

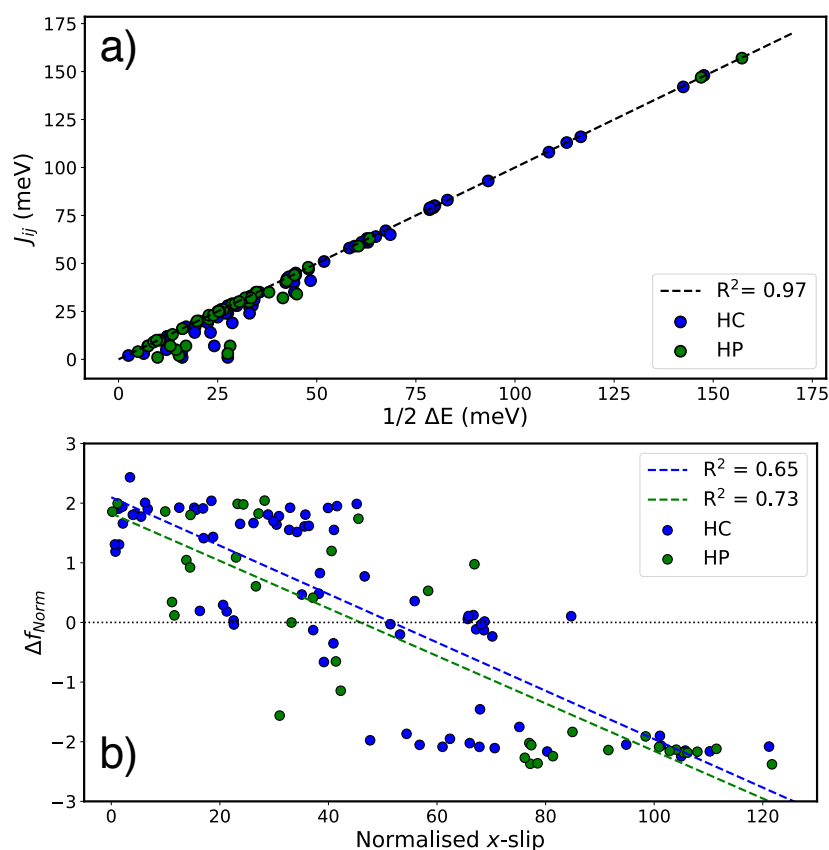


Figure 7.21: Panel a), top; Correlation between the energy splitting of the dimer states and the exciton coupling. Panel b), bottom; Linear regression of the x -slip against the difference in oscillator strength between the S_2 and S_1 states in dimers.

7.3.8 Exciton Hopping

For fluorescence to occur from the K^* state, the exciton must localise onto one monomer to enable ESIPT. In competition with this is exciton hopping, which will prevent localisation. Exciton hopping rates ν_{ij} between monomers i and j in a molecular crystal can be calculated based on a Marcus hopping scheme,^{132,133,279,280}

$$\nu_{ij} = \frac{J_{ij}^2}{\hbar} \sqrt{\frac{\pi}{\lambda k_B T}} \exp \left[-\frac{\lambda}{4k_B T} \right] \quad (7.2)$$

where k_B is the Boltzmann constant, \hbar is the reduced Planck constant, T is the temperature (298K), and λ is the internal reorganisation energy. The external reorganisation energy, of the

exterior molecules, is neglected here, since the MM-level atoms are frozen during optimisation.

Solid state reorganisation energies λ_A in keto and, when located, enol minima were calculated for ONIOM((TD-) ω B97X-D/6-31G(d):UFF) models with a monomer chromophore using Equation 3.10. Figure 7.22 shows the exciton coupling, reorganisation energy, and the associated exciton hopping rate (using a log scale) for each dimer. In Table 7.3 the reorganisation energies and largest rates in each channel are given. The hopping rate ν is ultrafast in the enol regime (**HC1-4,6,7**), where the planar conformation confers a relatively low reorganisation energy λ (244 meV on average). The lowest ν for **HC1** is $5 \times 10^{11} \text{ s}^{-1}$, while the rate of ESIPT in the molecular crystal, through time resolved spectroscopy, is $3 \times 10^{11} \text{ s}^{-1}$.²⁰² In Section 5.3.4, it was calculated that the rate of ESIPT in vacuum is $2.71 \times 10^{12} \text{ s}^{-1}$. Intramolecular hopping will therefore compete with ESIPT where there is a stable E^* minimum. Due to similarity of the electronic and crystal structures, this should also be the case for **HC2-4,6,7**, hence opening nonradiative intramolecular decay channels for these systems and a source of quantum yield leak.

For the **HP** family the stabilisation arising from ESIPT is larger than for the **HC** systems and will produce a larger Stokes shift, as is the case experimentally. In general the larger λ values due to ESIPT decrease the hopping rate by up to three orders of magnitude compared to the E^* hopping. Due to the increased organisation energy arising from tautomerism, localisation and ESIPT will be favoured over exciton hopping. By modifying the chromophore molecular structure through removal of the second aryl group, the bias towards ESIPT is increased with respect to the **HC** systems due to the instability the planar E^* conformer. As such, in **HP** the radiative decay channel through ESIPT is favoured at the expense of the intermolecular deactivation channel in E^* due to the intramolecular properties of the chromophore.

To explore the hopping rate close to the Franck-Condon state for **HP** systems, we use the exemplar **HP1** and optimise the cofacial dimer chromophore in S_0 and S_1 states. In particular, we locate the partially cis-trans isomerised E^* minimum which was located in vacuum in Section 7.3.1. Geometric relaxation in E^* in **HP1** affords a torsion in the bridging unsaturated C-C bond to a non-fluorescent state and a reorganisation energy of 2114 meV. As a direct consequence, the hopping rate for such a large λ is $3.24 \times 10^4 \text{ s}^{-1}$. For comparison, the smallest hopping rate for **HC1** in E^* is $5.17 \times 10^{11} \text{ s}^{-1}$ and, using the same methodology as **HP1**, $3.92 \times 10^{11} \text{ s}^{-1}$ in **HC5**. Exciton hopping is therefore reduced in **HP** due to the relatively small exciton coupling, helping to fulfil design rule two.

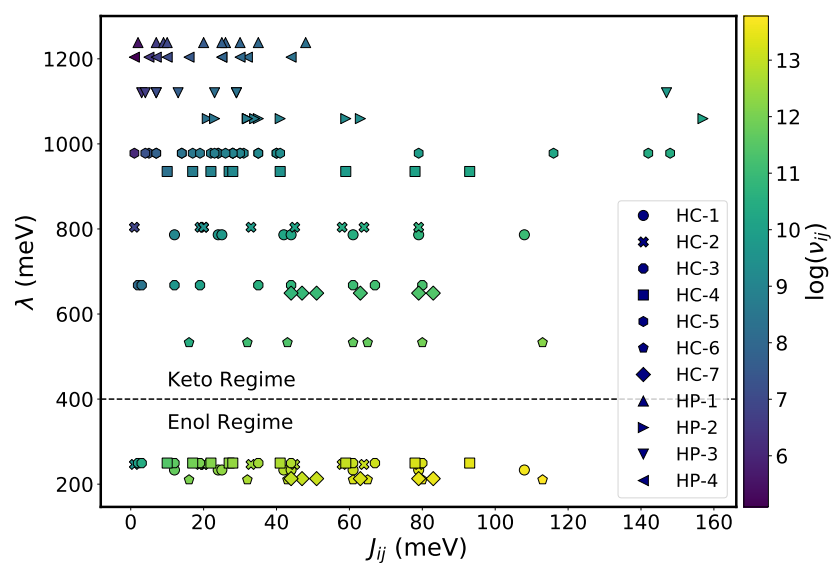


Figure 7.22: Coloumap of the exciton hopping rate ν_{ij} on a \log_{10} scale, as a function of the exciton coupling J_{ij} and the reorganisation energy λ , calculated *via* Equation 7.2.

7.4 Conclusions

In this Chapter we have systematically evaluated the photo behaviour of a range of solid-state emitters based on the ESIPT mechanism. The design rules established in Chapters 5 and 6 have been scrutinised for an expanded range of compounds, increasing the scope of the study of ESIPT chromophores. In the **HC** family of compounds, AIE is witnessed for five of the seven compounds, with Φ_{PL} ranging from 0.10 to 0.84. In the **HP** systems, which differ by containing only one aryl ring, all reported compounds are emissive in the solid state with Φ_{PL} of 0.72-0.84. In each crystal structure, there exist a range of dimers each with their own excitonic profile. In the **HC** systems, the herringbone stacking is prominent, with exciton coupling enhanced by the two aryl rings promoting $\pi - \pi$ interactions which are mostly absent in their **HP** counterparts.

In the **HC** compounds, after photoexcitation to the S_1 state, exciton hopping in the enol tautomer will compete with ESIPT on account of minimal electron density loss on the phenol oxygen and the stability of the planar enol tautomer, which results in only a small reorganisation energy. Here the hopping rate is several orders of magnitude larger than in the K^* state and will allow nonradiative dissipation of the excited state. Conversely in the **HP** compounds, and **HC5**, the electron density loss is increased on the oxygen and ESIPT is more favourable, coupled with the

System	$\lambda_A E^*$ (meV)	$\lambda_A K^*$ (meV)	$\nu_{max} E^*$ (s^{-1})	$\nu_{max} K^*$ (s^{-1})
HC1	233	786	4.19×10^{13}	1.05×10^{11}
HC2	246	804	1.92×10^{13}	4.66×10^{10}
HC3	249	668	1.90×10^{13}	1.98×10^{11}
HC4	250	936	2.56×10^{13}	1.67×10^{10}
HC5	-	978	-	2.73×10^{10}
HC6	210	533	6.03×10^{13}	1.64×10^{12}
HC7	213	649	3.15×10^{13}	2.59×10^{11}
HP1	-	1238	-	2.03×10^8
HP2	-	1059	-	1.34×10^{10}
HP3	-	1120	-	6.30×10^9
HP4	-	1204	-	2.41×10^8

Table 7.3: Adiabatic reorganisation energies (λ_A) and largest hopping rates ν in the enol (where available) and keto channels for **HC** and **HP** systems.

planar E^* tautomer being unstable. The stability of the K^* state increases the reorganisation energy λ of the chromophore and subsequently will increase the population of the ESIPT channel in these systems. The K^* state will be highly localised with minimal hopping. In **HC1**, emission from E^* will increase unfavourable self-absorption and contribute to the lower quantum yield compared to **HP1**.

The K^* minimum takes a planer conformation in the solid state, which considerable oscillator strength for emission back to S_0 . **HP1** has an energetically inaccessible MECI, as for **HC1**, whereas in **HC5** the MECI is energetically accessible. As for **HC1**, the MECI for **HP1** in the crystal takes a distorted, pyramidalised geometry and is energetically inaccessible in the decay path. As such, emission will occur from the planar K^* minimum for the **HP** compounds and with larger Φ_{PL} , due to the increase in the population of the K^* channel. Such is the similarity in absorption and emission spectra in the **HP** family, this mechanism is expected to be independent of the substituents present in this study.

These findings help to connect the electronic, molecular picture with the crystalline regime for organic light-emitting materials. In these ESIPT emitters, the intermolecular interactions dominate in the Franck-Condon regime at photoabsorption. From here, the electronic structure and the character of the excited state, inherently molecular properties, become dominant. The deconstruction of intra- and intermolecular factors here, connecting the chromophore with its crystal structure, offers a step forward in first principles design of solid state luminescent materials exploiting ESIPT.

8 Conclusions and Outlook

8.1 Mechanistic Overview and Design Rules

We have established the AIE mechanism in two families of ESIPT molecules, and how the photodecay is affected by electronic substituents, intermolecular electrostatics, excitonic interactions, and structural modification. We have determined that the compounds undergo AIE due to the RACI mechanism. The RACI model is a recent mechanistic interpretation for AIE, and there are still relatively few molecules which are known to undergo AIE in this way. Moreover, the known compounds are relatively simple, with containing a dominant decay channel. Our research has shown that the RACI model can be extended to incorporate ESIPT molecules with multiple competing decay channels.

To complement this we have illustrated how in compound **5**, there is no fluorescence in either vacuum or aggregate due to the persistence of a low energy conical intersection. Just a small structural modification between **1** and **5** completely changes the physical behaviour of the material, a phenomenon which we can account for. Our calculations show that this is due to the change in electronic structure and electronic density distribution upon excitation, and that electrostatic interactions can aid in the lowering of the conical intersection energy in the aggregate. As such, control over both the electronic and aggregate properties are crucial for enabling fluorescence in the solid state.

Understanding the fundamental cause of the contrasting properties of **HC1** and **HC5** enables the proposed mechanisms to be tested on the related **HP** systems. These have increased quantum yield of fluorescence, and our calculations show that this is due to a Goldilocks-like combination of properties in the molecular crystal. Favourable excited state character mobilises the proton. The large reorganisation energies lead to exciton localisation and efficient population transfer to the keto minimum, and the high energy conical intersection make fluorescence the most likely deactivation pathway. The mechanistic insight established for the **HC** systems directly contributes to understanding the efficiency of the **HP** compounds.

We can extrapolate these mechanistic findings in to general design rules for highly emissive ESIPT materials. Incorporation of the following features into the next generation of ESIPT emitters will increase their efficiency and fluorescent properties:

1. To maximise the population of the ESIPT channel, chromophore design should encourage a highly labile proton, where electronic excitation destabilises the E^* state
2. Packing modes should limit π - π interactions, which enable exciton coupling and delocalisation. However, if the ESIPT is favourable enough, the localisation inherent to the K^* state can overcome unfavourable stacking arrangements.
3. In the K^* form, solid state conical intersections are accessed *via* a combination of pyramidalisation and rotation. This can be made more unfavourable by tethering and chromophore design, where we have shown that simple probes such as scanning coordinates in vacuum can predict K^* stability.

We hope to realise these findings by working with experimental groups to synthesise systems obeying these rules, further developing the field of luminescent organic materials for the next generation of emissive technologies.

8.2 Detailed Summary of Results

The first step was to initially explore the PESs of the five systems in vacuum. This allowed for an isolated analysis of the effect of substituents on the parent **HC1**. We uncovered two decay pathways in vacuum which are open to the five systems, where relaxation can occur either in the E^* state, or *via* ESIPT to the K^* state through intramolecular rotation. In both channels, an energetically accessible MECI can funnel population nonradiatively back to the ground state, where GSIPT completes the four-level photocycle. The substituents determine the population of the enol and keto channels, which we investigated through TSH dynamics for **HC1** and **HC5**, which showed the biggest deviation in absorption and emission energies in the static calculations. Due to the increased electron density loss from the phenol oxygen on account of the methoxy group, in **HC5** the rate of ESIPT is increased and the lifetime of the K^* state is reduced with respect to **HC1**. This clear electronic effect between the two systems encouraged us to study their photochemistry in the solid state.

In Chapter 6, we present a study of the PES in the solid state for **HC1** and **HC5**. We use QM:MM models, with both electrostatic and mechanical embedding, with variable region size, and Ewald embedding, to explore as fully as possible the intertwined interactions present in the molecular crystal, considering ground and excited state minima, as well as conical intersections. The inherent electronic structure differences between the ground and excited state for ESIPT systems, coupled with the large intramolecular rotation in vacuum, led us to investigate the AIE through the RACI model, rather than the FGR-RIM. We find that in **HC1**, an excellent absorption energy is predicted and that dual emission from both E^* and K^* minima is possible. While the E^* emission is expected to be mostly self-absorbed, the K^* emission is bright, although is somewhat overestimated with respect to experiment. Crucially, we find that the **HC1** is able to fluoresce because the MECI lies above the excitation energy. Conversely, **HC5** can be expected to be dark because the MECI is energetically accessible. Other deactivation mechanisms are possible in **HC5**, for instance delocalisation in the E^* state. However, the propensity for ESIPT means that the RACI model is expected to dominate.

Stepping away from the specific mechanisms in the **HC** compounds, the effect of the electronic structure and the crystalline environment have on the PES is of general interest. Vacuum calculations at the obtained QM:MM geometries show that the energy of the MECIs are inherent to the chromophore itself. The crystalline environment provides the intermolecular interactions which prevent relaxation to the vacuum minima and MECIs, and can modulate the total energy, but their relative stability is an electronic factor.

We hypothesised that the more efficient ESIPT luminophore could be obtained by combining the properties of **HC1** and **HC5**. A deactivation route in **HC1** is the stability of the E^* state, where fluorescence or exciton hopping can occur. If the propensity for ESIPT in **HC5** could be incorporated, the population of the K^* channel would increase and more fluorescence would be witnessed. Alternatively, in **HC5**, making the conical intersection less accessible by preventing the pyramidalisation of the carbonyl by introducing fused rings to the molecular structure.

In 2016, the Zhang group synthesised a set of ESIPT materials with similar structural characteristics as the **HCs**. The **HPs** show AIE with exceptional quantum efficiencies in the solid state. In Chapter 7, we expanded the scope of our work to examine the similarities and differences of the **HCs** and **HPs**. For this, we took a more quantitative approach to studying the crystalline morphology. Dimer relationships are known to be important for charge and energy transfer, and so we

created density maps based on the configuration of dimers found in each of the molecular crystals. The algorithms for searching and classification of dimers and calculation have been implemented into `fromage`.⁹⁰ For the data in Chapter 7, a specific algorithm was written to quantify dimers based upon the molecular structure of the **HC** and **HP** systems, namely by locating molecular axes through the carbonyl groups. This has been generalised in the `fromage` implementation, where a plane is fitted to the molecular geometry and angles between planes are calculated in a dimer, thus meaning any molecular species can be quantified. Work in this area is ongoing in the group, for example to track dimer configurations during aggregation in molecular dynamics.

In the **HC** and **HP** families we calculated the exciton couplings for 121 dimers and, in combination with the reorganisation energies, calculated the exciton hopping rates within the Marcus framework. We found exciton delocalisation to be far more prevalent in the **HCs** than the **HPs**, where the lack of a stable planar E^* minimum promotes ESIPT more readily and produces a very large reorganisation energy. Once in the K^* channel, multireference QM:MM methods show that the MECI is even more inaccessible than for **HC1**. The radiative rates were estimated by simulating emission spectra. The combination of efficient population transfer to K^* and the inaccessible MECI could be responsible for the enhanced quantum efficiencies, as was hypothesised. Modelling exciton diffusion and dynamics would be an interesting extension for these systems, where Monte Carlo simulation could harness the stochastic nature of these processes.

In Chapter 7 we also considered the FGR-RIM interpretation by calculating the HR factors in vacuum and the solid state. The large torsional rotation (90°) and the anharmonic excited state PES results in gigantic HR factors in vacuum for **HC1** and **HP1**, which are of course reduced significantly in the solid state where the conformation remains planar. As such, the applicability of the FGR-RIM model is questionable for these systems. Moreover, even for **HC5**, there is a reduction of the HR factors, yet no AIE is witnessed. Calculating the nonradiative decay rates was outwith the scope of our work, but would be an interesting avenue to further explore.

Another such avenue is the nonradiative decay in both vacuum and solid state of **HC4**, which experimentally is attributed to the nonplanarity of the chromophore. However, the conclusions we have established based on **HC5** show that there is perhaps a similar nonradiative decay funnel present. The study of the solid state PES of **HC4** would be an interesting case in future. Also of interest is to specifically analyse the packing mode effect by arranging molecules of **HC1** in the packing arrangement of **HC5**, and determining the change in the PES.

The modelling of photochemistry in molecular crystals is a relatively young but rapidly developing field. Sitting somewhere in between molecular and materials chemistry, it is an area ripe for exploration. The inherent difficulties and intricacies involved in modelling excited state processes are increased when incorporating the environment, with the current state of the art methods building on developments in other fields. Progress into methods to model these processes are in development, mainly through different embedding models. On this part, our group is active in pursuing this research avenue, and while more standard QM:MM methods have been used in the majority of this thesis, new developments such as the Ewald scheme have been applied to gain a more sophisticated understanding into such processes. Further developments are ongoing on these methodologies. We are implementing self-consistent polarisation schemes within QM:QM' frameworks, which work across electronic structure codes and with different QM approximations, based on multireference and density functional methods.⁸⁹ By expanding the tool set available for probing excited state processes in molecular crystals, theoretical models and interpretations can continue to advance as we move towards the design of the next generation of light-emitting organic materials.

9 Bibliography

- [1] J. Zhang, Q. Zou and H. Tian, *Adv. Mater.*, 2013, **25**, 378–399.
- [2] O. Ostroverkhova, *Chem. Rev.*, 2016, **116**, 13279–13412.
- [3] J. Mei, N. L. C. Leung, R. T. K. Kwok, J. W. Y. Lam and B. Z. Tang, *Chem. Rev.*, 2015, **115**, 11718–11940.
- [4] V. S. Padalkar and S. Seki, *Chem. Soc. Rev.*, 2015, **45**, 169–202.
- [5] C. J. Cramer, *Essentials of Computational Chemistry, Theories and Models*, Wiley-Blackwell, New York, 2002.
- [6] E. Schrödinger, *Ann. Phys.*, 1926, **384**, 489–527.
- [7] M. Born and R. Oppenheimer, *Ann. Phys.*, 1927, **389**, 457–484.
- [8] A. Szabo and N. S. Ostlund, *Modern Quantum Chemistry: Introduction to Advanced Electronic Structure Theory*, Dover Publications, Inc., Mineola, 1996.
- [9] M. Born and K. Huang, *Dynamical Theory of Crystal Lattices*, Oxford University Press, New York and London, 1954.
- [10] R. Crespo-Otero and M. Barbatti, *Chem. Rev.*, 2018, **118**, 7026–7068.
- [11] G. Worth and L. S. Cederbaum, *Annu. Rev. Phys. Chem.*, 2004, **55**, 127–158.
- [12] T. Yonehara, K. Hanasaki and K. Takatsuka, *Chem. Rev.*, 2012, **112**, 499–542.
- [13] J. Franck and E. G. Dymond, *J. Chem. Soc. Faraday Trans.*, 1926, **21**, 536.
- [14] D. G. Truhlar and C. A. Mead, *Phys. Rev. A*, 2003, **68**, 32501.
- [15] M. Garavelli, *Theo. Chem. Acc.*, 2006, **116**, 87–105.
- [16] M. Robb, M. Garavelli, M. Olivucci and F. Bernardi, *Reviews in Computational Chemistry*, John Wiley & Sons, Ltd, 2007, vol. 15, pp. 87–146.
- [17] W. Domcke, D. R. Yarkony and H. Köppel, *Conical Intersections*, World Scientific Publishing Co Pte Ltd, 2011, vol. 17.
- [18] F. Plasser, M. Barbatti, A. J. A. Aquino and H. Lischka, *Theo. Chem. Acc.*, 2012, **131**, 1–14.

- [19] B. G. Levine, J. D. Coe and T. J. Martínez, *J. Phys. Chem. B*, 2008, **112**, 405–413.
- [20] J. C. Tully, *J. Chem. Phys.*, 1990, **93**, 1061–1071.
- [21] M. Barbatti, *Wiley Interdiscip. Rev. Comput. Mol. Sci.*, 2011, **1**, 620–633.
- [22] W. C. Swope, H. C. Andersen, P. H. Berens and K. R. Wilson, *J. Chem. Phys.*, 1982, **76**, 637–649.
- [23] J. Pittner, H. Lischka and M. Barbatti, *Chem. Phys.*, 2009, **356**, 147–152.
- [24] I. G. Ryabinkin, J. Nagesh and A. F. Izmaylov, *J. Phys. Chem. Lett.*, 2015, **6**, 4200–4203.
- [25] G. Granucci and M. Persico, *J. Chem. Phys.*, 2007, **126**, 134114.
- [26] T. Förster, *Z. Phys. Chem. N. F.*, 1954, **1**, 275–276.
- [27] T. Förster, *Angew. Chem. Int. Ed. Engl.*, 1969, **8**, 333–343.
- [28] S. Grimme, *Angew. Chem., Int. Ed.*, 2008, **47**, 3430–3434.
- [29] C. R. Martinez and B. L. Iverson, *Chem. Sci.*, 2012, **3**, 2191–2201.
- [30] S. W. Thomas, G. D. Joly and T. M. Swager, *Chem. Rev.*, 2007, **107**, 1339–1386.
- [31] R. T. K. Kwok, C. W. T. Leung, J. W. Y. Lam and B. Z. Tang, *Chem. Soc. Rev.*, 2015, **44**, 4228–4238.
- [32] Y. Hong, J. W. Y. Lam and B. Z. Tang, *Chem. Commun.*, 2009, 4332.
- [33] J. Mei, Y. Hong, J. W. Y. Lam, A. Qin, Y. Tang and B. Z. Tang, *Adv. Mater.*, 2014, **26**, 5429–5479.
- [34] L. Chen, S. Xu, D. McBranch and D. Whitten, *J. Am. Chem. Soc.*, 2000, **122**, 9302–9303.
- [35] D. Lee, O. Bolton, B. C. Kim, J. H. Youk, S. Takayama and J. Kim, *J. Am. Chem. Soc.*, 2013, **135**, 6325–6329.
- [36] J. Gierschner, Y.-S. Huang, B. Van Averbeke, J. Cornil, R. H. Friend and D. Beljonne, *J. Chem. Phys.*, 2009, **130**, 044105.
- [37] J. Gierschner and S. Y. Park, *J. Mater. Chem. C*, 2013, **1**, 5818.
- [38] J. Gierschner, L. Lüer, B. Milián-Medina, D. Oelkrug and H.-J. Egelhaaf, *J. Phys. Chem. Lett.*, 2013, **4**, 2686–2697.
- [39] N. J. Hestand and F. C. Spano, *Acc. Chem. Res.*, 2017, **50**, 341–350.
- [40] J. Shi, L. E. Aguilar Suarez, S. J. Yoon, S. Varghese, C. Serpa, S. Y. Park, L. Lüer, D. Roca-Sanjuán, B. Milián-Medina and J. Gierschner, *J. Phys. Chem. C*, 2017, **121**, 23166–23183.

- [41] M. Kasha, H. R. Rawls and M. Ashraf El-Bayoumi, *Pure Appl. Chem.*, 1965, **11**, 371–392.
- [42] F. C. Spano and D. Beljonne, *The WSPC Reference on Organic Electronics: Organic Semiconductors*, World Scientific Publishing Co Pte Ltd, ch. 4, pp. 93–130.
- [43] N. J. Hestand and F. C. Spano, *Chem. Rev.*, 2018, **118**, 7069–7163.
- [44] B. Y. M. Kasha, *Discuss. Faraday Soc.*, 1950, **9**, 14–19.
- [45] C. Brückner, M. Stolte, F. Würthner, J. Pflaum and B. Engels, *J. Phys. Org. Chem.*, 2017, **30**, 1–13.
- [46] J. Aragón and A. Troisi, *Adv. Funct. Mater.*, 2016, **26**, 2316–2325.
- [47] T. Stangl, P. Wilhelm, D. Schmitz, K. Remmerssen, S. Henzel, S. S. Jester, S. Höger, J. Vogelsang and J. M. Lupton, *J. Phys. Chem. Lett.*, 2015, **6**, 1321–1326.
- [48] S. Fratini, D. Mayou and S. Ciuchi, *Adv. Funct. Mater.*, 2016, **26**, 2292–2315.
- [49] J. Aragón and A. Troisi, *Phys. Rev. Lett.*, 2015, **114**, 1–5.
- [50] R. P. Fornari, P. Rowe, D. Padula and A. Troisi, *J. Chem. Theory Comput.*, 2017, **13**, 3754–3763.
- [51] T. F. Harrelson, V. Dantanarayana, X. Xie, C. Koshnick, D. Nai, R. Fair, S. A. Nuñez, A. K. Thomas, T. L. Murrey, M. A. Hickner, J. K. Grey, J. E. Anthony, E. D. Gomez, A. Troisi, R. Faller and A. J. Moulé, *Mater. Horiz.*, 2019, **6**, 182–191.
- [52] K. A. Kistler, F. C. Spano and S. Matsika, *J. Phys. Chem. B*, 2013, **117**, 2032–2044.
- [53] A. A. M. H. M. Darghouth, G. C. Correa, S. Juillard, M. E. Casida, A. Humeniuk and R. Mitric, *arXiv:1803.00056*, 2018, 1–40.
- [54] H. Yamagata, C. M. Pochas and F. C. Spano, *J. Phys. Chem. B*, 2012, **116**, 14494–14503.
- [55] C.-P. Hsu, *Acc. Chem. Res.*, 2009, **42**, 509–518.
- [56] W. P. Bricker and C. S. Lo, *J. Phys. Chem. B*, 2014, **118**, 9141–9154.
- [57] J. Sauer, *Chem. Rev.*, 1989, **89**, 199–255.
- [58] F. Libisch, C. Huang and E. A. Carter, *Acc. Chem. Res.*, 2014, **47**, 2768–2775.
- [59] J. Cheng, K. Yu, F. Libisch, J. M. Dieterich and E. A. Carter, *J. Chem. Theory Comput.*, 2017, **13**, 1081–1093.
- [60] J. Cheng, F. Libisch, K. Yu, M. Chen, J. M. Dieterich and E. A. Carter, *J. Chem. Theory Comput.*, 2017, **13**, 1067–1080.

- [61] D. Presti, F. Labat, A. Pedone, M. J. Frisch, H. P. Hratchian, I. Ciofini, M. Cristina Menziani and C. Adamo, *J. Comput. Chem.*, 2016, **37**, 861–870.
- [62] S. Dapprich, I. Komaromi, K. S. Byun, K. Morokuma and M. J. Frisch, *J. Mol. Struct. THEOCHEM*, 1999, **462**, 1–21.
- [63] M. J. Frisch, *J. Comput. Chem.*, 2003, **24**, 760–769.
- [64] L. W. Chung, W. M. C. Sameera, R. Ramozzi, A. J. Page, M. Hatanaka, G. P. Petrova, T. V. Harris, X. Li, Z. Ke, F. Liu, H. B. Li, L. Ding and K. Morokuma, *Chem. Rev.*, 2015, **115**, 5678–5796.
- [65] M.-C. Li, M. Hayashi and S.-h. Lin, *J. Phys. Chem. A*, 2011, **115**, 14531–8.
- [66] Q. Li and L. Blancafort, *Chem. Commun.*, 2013, **49**, 5966–8.
- [67] G. Sun, Y. Zhao and W. Z. Liang, *J. Chem. Theory Comput.*, 2015, **11**, 2257–2267.
- [68] D. Presti, A. Pedone, I. Ciofini, F. Labat, M. C. Menziani and C. Adamo, *Theor. Chem. Acc.*, 2016, **135**, 1–11.
- [69] L. Wilbraham, C. Adamo, F. Labat and I. Ciofini, *J. Chem. Theory Comput.*, 2016, **12**, 3316–3324.
- [70] B. Wang, X. Wang, W. Wang and F. Liu, *J. Phys. Chem. C*, 2016, **120**, 21850–21857.
- [71] X.-L. Peng, S. Ruiz-Barragan, Z.-S. Li, Q.-S. Li and L. Blancafort, *J. Mater. Chem. C*, 2016, **4**, 2802–2810.
- [72] J. Fan, L. Cai, L. Lin and C.-K. Wang, *J. Phys. Chem. A*, 2016, **120**, 9422–9430.
- [73] D. Presti, L. Wilbraham, C. Targa, F. Labat, A. Pedone, M. C. Menziani, I. Ciofini and C. Adamo, *J. Phys. Chem. C*, 2017, **121**, 5747–5752.
- [74] Y. Li, G. Wang, W. Li, Y. Wang and S. Li, *Phys. Chem. Chem. Phys.*, 2017, **19**, 17516–17520.
- [75] L. Lin, J. Fan, L. Cai and C.-K. Wang, *RSC Adv.*, 2017, **7**, 44089–44096.
- [76] W. Li, Q. Peng, H. Ma, J. Wen, J. Ma, L. A. Peteanu and Z. Shuai, *Chem. Mater.*, 2017, **29**, 2513–2520.
- [77] J. Fan, L. Lin and C.-K. Wang, *J. Mater. Chem. C*, 2017, **5**, 8390–8399.
- [78] W. D. Cornell, P. Cieplak, C. I. Bayly, I. R. Gould, K. M. Merz, D. M. Ferguson, D. C. Spellmeyer, T. Fox, J. W. Caldwell and P. A. Kollman, *J. Am. Chem. Soc.*, 1995, **117**, 5179–5197.

- [79] A. K. Rappé, L. M. Bormann-Rochotte, D. C. Wiser, J. R. Hart, M. A. Pietsch, C. J. Casewit and W. M. Skiff, *Mol. Phys.*, 2007, **105**, 301–324.
- [80] T. Vreven, K. S. Byun, I. Komáromi, S. Dapprich, J. A. Montgomery, K. Morokuma and M. J. Frisch, *J. Chem. Theory Comput.*, 2006, **2**, 815–826.
- [81] M. J. Bearpark, S. M. Larkin and T. Vreven, *J. Phys. Chem. A*, 2008, **112**, 7286–7295.
- [82] M. A. Kochman and C. A. Morrison, *J. Chem. Theory Comput.*, 2013, **9**, 1182–1192.
- [83] M. A. Kochman, A. Bil and C. A. Morrison, *Phys. Chem. Chem. Phys.*, 2013, **15**, 10803–10816.
- [84] J. Weber and J. Schmedt Auf der Günne, *Phys. Chem. Chem. Phys.*, 2010, **12**, 583–603.
- [85] D. Stueber, F. N. Guenneau and D. M. Grant, *J. Chem. Phys.*, 2001, **114**, 9236–9243.
- [86] M. Klintonberg, S. E. Derenzo and M. J. Weber, *Comput. Phys. Commun.*, 2000, **131**, 120–128.
- [87] S. E. Derenzo, M. K. Klintonberg and M. J. Weber, *J. Chem. Phys.*, 2000, **112**, 2074–2081.
- [88] L. Wilbraham, M. Louis, D. Alberga, A. Brosseau, R. Guillot, F. Ito, F. Labat, R. Métivier, C. Allain and I. Ciofini, *Adv. Mater.*, 2018, **30**, 1–8.
- [89] M. Rivera, M. Dommett and R. Crespo-Otero, *J. Chem. Theory Comput.*, 2019, **15**, 2504–2516.
- [90] M. Rivera, M. Dommett and R. Crespo-Otero, *fromage: A FRamewOrk for Molecular AGgregate Excitations*, 2018, <https://github.com/Crespo-Otero-group/fromage>.
- [91] J. Luo, Z. Xie, Z. Xie, J. W. Lam, L. Cheng, H. Chen, C. Qiu, H. S. Kwok, X. Zhan, Y. Liu, D. Zhu, B. Z. Tang, B. Z. Tang and B. Z. Tang, *Chem. Commun.*, 2001, **18**, 1740–1741.
- [92] Y. Dong, J. W. Y. Lam, A. Qin, J. Liu, Z. Li, B. Z. Tang, J. Sun and H. S. Kwok, *Appl. Phys. Lett.*, 2007, **91**, 011111.
- [93] Z. Li, Y. Dong, B. Mi, Y. Tang, M. Häussler, H. Tong, Y. Dong, J. W. Y. Lam, Y. Ren, H. H. Y. Sung, K. S. Wong, P. Gao, I. D. Williams, H. S. Kwok and B. Z. Tang, *J. Phys. Chem. B*, 2005, **109**, 10061–10066.
- [94] Z. Li, Y. Q. Dong, J. W. Lam, J. Sun, A. Qin, M. Häussler, Y. P. Dong, H. H. Sung, I. D. Williams, H. S. Kwok and B. Z. Tang, *Adv. Funct. Mater.*, 2009, **19**, 905–917.
- [95] X. Wang, J. Hu, G. Zhang and S. Liu, *J. Am. Chem. Soc.*, 2014, **136**, 9890–9893.
- [96] Y. Yuan, R. T. K. Kwok, G. Feng, J. Liang, J. Geng, B. Z. Tang and B. Liu, *Chem. Commun.*,

- 2014, **50**, 295–297.
- [97] X. Shen, G. Zhang and D. Zhang, *Org. Lett.*, 2012, **14**, 1744–1747.
- [98] Y. Hong, L. Meng, S. Chen, C. W. T. Leung, L. T. Da, M. Faisal, D. A. Silva, J. Liu, J. W. Y. Lam, X. Huang and B. Z. Tang, *J. Am. Chem. Soc.*, 2012, **134**, 1680–1689.
- [99] M. Wang, G. Zhang, D. Zhang, D. Zhu and B. Z. Tang, *J. Mater. Chem.*, 2010, **20**, 1858–1867.
- [100] Y. Hong, J. W. Y. Lam and B. Z. Tang, *Chem. Soc. Rev.*, 2011, **40**, 5361.
- [101] R. Hu, N. L. Leung and B. Z. Tang, *Chem. Soc. Rev.*, 2014, **43**, 4494–4562.
- [102] B. Z. Tang, X. Zhan, G. Yu, P. P. Sze Lee, Y. Liu and D. Zhu, *J. Mater. Chem.*, 2001, **11**, 2974–2978.
- [103] J. Chen, C. C. Law, J. W. Lam, Y. Dong, S. M. Lo, I. D. Williams, D. Zhu and B. Z. Tang, *Chem. Mater.*, 2003, **15**, 1535–1546.
- [104] C. Y. Chan, J. W. Lam, Z. Zhao, S. Chen, P. Lu, H. H. Sung, H. S. Kwok, Y. Ma, I. D. Williams and B. Z. Tang, *J. Mater. Chem. C*, 2014, **2**, 4320–4327.
- [105] W. Z. Yuan, P. Lu, S. Chen, J. W. Y. Lam, Z. Wang, Y. Liu, H. S. Kwok, Y. Ma and B. Z. Tang, *Adv. Mater.*, 2010, **22**, 2159–2163.
- [106] T. Nishiuchi, K. Tanaka, Y. Kuwatani, J. Sung, T. Nishinaga, D. Kim and M. Iyoda, *Chem. Eur. J.*, 2013, **19**, 4110–4116.
- [107] N. L. Leung, N. Xie, W. Yuan, Y. Liu, Q. Wu, Q. Peng, Q. Miao, J. W. Lam and B. Z. Tang, *Chem. Eur. J.*, 2014, **20**, 15349–15353.
- [108] H. Y. Chen, W. Y. Lam, J. D. Luo, Y. L. Ho, B. Z. Tang, D. B. Zhu, M. Wong and H. S. Kwok, *Appl. Phys. Lett.*, 2002, **81**, 574–576.
- [109] J. Huang, Y. Jiang, J. Yang, R. Tang, N. Xie, Q. Li, H. S. Kwok, B. Z. Tang and Z. Li, *J. Mater. Chem. C*, 2014, **2**, 2028–2036.
- [110] J. Huang, N. Sun, J. Yang, R. Tang, Q. Li, D. Ma and Z. Li, *Adv. Funct. Mater.*, 2014, **24**, 7645–7654.
- [111] R. Kumar Konidena, K. R. Justin Thomas, D. Kumar Dubey, S. Sahoo and J.-H. Jou, *Chem. Commun.*, 2017, **53**, 11802–11805.
- [112] X. Tang, Q. Bai, T. Shan, J. Li, Y. Gao, F. Liu, H. Liu, Q. Peng, B. Yang, F. Li and P. Lu, *Adv. Funct. Mater.*, 2018, **28**, 1–8.

- [113] Z.-L. Zhu, S.-F. Ni, W.-C. Chen, M. Chen, J.-J. Zhu, Y. Yuan, Q.-X. Tong, F.-L. Wong and C.-S. Lee, *J. Mater. Chem. C*, 2018, **6**, 3584–3592.
- [114] G. Yu, S. Yin, Y. Liu, J. Chen, X. Xu, X. Sun, D. Ma, X. Zhan, Q. Peng, Z. Shuai, B. Tang, D. Zhu, W. Fang and Y. Luo, *J. Am. Chem. Soc.*, 2005, **127**, 6335–6346.
- [115] Y. Niu, Q. Peng, C. Deng, X. Gao and Z. Shuai, *J. Phys. Chem. A*, 2010, **114**, 7817–7831.
- [116] R. Crespo-Otero and M. Barbatti, *Theor. Chem. Acc.*, 2012, **131**, 1–14.
- [117] S. Yin, Q. Peng, Z. Shuai, W. Fang, Y. H. Wang and Y. Luo, *Phys. Rev. B*, 2006, **73**, 1–5.
- [118] W. Li, L. Zhu, Q. Shi, J. Ren, Q. Peng and Z. Shuai, *Chem. Phys. Lett.*, 2017, **683**, 507–514.
- [119] Q. Peng, Y. Yi, Z. Shuai and J. Shao, *J. Chem. Phys.*, 2007, **126**, 114302.
- [120] Q. Peng, Y. Niu, Q. Shi, X. Gao and Z. Shuai, *J. Chem. Theory Comput.*, 2013, **9**, 1132–1143.
- [121] Q. Peng, Y. Yi, Z. Shuai and J. Shao, *J. Am. Chem. Soc.*, 2007, **129**, 9333–9339.
- [122] Y. Niu, W. Li, Q. Peng, H. Geng, Y. Yi, L. Wang, G. Nan, D. Wang and Z. Shuai, *Mol. Phys.*, 2018, **116**, 1078–1090.
- [123] Z. Shuai, D. Wang, Q. Peng and H. Geng, *Acc. Chem. Res.*, 2014, **47**, 3301–3309.
- [124] Z. Shuai and Q. Peng, *Phys. Rep.*, 2014, **537**, 123–156.
- [125] Q. Wu, T. Zhang, Q. Peng, D. Wang and Z. Shuai, *Phys. Chem. Chem. Phys.*, 2014, **16**, 5545–52.
- [126] T. Zhang, H. Ma, Y. Niu, W. Li, D. Wang, Q. Peng, Z. Shuai and W. Z. Liang, *J. Phys. Chem. C*, 2015, **119**, 5040–5047.
- [127] X. Zheng, Q. Peng, L. Zhu, Y. Xie, X. Huang and Z. Shuai, *Nanoscale*, 2016, **8**, 15173–15180.
- [128] T. Zhang, Q. Peng, C. Quan, H. Nie, Y. Niu, Y. Xie, Z. Zhao, B. Z. Tang and Z. Shuai, *Chem. Sci.*, 2016, **7**, 5573–5580.
- [129] Y. C. Duan, Y. Wu, J. L. Jin, D. M. Gu, Y. Geng, M. Zhang and Z. M. Su, *ChemPhysChem*, 2017, **18**, 755–762.
- [130] J. Fan, Y. Zhang, Y. Zhou, L. Lin and C. K. Wang, *J. Phys. Chem. C*, 2018, **122**, 2358–2366.
- [131] J. R. Reimers, *J. Chem. Phys.*, 2001, **115**, 9103–9109.
- [132] J.-L. Brédas, D. Beljonne, V. Coropceanu and J. Cornil, *Chem. Rev.*, 2004, **104**, 4971–5004.

- [133] V. Stehr, R. F. Fink, B. Engels, J. Pflaum and C. Deibel, *J. Chem. Theory Comput.*, 2014, **10**, 1242–1255.
- [134] A. Prlj, N. Došlić and C. Corminboeuf, *Phys. Chem. Chem. Phys.*, 2016, **18**, 11606–11609.
- [135] Y. Cai, L. Du, K. Samedov, X. Gu, F. Qi, H. H. Sung, B. O. Patrick, Z. Yan, X. Jiang, H. Zhang, J. W. Lam, I. D. Williams, D. Lee Phillips, A. Qin and B. Z. Tang, *Chem. Sci.*, 2018, **9**, 4662–4670.
- [136] Y. J. Gao, X. P. Chang, X. Y. Liu, Q. S. Li, G. Cui and W. Thiel, *J. Phys. Chem. A*, 2017, **121**, 2572–2579.
- [137] S. Sasaki, S. Suzuki, W. M. C. Sameera, K. Igawa, K. Morokuma and G. I. Konishi, *J. Am. Chem. Soc.*, 2016, **138**, 8194–8206.
- [138] C. Yuan, S. Saito, C. Camacho, S. Irle, I. Hisaki and S. Yamaguchi, *J. Am. Chem. Soc.*, 2013, **135**, 8842–8845.
- [139] A. Weller, *Naturwissenschaften*, 1955, **42**, 175–176.
- [140] C. Azarias, Ā. Budzák, A. D. Laurent, G. Ulrich and D. Jacquemin, *Chem. Sci.*, 2016, **7**, 3763–3774.
- [141] D. A. Yushchenko, V. V. Shvadchak, A. S. Klymchenko, G. Duportail, V. G. Pivovarenko and Y. Mély, *J. Phys. Chem. A*, 2007, **111**, 10435–10438.
- [142] C.-C. Hsieh, C.-M. Jiang and P.-T. Chou, *Acc. Chem. Res.*, 2010, **43**, 1364–1374.
- [143] J. E. Kwon and S. Y. Park, *Adv. Mater.*, 2011, **23**, 3615–3642.
- [144] J. Zhao, S. Ji, Y. Chen, H. Guo and P. Yang, *Phys. Chem. Chem. Phys.*, 2012, **14**, 8803.
- [145] A. P. Demchenko, K.-C. Tang and P.-T. Chou, *Chem. Soc. Rev.*, 2013, **42**, 1379–1408.
- [146] C.-L. Chen, Y.-T. Chen, A. P. Demchenko and P.-T. Chou, *Nat. Rev. Chem.*, 2018, **2**, 131–143.
- [147] H. Lin, X. Chang, D. Yan, W. H. Fang and G. Cui, *Chem. Sci.*, 2017, **8**, 2086–2090.
- [148] B. Li, G. Tang, L. Zhou, D. Wu, J. Lan, L. Zhou, Z. Lu and J. You, *Adv. Funct. Mater.*, 2017, **27**, 1605245.
- [149] W. Al-Soufi, K. H. Grellmann and B. Nickel, *Chem. Phys. Lett.*, 1990, **174**, 609–616.
- [150] J. Cheng, D. Liu, W. Li, L. Bao and K. Han, *J. Phys. Chem. C*, 2015, **119**, 4242–4251.
- [151] M. Kasha, *J. Chem. Soc., Faraday Trans.*, 1986, **82**, 2379–2392.
- [152] A. D. Laurent, Y. Houari, P. H. P. R. Carvalho, B. A. D. Neto and D. Jacquemin, *RSC Adv.*,

- 2014, **4**, 14189–14192.
- [153] S. Park, J. E. Kwon, S.-Y. Park, O.-H. Kwon, J. K. Kim, S.-J. Yoon, J. W. Chung, D. R. Whang, S. K. Park, D. K. Lee, D.-J. Jang, J. Gierschner and S. Y. Park, *Adv. Opt. Mater.*, 2017, **5**, 1700353.
- [154] D.-E. Wu, Q.-C. Yao and M. Xia, *Phys. Chem. Chem. Phys.*, 2015, **17**, 3287–3294.
- [155] A. L. Sobolewski, W. Domcke and C. Hättig, *J. Phys. Chem. A*, 2006, **110**, 6301–6306.
- [156] A. L. Sobolewski and W. Domcke, *Phys. Chem. Chem. Phys.*, 2006, **8**, 3410–3417.
- [157] M. Barbatti, A. J. A. Aquino, H. Lischka, C. Schrieffer, S. Lochbrunner and E. Riedle, *Phys. Chem. Chem. Phys.*, 2009, **11**, 1406–1415.
- [158] S. Park, E. K. Ji, H. K. Se, J. Seo, K. Chung, S. Y. Park, D. J. Jang, B. M. Medina, J. Gierschner and Y. P. Soo, *J. Am. Chem. Soc.*, 2009, **131**, 14043–14049.
- [159] S. Lochbrunner, T. Schultz, M. Schmitt, J. P. Shaffer, M. Z. Zgierski and A. Stolow, *J. Chem. Phys.*, 2001, **114**, 2519.
- [160] Y. Shigemitsu, T. Mutai, H. Houjou and K. Araki, *J. Phys. Chem. A*, 2012, **116**, 12041–12048.
- [161] L. Spörkel, G. Cui, A. Koslowski and W. Thiel, *J. Phys. Chem. A*, 2014, **118**, 152–157.
- [162] F. Plasser, R. Crespo-Otero, M. Pederzoli, J. Pittner, H. Lischka and M. Barbatti, *J. Chem. Theory Comput.*, 2014, **10**, 1395–1405.
- [163] L. a. Baker, M. D. Horbury, S. E. Greenough, P. M. Coulter, T. N. V. Karsili, G. M. Roberts, A. J. Orr-Ewing, M. N. R. Ashfold and V. G. Stavros, *J. Phys. Chem. Lett.*, 2015, **6**, 1363–1368.
- [164] R. Wang, D. Liu, K. Xu and J. Li, *J. Photochem. Photobiol., A.*, 2009, **205**, 61–69.
- [165] L. Tang, M. Tian, H. Chen, X. Yan, K. Zhong and Y. Bian, *Dyes Pigm.*, 2018, **158**, 482–489.
- [166] V. Kachwal, I. S. Vamsi Krishna, L. Fageria, J. Chaudhary, R. Kinkar Roy, R. Chowdhury and I. R. Laskar, *Analyst*, 2018, **143**, 3741–3748.
- [167] Y. Liu, J. Nie, J. Niu, W. Wang and W. Lin, *J. Mater. Chem. B.*, 2018, **6**, 1973–1983.
- [168] S. Park, J. Seo, S. H. Kim and S. Y. Park, *Adv. Funct. Mater.*, 2008, **18**, 726–731.
- [169] S. H. Kim, S. Park, J. E. Kwon and S. Y. Park, *Adv. Funct. Mater.*, 2011, **21**, 644–651.
- [170] M. Mamada, K. Inada, T. Komino, W. J. Potscavage, H. Nakanotani and C. Adachi, *ACS*

- Cent. Sci.*, 2017, **3**, 769–777.
- [171] K.-C. Tang, M.-J. Chang, T.-Y. Lin, H.-A. Pan, T.-C. Fang, K.-Y. Chen, W.-Y. Hung, Y.-H. Hsu and P.-T. Chou, *J. Am. Chem. Soc.*, 2011, **133**, 17738–17745.
- [172] D. Yao, S. Zhao, J. Guo, Z. Zhang, H. Zhang, Y. Liu and Y. Wang, *J. Mater. Chem.*, 2011, **21**, 3568–3570.
- [173] Z. Zhang, Y.-A. Chen, W.-Y. Hung, W.-F. Tang, Y.-H. Hsu, C.-L. Chen, F.-Y. Meng and P.-T. Chou, *Chem. Mater.*, 2016, **28**, 8815–8824.
- [174] I. E. Serdiuk, *J. Phys. Chem. C*, 2017, **121**, 5277–5286.
- [175] H.-H. Fang, J. Yang, J. Feng, T. Yamao, S. Hotta and H.-B. Sun, *Laser Photonics Rev.*, 2014, **8**, 687–715.
- [176] J. Gierschner, S. Varghese and S. Y. Park, *Adv. Opt. Mater.*, 2016, **4**, 348–364.
- [177] A. U. Khan and M. Kasha, *Proc. Natl. Acad. Sci. U.S.A.*, 1983, **80**, 1767–1770.
- [178] P. Chou, D. McMorro, T. J. Aartsma and M. Kasha, *J. Phys. Chem.*, 1984, **88**, 4596–4599.
- [179] K. I. Sakai, S. Tsuchiya, T. Kikuchi and T. Akutagawa, *J. Mater. Chem. C*, 2016, **4**, 2011–2016.
- [180] L. Chen, S. Y. Yin, M. Pan, K. Wu, H. P. Wang, Y. N. Fan and C. Y. Su, *J. Mater. Chem. C*, 2016, **4**, 6962–6966.
- [181] S. Park, J. E. Kwon and S. Y. Park, *Phys. Chem. Chem. Phys.*, 2012, **14**, 8878–8884.
- [182] X. Cheng, K. Wang, S. Huang, H. Zhang, H. Zhang and Y. Wang, *Angew. Chem., Int. Ed.*, 2015, **54**, 8369–8373.
- [183] X. Cheng, Y. Zhang, S. Han, F. Li, H. Zhang and Y. Wang, *Chem. Eur. J.*, 2016, **22**, 4899–4903.
- [184] B. Tang, H. Liu, F. Li, Y. Wang and H. Zhang, *Chem. Commun.*, 2016, **52**, 6577–6580.
- [185] P. Singh, A. Anand and V. Kumar, *Eur. J. Med. Chem.*, 2014, **85**, 758–777.
- [186] P.-t. Chou, M. L. Martinez and W. C. Cooper, *J. Am. Chem. Soc.*, 1992, **114**, 4943–4944.
- [187] F. R. Stermitz, A. Adamovics and J. Geigert, *Tetrahedron*, 1975, **31**, 1595.
- [188] R. Matsushima and H. Kageyama, *J. Chem. Soc., Perkin Trans. 1*, 1985, 743.
- [189] K. Tokumura and R. Matsushima, *Chem. Phys. Lett.*, 1998, **295**, 516–524.
- [190] T. Arai and Y. Norikane, *Chem. Lett.*, 1997, **26**, 339–340.

- [191] Y. Norikane, H. Itoh and T. Arai, *J. Phys. Chem. A*, 2002, **106**, 2766–2776.
- [192] Y. Norikane, N. Nakayama, N. Tamaoki, T. Arai and U. Nagashima, *J. Phys. Chem. A*, 2003, **107**, 8659–8664.
- [193] K. Kaneda and T. Arai, *Org. Biomol. Chem*, 2003, **1**, 2041–2043.
- [194] K. Kaneda and T. Arai, *Photochem. Photobiol. Sci.*, 2003, **2**, 402.
- [195] K. Kaneda, S. Sato, H. O. Hamaguchi and T. Arai, *Bull. Chem. Soc. Jpn.*, 2004, **77**, 1529–1535.
- [196] T. Teshima, M. Takeishi and T. Arai, *New J. Chem.*, 2009, **33**, 1393.
- [197] Y. Shinozaki, M. Yamaji and T. Arai, *J. Photochem. Photobiol., A*, 2018, **350**, 17–22.
- [198] R. Li, L. Yan, Z. Wang and Z. Qi, *J. Mol. Struct.*, 2017, **1136**, 1–6.
- [199] Z. Song, R. T. K. Kwok, E. Zhao, Z. He, Y. Hong, J. W. Y. Lam, B. Liu and B. Z. Tang, *ACS Appl. Mater. Interfaces*, 2014, **6**, 17245–54.
- [200] X. Jin, L. Dong, X. Di, H. Huang, J. Liu, X. Sun, X. Zhang and H. Zhu, *RSC Adv.*, 2015, **5**, 87306–87310.
- [201] J. Li, Y. Wu, Z. Xu, Q. Liao, H. Zhang, Y. Zhang, L. Xiao, J. Yao and H. Fu, *J. Mater. Chem. C*, 2017, **5**, 12235–12240.
- [202] N. I. Zahid, M. S. Mahmood, B. Subramanian, S. Mohd Said and O. K. Abou-Zied, *J. Phys. Chem. Lett.*, 2017, 5603–5608.
- [203] H. Song, Z. Kuang, X. Wang, Y. Guo, Q. Guo, H. Zhang and A. Xia, *J. Phys. Chem. C*, 2018, **122**, 15108–15117.
- [204] I. E. Serdiuk, M. Wera and A. D. Roshal, *J. Phys. Chem. A*, 2018, **122**, 2030–2038.
- [205] D. R. Hartree, *Math. Proc. Cambridge Philos. Soc.*, 1928, **24**, 426–437.
- [206] J. C. Slater, *Phys. Rev.*, 1929, **34**, 1293–1322.
- [207] C. C. J. Roothaan, *Rev. Mod. Phys.*, 1951, **23**, 69–89.
- [208] G. G. Hall, *Proc. R. Soc. Lond. A Math. Phys. Sci.*, 1951, **205**, 541–552.
- [209] C. Møller and M. S. Plesset, *Phys. Rev.*, 1934, **46**, 618–622.
- [210] J. Čížek, *J. Chem. Phys.*, 1966, **45**, 4256–4266.
- [211] J. Paldus, J. Íek and I. Shavitt, *Phys. Rev. A*, 1972, **5**, 50–67.
- [212] B. O. Roos, P. R. Taylor and P. E. M. Siegbahn, *Chem. Phys.*, 1980, **48**, 1680.

- [213] H. Lischka, D. Nachtigallová, A. J. A. Aquino, P. G. Szalay, F. Plasser, F. B. C. Machado and M. Barbatti, *Chem. Rev.*, 2018, **118**, 7293–7361.
- [214] C. J. Stein and M. Reiher, *J. Chem. Theory Comput.*, 2016, **12**, 1760–1771.
- [215] J. J. Bao, S. S. Dong, L. Gagliardi and D. G. Truhlar, *J. Chem. Theory Comput.*, 2018, **14**, 2017–2025.
- [216] E. Ramos-Cordoba, P. Salvador and E. Matito, *Phys. Chem. Chem. Phys.*, 2016, **18**, 24015–24023.
- [217] C. J. Stein, V. Von Burg and M. Reiher, *J. Chem. Theory Comput.*, 2016, **12**, 3764–3773.
- [218] K. Andersson, P. Å. Malmqvist and B. O. Roos, *J. Chem. Phys.*, 1992, **96**, 1218–1226.
- [219] J. Finley, P.-Å. Malmqvist, B. O. Roos and L. Serrano-Andrés, *Chem. Phys. Lett.*, 1998, **288**, 299–306.
- [220] P. Hohenberg and W. Kohn, *Phys. Rev.*, 1964, **136**, B864–B871.
- [221] W. Kohn and L. J. Sham, *Phys. Rev.*, 1965, **140**, A1133–A1138.
- [222] C. Ullrich, *Time-Dependent Density-Functional Theory: Concepts and Applications*, Oxford University Press, New York, 2012.
- [223] J. P. Perdew, K. Burke and M. Ernzerhof, *Phys. Rev. Lett.*, 1996, **77**, 3865–3868.
- [224] W. Koch and M. C. Holthausen, *A Chemist's Guide to Density Functional Theory*, Wiley-VCH Verlag GmbH, New York, 2001.
- [225] D. Young, *Computational Chemistry: A Practical Guide for Applying Techniques to Real World Problems*, Wiley-Interscience, New York, 2001.
- [226] E. Runge and E. K. Gross, *Phys. Rev. Lett.*, 1984, **52**, 997–1000.
- [227] R. V. Leeuwen, *Phys. Rev. Lett.*, 1999, 3863–3866.
- [228] C. A. Ullrich and Z. h. Yang, *Braz. J. Phys.*, 2014, **44**, 154–188.
- [229] M. E. Casida, *Recent Advances in Computational Chemistry*, World Scientific, Singapore, 1995, pp. 155–192.
- [230] T. Stein, L. Kronik and R. Baer, *J. Am. Chem. Soc.*, 2009, **131**, 2818–2820.
- [231] N. Kuritz, T. Stein, R. Baer and L. Kronik, *J. Chem. Theory Comput.*, 2011, **7**, 2408–2415.
- [232] L. Kronik, T. Stein, S. Refaely-Abramson and R. Baer, *J. Chem. Theory Comput.*, 2012, **8**, 1515–1531.

- [233] J.-D. Chai and M. Head-Gordon, *Phys. Chem. Chem. Phys.*, 2008, **10**, 6615.
- [234] O. Christiansen, H. Koch and P. Jorgensen, *Chem. Phys. Lett.*, 1995, **243**, 409–418.
- [235] C. Hättig, *Adv. Quantum Chem.*, 2005, **50**, 37–60.
- [236] K. Sneskov and O. Christiansen, *WIREs Comput. Mol. Sci.*, 2012, **2**, 566–584.
- [237] A. D. Laurent, A. Blondel and D. Jacquemin, *Theo. Chem. Acc.*, 2015, **134**, 1–11.
- [238] A. B. Trofimov and J. Schirmer, *J. Phys. B: At., Mol. Opt. Phys.*, 1995, **28**, 2299.
- [239] A. Trofimov and J. Schirmer, *Chem. Phys.*, 1997, **214**, 153–170.
- [240] D. Jacquemin, I. Duchemin and X. Blase, *J. Chem. Theory Comput.*, 2015, **11**, 5340–5359.
- [241] A. Dreuw and M. Wormit, *Wiley Interdiscip. Rev. Comput. Mol. Sci.*, 2015, **5**, 82–95.
- [242] N. Koga and K. Morokuma, *Chem. Phys. Lett.*, 1985, **119**, 371–374.
- [243] M. R. Manaa and D. R. Yarkony, *J. Chem. Phys.*, 1993, **99**, 5251–5256.
- [244] M. J. Bearpark, M. A. Robb and H. Bernhard Schlegel, *Chem. Phys. Lett.*, 1994, **223**, 269–274.
- [245] M. Dallos, H. Lischka, R. Shepard, D. R. Yarkony and P. G. Szalay, *J. Chem. Phys.*, 2004, **120**, 7330–7339.
- [246] D. R. Yarkony, *J. Phys. Chem. A*, 2004, **108**, 3200–3205.
- [247] B. G. Levine, C. Ko, J. Quenneville and T. J. Martínez, *Mol. Phys.*, 2006, **104**, 1039–1051.
- [248] S. Gozem, F. Melaccio, A. Valentini, M. Filatov, M. Huix-Rotllant, N. Ferré, L. M. Frutos, C. Angeli, A. I. Krylov, A. a. Granovsky, R. Lindh and M. Olivucci, *J. Chem. Theory Comput.*, 2014, **10**, 3074–3084.
- [249] D. Tuna, D. Lefrancois, L. Wolanski, S. Gozem, I. Schapiro, T. Andruniow, A. Dreuw and M. Olivucci, *J. Chem. Theory Comput.*, 2015, **11**, 5758–5781.
- [250] D. Lefrancois, D. Tuna, T. J. Martínez and A. Dreuw, *J. Chem. Theory Comput.*, 2017, **13**, 4436–4441.
- [251] R. Crespo-Otero, A. Mardykov, E. Sanchez-Garcia, W. Sander and M. Barbatti, *Phys. Chem. Chem. Phys.*, 2014, **16**, 18877–18887.
- [252] M. Barbatti and R. Crespo-Otero, *Density-Functional Methods for Excited States*, Springer International Publishing: Cham, 2016, vol. 368, pp. 415–444.
- [253] M. Dommett and R. Crespo-Otero, *Phys. Chem. Chem. Phys.*, 2017, **19**, 2409–2416.

- [254] F. Haase and R. Ahlrichs, *J. Comput. Chem.*, 1993, **14**, 907–912.
- [255] A. Schäfer, H. Horn and R. Ahlrichs, *J. Chem. Phys.*, 1992, **97**, 2571–2577.
- [256] F. Weigend and R. Ahlrichs, *Phys. Chem. Chem. Phys.*, 2005, **7**, 3297.
- [257] C. Hättig and F. Weigend, *J. Chem. Phys.*, 2000, **113**, 5154–5161.
- [258] C. Hättig and A. Köhn, *J. Chem. Phys.*, 2002, **117**, 6939–6951.
- [259] A. Köhn and C. Hättig, *J. Chem. Phys.*, 2003, **119**, 5021–5036.
- [260] *TURBOMOLE V7.0 2015, a development of University of Karlsruhe and Forschungszentrum Karlsruhe GmbH, 1989-2007, TURBOMOLE GmbH, since 2007; available from <http://www.turbomole.com>.*
- [261] H. Werner, P. J. Knowles, G. Knizia, F. R. Manby and M. Schütz, *Wiley Interdiscip. Rev. Comput. Mol. Sci.*, 2012, **2**, 242–253.
- [262] M. Barbatti, M. Ruckebauer, F. Plasser, J. Pittner, G. Granucci, M. Persico and H. Lischka, *Wiley Interdiscip. Rev. Comput. Mol. Sci.*, 2014, **4**, 26–33.
- [263] M. Barbatti, G. Granucci, M. Persico, M. Ruckebauer, M. Vazdar, M. Eckert-Maksić and H. Lischka, *J. Photochem. Photobiol., A.*, 2007, **190**, 228–240.
- [264] M. J. Paterson, M. A. Robb, L. Blancafort and A. D. DeBellis, *J. Phys. Chem. A*, 2005, **109**, 7527–7537.
- [265] Maxima, *Maxima, a Computer Algebra System. Version 5.34.1*, 2014, <http://maxima.sourceforge.net/>.
- [266] E. Jones, T. Oliphant, P. Peterson and others, *SciPy: Open source scientific tools for Python*, <http://www.scipy.org/>.
- [267] M. Dommert, M. Rivera and R. Crespo-Otero, *J. Phys. Chem. Lett.*, 2017, 6148–6153.
- [268] P. Giannozzi, S. Baroni, N. Bonini, M. Calandra, R. Car, C. Cavazzoni, D. Ceresoli, G. L. Chiarotti, M. Cococcioni, I. Dabo, A. Dal Corso, S. de Gironcoli, S. Fabris, G. Fratesi, R. Gebauer, U. Gerstmann, C. Gougoussis, A. Kokalj, M. Lazzeri, L. Martin-Samos, N. Marzari, F. Mauri, R. Mazzarello, S. Paolini, A. Pasquarello, L. Paulatto, C. Sbraccia, S. Scandolo, G. Sclauzero, A. P. Seitsonen, A. Smogunov, P. Umari and R. M. Wentzcovitch, *J. Phys. Condens. Matter*, 2009, **21**, 395502.
- [269] K. Sen, R. Crespo-Otero, O. Weingart, W. Thiel and M. Barbatti, *J. Chem. Theory Comput.*, 2013, **9**, 533–542.

- [270] M. J. Frisch, G. W. Trucks, H. B. Schlegel, G. E. Scuseria, M. A. Robb, J. R. Cheeseman, G. Scalmani, V. Barone, B. Mennucci, G. A. Petersson, H. Nakatsuji, M. Caricato, X. Li, H. P. Hratchian, A. F. Izmaylov, J. Bloino, G. Zheng, J. L. Sonnenberg, M. Hada, M. Ehara, K. Toyota, R. Fukuda, J. Hasegawa, M. Ishida, T. Nakajima, Y. Honda, O. Kitao, H. Nakai, T. Vreven, J. A. Montgomery, J. E. Peralta, F. Ogliaro, M. Bearpark, J. J. Heyd, E. Brothers, K. N. Kudin, V. N. Staroverov, R. Kobayashi, J. Normand, K. Raghavachari, A. Rendell, J. C. Burant, S. S. Iyengar, J. Tomasi, M. Cossi, N. Rega, J. M. Millam, M. Klene, J. E. Knox, J. B. Cross, V. Bakken, C. Adamo, J. Jaramillo, R. Gomperts, R. E. Stratmann, O. Yazyev, A. J. Austin, R. Cammi, C. Pomelli, J. W. Ochterski, R. L. Martin, K. Morokuma, V. G. Zakrzewski, G. A. Voth, P. Salvador, J. J. Dannenberg, S. Dapprich, A. D. Daniels, Farkas, J. B. Foresman, J. V. Ortiz, J. Cioslowski and D. J. Fox, *Gaussian 09, Revision D.01*, 2009.
- [271] F. Aquilante, J. Autschbach, R. K. Carlson, L. F. Chibotaru, M. G. Delcey, L. De Vico, I. Fdez Galván, N. Ferré, L. M. Frutos, L. Gagliardi, M. Garavelli, A. Giussani, C. E. Hoyer, G. Li Manni, H. Lischka, D. Ma, P. Å. Malmqvist, T. Müller, A. Nenov, M. Olivucci, T. B. Pedersen, D. Peng, F. Plasser, B. Pritchard, M. Reiher, I. Rivalta, I. Schapiro, J. Segarra-Martí, M. Stenrup, D. G. Truhlar, L. Ungur, A. Valentini, S. Vancoillie, V. Veryazov, V. P. Vysotskiy, O. Weingart, F. Zapata and R. Lindh, *J. Comput. Chem.*, 2016, **37**, 506–541.
- [272] J. A. Rackers, Z. Wang, C. Lu, M. L. Laury, L. Lagardère, M. J. Schnieders, J. P. Piquemal, P. Ren and J. W. Ponder, *J. Chem. Theory Comput.*, 2018, **14**, 5273–5289.
- [273] M. Dommert, *exciton_coupling: a python package to calculate the exciton coupling in molecular dimers*, 2018, https://github.com/mdommett/exciton_coupling.
- [274] A. J. A. Aquino, H. Lischka and C. Hättig, *J. Phys. Chem. A*, 2005, **109**, 3201–3208.
- [275] T. N. V. Karsili, B. Marchetti and M. N. R. Ashfold, *Dalton Trans.*, 2016, **45**, 18921–18930.
- [276] J. E. Campbell, J. Yang and G. M. Day, *J. Mater. Chem. C*, 2017, **5**, 7574–7584.
- [277] T. Yanai, D. P. Tew and N. C. Handy, *Chem. Phys. Lett.*, 2004, **393**, 51–57.
- [278] R. P. Fornari, J. Aragón and A. Troisi, *J. Phys. Chem. C*, 2016, **120**, 7987–7996.
- [279] C. Brückner and B. Engels, *J. Comput. Chem.*, 2016, **37**, 1335–1344.
- [280] A. Kimura, T. Kakitani and T. Yamato, *J. Phys. Chem. B*, 2000, **104**, 9276–9287.

Appendices

Appendix A

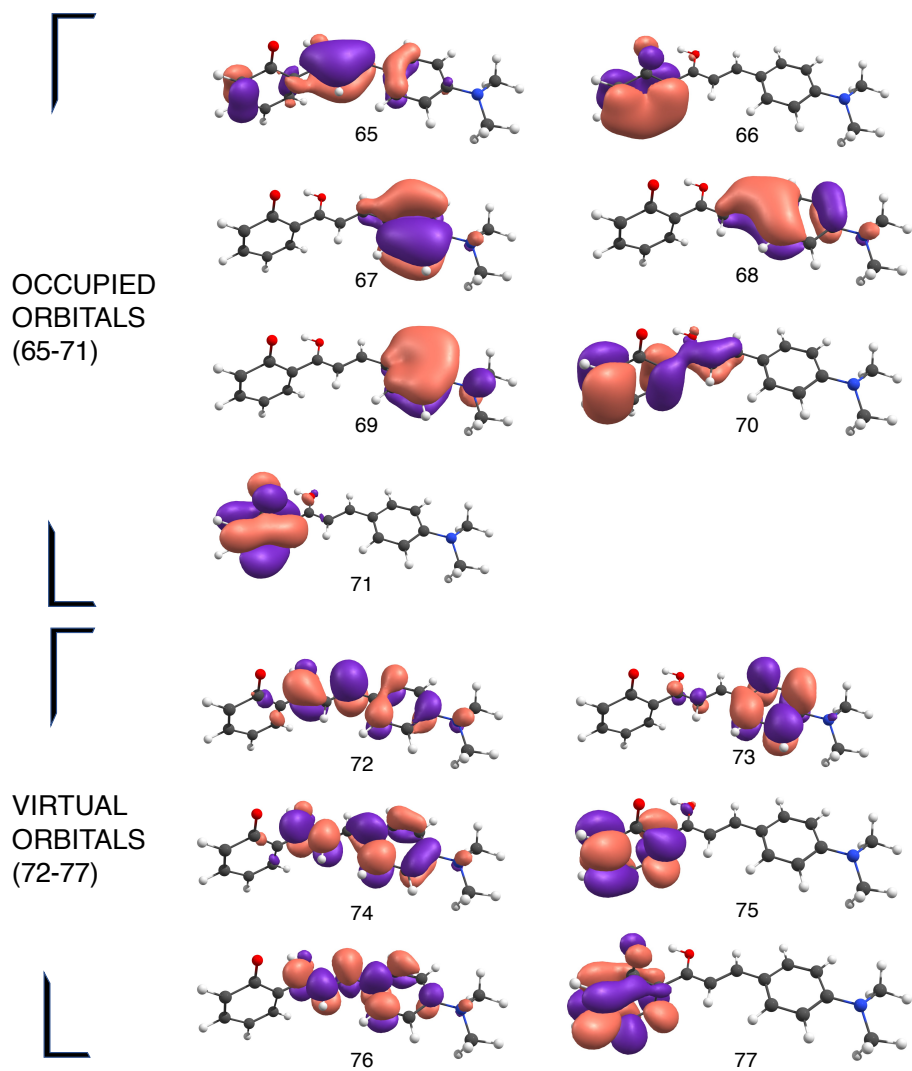


Figure A1: CASSCF space used in Chapter 5.

Appendix B

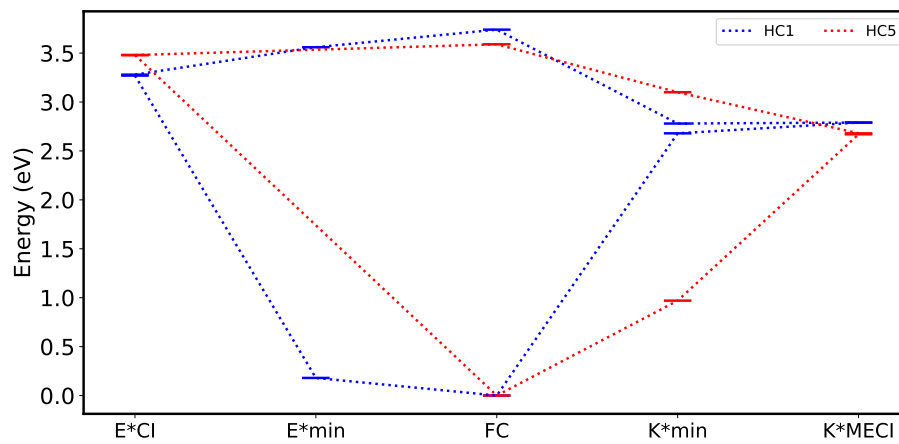


Figure A2: The critical points on the PES of **HC1** & **HC5** obtained at (TD-) ω BX-D/6-31G(d) in vacuum.

Appendix C

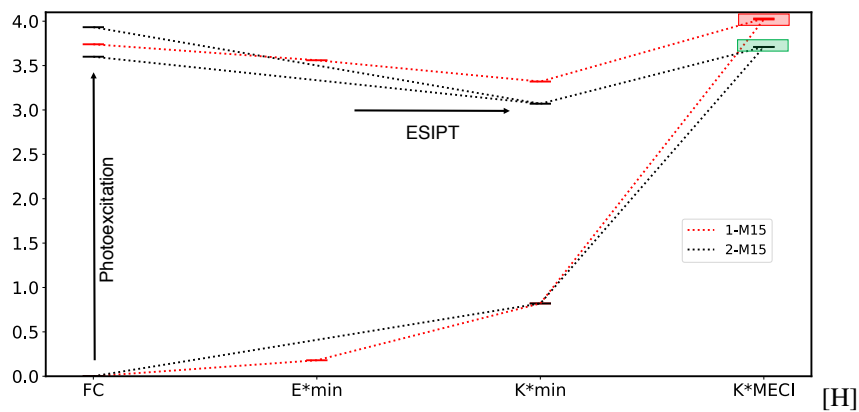


Figure A3: Energy of the S₀ and S₁ states at the Franck-Condon (FC) point, E* and K* minima, and the MECI of **1** and **5** with the **M15** model with ONIOM(ω B7X-D/6-31G(d)):AMBER level of theory. The accessibility is colour coded.

Appendix D

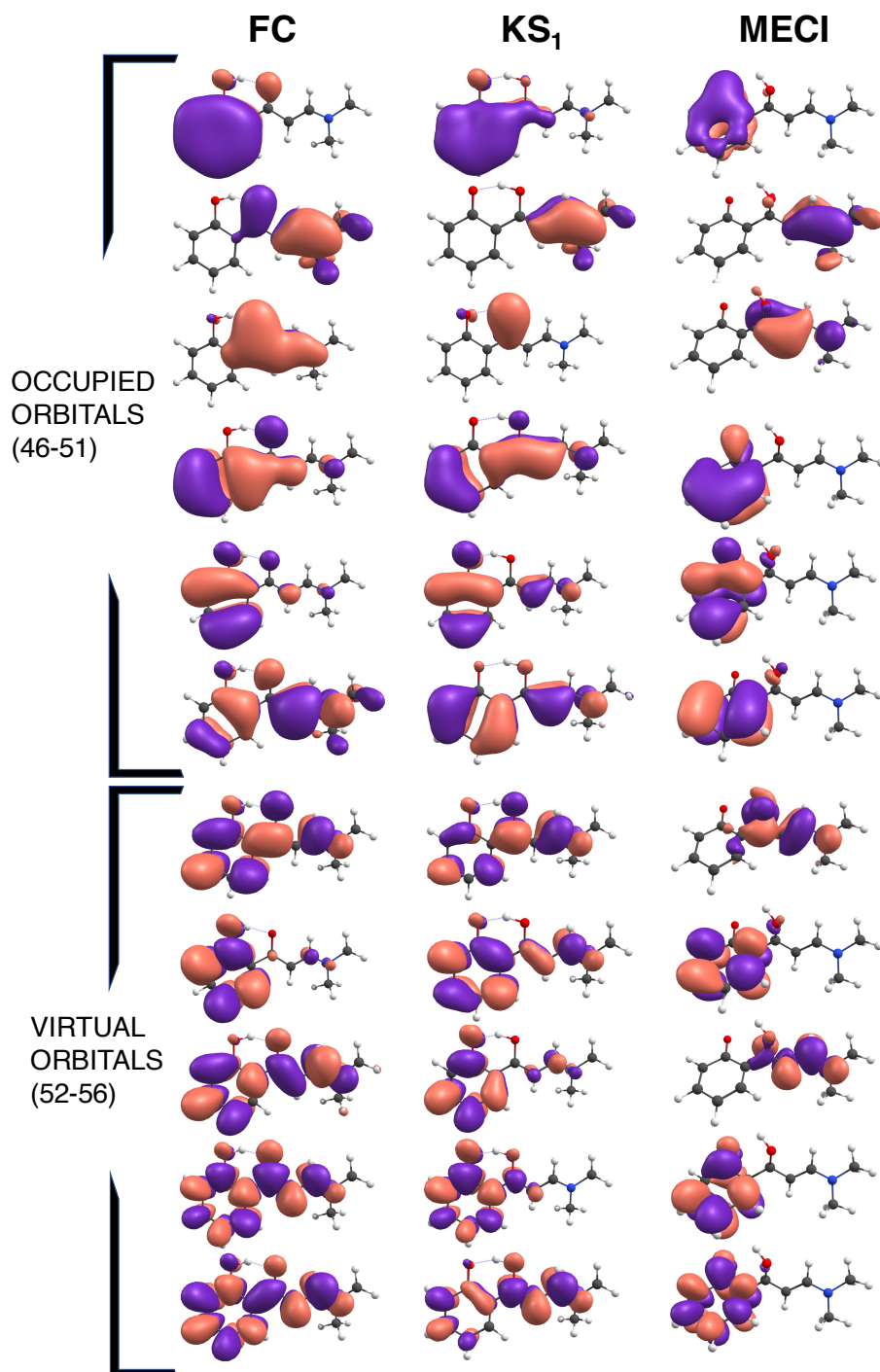


Figure A4: HP orbitals in the active space for the CASSCF and CASPT2 calculations, where the active space consists of 12 electrons in 11 orbitals. Orbitals shown for each of the Franck-Condon (FC), keto S₁ (KS₁) and minimum energy conical intersection (MECI) calculations.